Readout

HORIBA Technical Reports

May 2024　No. **58**

特集　次世代半導体デバイスの開発に貢献する分析・計測技術
　　　2023 堀場雅夫賞

HORIBA

https://www.horiba.com/jp/publications/readout/

Readout

HORIBA Technical Reports

May 2024　No.58
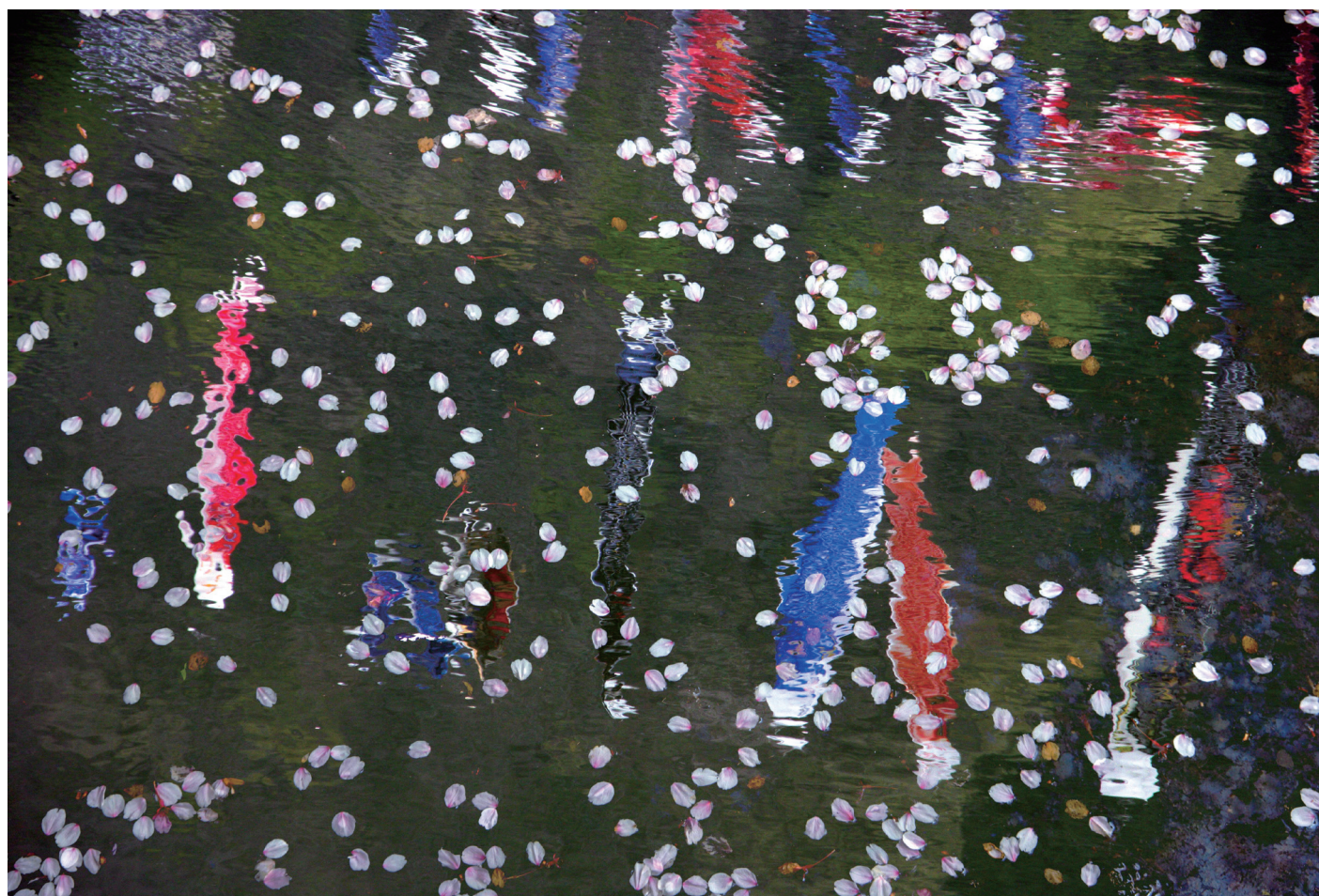
近年，半導体技術はデジタル化社会の進展と共に急速に進化を遂げています。次世代の3Dパッケージング技術や2次元材料の活用が注目され，これらは情報処理の高速化と大容量化を実現するための鍵となっています。本号では，対象分野を「次世代半導体デバイスの開発に貢献する分析・計測技術」とした堀場雅夫賞の内容とHORIBAが展開する半導体材料・プロセス解析技術とその取り組みについて紹介します。

■表紙写真
撮影: 写真家　松井秀雄氏
　　　（二科会写真部　会員）
良く晴れた春の日に，桜で有名な山あいの公園を訪ねました。上空に飾られた鯉のぼりが風に吹かれて元気良く泳ぎ，川面には桜の花びらが春の風情を添えてくれていました。

■誌名について
誌名 Readout（リードアウト）には，「当社が創造・育成した製品・技術を広く世にお知らせし，多くの皆様に読み取っていただきたい」という願いが込められています。

特集 次世代半導体デバイスの開発に貢献する分析・計測技術 2023 堀場雅夫賞

The continuing evolution of Semiconductor technologies has enabled the development of the digital society. Keys to further developments in faster information processing and increased calculation capacity include next generation 3D packaging technologies and the integration of 2D materials in integrated circuits. In this issue of the Readout, we will introduce you to the topics of the 2023 Masao Horiba Awards whose theme was "Analysis and measurement technologies that contribute to the development of the next generation of semiconductor devices" and to HORIBA's technologies and activities around semiconductor materials and process analysis.

On a beautiful sunny spring day, I visited a park in the mountains famous for its cherry blossoms. I could feel spring as Koinobori in the sky were swimming energetically in the wind and cherry blossom petals were floating on the river surface.
-Photographer MATSUI Hideo- (Member of Nikakai Association of Photographers)

Name of this Journal

This Journal is named "Readout" in the hope that "the products and technology we have created and developed will be read out and so become widely known".

Analysis and Measurement Technologies that Contribute to the Development of Next Generation Semiconductor Devices 2023 Masao Horiba Awards

Analytical Instruments in Semiconductor Development
半導体開発における分析機器

Dale A. POOLE Jr

Corporate Officer
HORIBA, Ltd.
Senior Corporate Officer,
HORIBA STEC, Co., Ltd.
Executive Vice President, HORIBA Instruments Incorporated

In 1959 Jack Kilby of Texas Instruments and Robert Noyce of Fairchild developed and patented the basic concept and manufacturing technology of the integrated circuit. Soon after this, in the early 60's, computers were being constructed with what we would consider this very basic technology. The remarkable part of this semiconductor-based device was the scalability of silicon with a simple planar structure. Currently with billions of transistors on a single die, a basic smartphone processor has far more power than a Cray Supercomputer of the late 70's. This revolution in materials and design has fundamentally changed the world and ushered in the age of information. One could compare how early electrification opened a new world of possibilities in a similar way to what is happening today. With the common use of the internet, smartphones and cloud computing, we are quickly entering the age of ubiquitous computing and our lives and world are defined by it. This now has enabled the 4th industrial revolution and with the advent of artificial intelligence (AI), it is easy to see how the world as we know it is completely dependent and defined by the computational capability of integrated circuits (IC's).

The Semiconductor market has become a key strategic business for HORIBA. HORIBA is the leading company for the components of Fluid delivery to the Dry process chamber and Chemical Concentration monitoring in Wet processes with some products in metrology for reticle inspection. The Scientific segment has concentrated on high-end analytical benchtop equipment, thin film ellipsometry, and the original equipment manufacturer (OEM) end-point market with good results. One important aspect of the Semiconductor market is that it is constantly evolving. The planar structure is no longer the basis of the most sophisticated IC's such as 3D NAND flash memory and FinFet three dimensional (3D) transistors used in CMOS logic. These

Foreword

devices require new materials and manufacturing techniques that are reshaping the demands of the Semiconductor industry.

New technologies are needed as node shrink[*1] comes to an end point with existing planar structures, in other words, one is no longer able to manufacture a semiconductor chip with reliable performance utilizing the techniques of the past. Moore's law stated that the number of transistors on an IC will double every two years, and this was possible for many years but completely new approaches such as the FinFet 3D transistor and advanced packaging are required to keep Moore's law relevant. One of the key parameters for any semiconductor design is the bandgap which basically defines the parameters which causes a device transistor to turn on or off and as well as the transistor gate leakage. As transistors get smaller and smaller, using materials that provide the correct electron mobility and insulating properties for the gate no longer work correctly in a planar architecture. The gate area becomes so small that the transistor will not function. One way to continue to shrink the gate 2D area is to build a 3D structure that provides a larger volume for the gate. This approach is beginning to reach its limit and a new structure called Gate All Around (GAA) will be required which brings with it many new processes and materials. Eventually a GAA transistor will reach its limits and new materials called 2D materials[*2] will allow transistors to be stacked on top of each other allowing for a big improvement in transistor density. While GAA is being implemented in Semiconductor Fab's now, 2D transistors[*3] are at least 5 to 10 years away from mass production. This means that Moore's law is still relevant and has a device roadmap even though the transistor count scaling per year has slowed down from the previous doubling rate.

To achieve the process results required, the OEM's and integrated device manufacturers (IDM's) need new measurement techniques that will feed into sophisticated machine learning control systems for advanced process control. As new materials are developed for advanced processes these materials need precise characterization of their stability and purity for the process environment. From the point of view of a process or equipment engineer, every subsystem on the tool must work at such a high-level of precision that they cannot leave any factor uncontrolled or not understood. What this means for HORIBA is there are many areas where we can contribute to our customers' success by integrating the Semiconductor and the Scientific segments approach to the market. Our vision is to develop a new way of understanding and executing in the Semiconductor market starting with the materials point of view all the way to process in a so called "Lab to Fab" approach.

The challenges that the semiconductor industry is facing can be addressed with HORIBA's analytical tools and will be used to determine the key measurement techniques that will be needed to measure and control complex device structures. While thin film, wafer inspection and metrology solutions are evolving to keep up with new device dimensions and applications, the new challenge is taking on the increasingly 3D nature of structures as well as 2D materials. To meet the needs of these new materials and devices analytical technologies based on optical, X-ray, electron beam and scanning Atomic Force Microscopy (AFMs) techniques will be required.

Node shrink[*1]   : Refers to the reduction in distance between the Source and Gate in a transistor.
                        The source provides electrons, while the drain collects them.
2D materials[*2] : A new family of materials characterized by a one-monolayer thickness (the size of one atom),
                        such as Carbon Graphene.
2D transistors[*3] : Transistors composed of two-dimensional materials, offering efficient electron transfer and high flexibility.

* Editorial note: This content is based on HORIBA's investigation at the year of issue unless otherwise stated.

2023 堀場雅夫賞　受賞内容

堀場雅夫賞について

堀場雅夫賞は，国内外の大学または公的な試験研究機関において，分析・計測およびその応用に関する科学技術分野で顕著な業績を挙げつつある研究者・技術者を奨励表彰するものです。

対象分野

次世代半導体デバイスの開発に貢献する分析・計測技術

審査講評

2023堀場雅夫賞　審査委員長
東京大学大学院工学系研究科
電気系工学専攻 教授
染谷 隆夫

堀場雅夫賞を受賞された皆様，誠におめでとうございます。心からお慶びとお祝いを申し上げます。審査委員会の委員長として選考過程について報告を致します。本年の堀場雅夫賞は国内18件，海外15件の合計33件の応募がございました。国内外のトップクラスの大学から優れた応募が多数寄せられ，これらは堀場雅夫賞に対する世界のアカデミアからの関心の高さを示しているものと思います。審査におきましては，私を含む7名の審査委員が応募書類全件について審査要領に基づき採点を行ないました。審査ポイントと致しましては学術的，新規性，独創性，次世代半導体デバイスの研究開発，生産プロセス確立への寄与，応募者の将来性，応募研究の学際的，俯瞰的な視点の4つのポイントで評価を行ないました。加えて本賞が分析・計測技術を対象とした賞であることを重視致しまして，新たな分析・計測技術創出への貢献度についても重要な採点のポイントと致しました。書面の審査後，審査委員会を対面で開催し，厳正な審査を経まして堀場雅夫賞の受賞者3名を選出致しました。また，本年は半導体分野での研究としても優れており，かつ将来的には分析・計測技術への展開が大いに期待できる応募がございましたので，特別賞2名を選出致しました。受賞者の研究は，優れた分析計測技術からAIを活用した基礎研究の在り方を示した研究まで，これからの半導体分野の発展に大いに期待できる研究が選ばれました。また，堀場雅夫賞の受賞者3名の所属を見てみますと，これは意図したわけではありませんが，結果として日本，ヨーロッパ，アメリカから各1名の受賞者が選出されました。19回の歴史と伝統を得て，文字通り国際的な賞であることの本賞の重みを審査委員長として，私も実感した次第でございます。以上，簡単ではございますが，受賞された方々の今後のますますのご活躍を祈念し，審査報告とさせていただきます。改めまして受賞者の皆様，誠におめでとうございます。

2023堀場雅夫賞 審査委員会 委員 （敬称略，順不同）

審査委員長：染谷 隆夫　　東京大学大学院工学系研究科 電気系工学専攻 教授
審 査 委 員：小林 正宏　　住友電気工業株式会社　シニアフェロー　研究開発本部 技師長
　　　　　　藤村 紀文　　大阪公立大学大学院工学研究科 電子物理系専攻 教授
　　　　　　昌原 明植　　国立研究開発法人 産業技術総合研究所 デバイス技術研究部門 部門長
海外審査委員：陳 永富　　国立陽明交通大学(台湾) 電子物理系 教授
社内審査委員：田中 悟　　株式会社堀場テクノサービス 分析技術本部
　　　　　　　　　　　Analytical & Testing Technology Department マネジャー
　　　　　　Fran ADAR　HORIBA Instruments Incorporated(ホリバ・インスツルメンツ社/米国)
　　　　　　　　　　　Principal Raman Applications Scientist Semi / Scientific Applications

堀場雅夫賞受賞

国立大学法人京都大学大学院工学研究科
電子工学専攻　助教

石井 良太 氏

【受賞研究題目】

**超ワイドギャップ半導体の基礎光物性解明と新機能性発現に向けた
深紫外時空間分解分光法の開拓**

チューリッヒ工科大学　化学・応用バイオサイエンス学部
上級研究員

Naresh KUMAR 氏

【受賞研究題目】

チップ増強光分光法を用いた新規半導体材料のナノスケール化学特性評価

マサチューセッツ工科大学　電気工学・コンピューターサイエンス学科
博士課程

Ang-Yu LU 氏

【受賞研究題目】

機械学習モデルによる単層MoS_2のラマンとフォトルミネッセンスの相関の解明

特別賞受賞

国立大学法人東京大学大学院工学系研究科
電気系工学専攻　教授

竹中 充 氏

【受賞研究題目】

シリコン光回路を用いた光電融合深層学習プロセッサの開発

東海国立大学機構名古屋大学大学院
工学研究科電子工学専攻　講師

久志本 真希 氏

【受賞研究題目】

微細構造計測に向けた小型深紫外レーザー光源の開発

授賞式　2023年10月17日(火)京都大学 国際科学イノベーション棟 シンポジウムホールにおいて

*編集脚注：本内容は特段の記載がない限り，受賞時点での自社調査に基づいて記載しています。

Exploring Optoelectronic Properties of Ultrawide Bandgap Semiconductors and Deep-Ultraviolet Spectroscopy

超ワイドバンドギャップ半導体光電子物性と深紫外分光技術の開拓

ISHII Ryota

石井 良太

Ultrawide bandgap (UWBG) semiconductors have attracted much attention for deep-ultraviolet (DUV) photonics and high-power electronics. However, the physical understanding is in infancy, preventing the potential capacities of UWBG semiconductors to be drawn out. The electronic and optical properties should be fully elucidated using such as DUV spectroscopy. However, one problem stands that DUV spectroscopy itself is immature. Therefore, we have been exploring both DUV spectroscopy and optoelectronic properties of UWBG semiconductors. Herein, we introduce the development of a deep-ultraviolet scanning near-field optical microscope operating at world's shortest wavelength, and discovery of feasible p-type electric conductivity control by Mg doping in AlN using deep-ultraviolet spectroscopy.

深紫外発光デバイスやパワーデバイス用材料として，バンドギャップの極めて大きい超ワイドバンドギャップ半導体材料に注目が集まっている。しかしながら，その評価手段である深紫外分光技術が未成熟であることが超ワイドバンドギャップ半導体光電子物性の理解・制御を阻んでいる。そこで我々は超ワイドバンドギャップ半導体光電子物性と深紫外分光技術の開拓を両輪として研究に取り組んでおり，ここでは世界最短波長で動作する近接場光学顕微鏡の開発と，超ワイドバンドギャップ半導体材料である窒化アルミニウムのp型電気伝導可能性を示した深紫外分光測定結果について述べる。

Introduction

Figure 1 shows the relationship between the lattice constant and bandgap (energy gap) in various semiconductors. In the early days of semiconductor research, materials with a small bandgap, such as Ge, Si, and GaAs, were main research targets. Today, thanks to the basic research on these materials, semiconductor industries have grown into a huge market, and semiconductor electronics has become an indispensable part of our modern society. From around 1970s, basic research on so-called "wide bandgap semiconductors", such as SiC and GaN, began. Owing to the tireless efforts by researchers and engineers, low-loss/high-voltage power devices and high-efficiency white LEDs have been realized. These applications utilizing wide bandgap semiconductors support today's and future energy-saving societies.

Currently, semiconducting materials with even wider bandgap, "ultrawide bandgap (UWBG) semiconductors" are attracting much attention as next-generation materials.
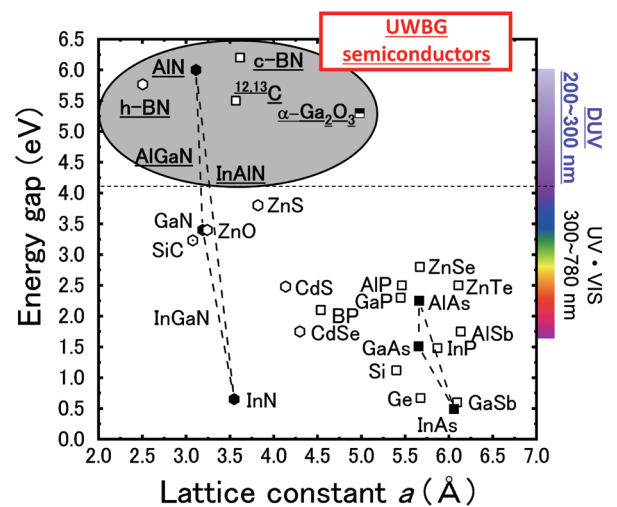

Figure 1 Lattice constant vs energy gap.
(Deep-ultraviolet (DUV) ray: 200~300 nm).

As shown in Figure 1, from the viewpoint of optical devices, deep-ultraviolet (DUV) light-emitting devices can be fabricated using UWBG semiconductors. From the viewpoint of electronic devices, ultrahigh voltage power devices can be realized. Notably, DUV light-emitting devices are capable of inactivating influenza- and corona-viruses, and purifying water (900 million people on earth cannot drink clean water). Therefore, DUV light-emitting devices using UWBG semiconductors are expected to dramatically improve the world's sanitary environment.

However, the external quantum efficiency of DUV LEDs using UWBG semiconductors is currently low (Figure 2). The reasons should originate from such as the immaturity of the bulk crystal growth, epitaxial growth, and device processing technologies. In addition, our group focuses on the lack of the understanding of the optoelectronic properties of UWBG semiconductors such as aluminum nitride (AlN) and diamond.

To draw out the potential capacities of UWBG semiconductors, the electronic and optical properties should be fully elucidated using such as DUV spectroscopy. However, one problem arises that DUV spectroscopy itself is immature[1]. Therefore, we have been studying DUV spectroscopy and optoelectronic properties of UWBG semiconductors. These include the development of a DUV scanning near-field optical microscope (SNOM)[2], intrinsic exciton physics[3] and donor/acceptor impurity physics in AlN[4], recombination processes in AlGaN DUV LEDs[5], and isotopic effects on excitons in diamond[6]. In this manuscript, we will introduce some of our recent works[2,4].

Development of a deep-ultraviolet scanning near-field optical microscope (DUV SNOM)

Classical optics tells that the lateral resolution R is determined by $R=k_1 (\lambda/\mathrm{NA})$, where k_1 is the experimental factor, λ is the optical wavelength, and NA is the

numerical aperture[7]. Therefore, the lateral resolution of lithography has been enhanced by shortening the wavelength of light sources. The immersion argon-fluoride technique (λ=193 nm) has achieved R as small as 40 nm[8]. On the other hand, the lateral resolution of DUV luminescence (fluorescence) spectroscopy is limited at $R>300$ nm[9]. This relatively large value stems from the fact that luminescence spectroscopy requires wider spectral band-widths. In the DUV spectral region, it is very difficult to design an objective lens with a high NA and broadband chromatic-aberration correction[1].

One approach to resolve the issue is luminescence spectroscopy using a SNOM which can overcome the diffraction limit of light[10,11]. Table 1 summarizes the development history of DUV SNOM in literature. The previous DUV SNOM cannot investigate luminescence signals below λ=240 nm due to the constraints. Therefore, we developed a DUV SNOM with an excitation wavelength of 210 nm to overcome the problem. Because of the immaturity of DUV spectroscopy, we designed and built a DUV SNOM from scratch: excitation optical system, objective optical system, scanning probe system, illumination optical system, imaging optical system, and detection optical system.

We used a fourth harmonic generation of a continuous-wave (CW) Ti:sapphire laser as an excitation source. The wavelength was adjusted to 210 nm. Unlike pulsed lasers, CW lasers realized luminescence measurements with a high signal-to-noise ratio. A serious problem in DUV spectroscopy was the temporal deterioration of transmission and reflection optics, which caused the power and pointing instability of the excitation beam. To solve the issue, we constructed a power and pointing stabilizing optical systems composed of two negative-feedback control.

The objective optical system consisted of a custom dichroic mirror and a reflective objective. The reflective
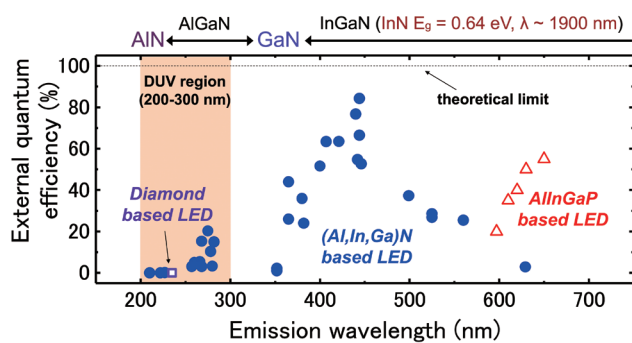
Figure 2 Current status of ultraviolet and visible LEDs.

Table 1 Development history of DUV SNOM (I: illumination, C: collection, PL:photoluminescence,EL: electroluminescence)

References	Excitation λ (nm)	Configuration	R (nm)	Experiment, samples
Sands et al., J. Raman. Spectrosc. **33**, 730 (2002).	244	I mode	200	Raman signals, diamond
Aoki et al., APL **84**, 356 (2004).	266	I mode	50	PL signals, organic materials
Taguchi et al., J. Raman. Spectrosc. **40**, 1324 (2009).	266	I mode	30	Raman signals, diamond
Pinos et al., APL **95**, 181914 (2009).	285	C mode	150	EL signals, AlGaN LED
Pinos et al., JAP **109**, 113516 (2011).	258	I-C mode	100	PL signals, $Al_{0.3\sim0.5}GaN$ layers
Marcinkevičius et al., APL **105**, 241108 (2014).	227	I-C mode	100	PL signals, $Al_{0.6\sim0.7}GaN$ layers

objective did not introduce chromatic aberrations which were ones of the most serial problems in DUV spectroscopy. Compared to a conventional SNOM used in the visible and near-infrared spectral regions, we used a short (3 mm) double-tapered[12] optical fiber probe to ensure a high-throughput transmission of DUV light. The distance between the optical fiber probe and the sample surface was controlled by the shear-force method[13].

The illumination optical system consisted of an incandescent lamp and a liquid light guide with a large core diameter. The beam was collimated by a visible achromatic lens and focused onto an optical fiber probe by a reflective objective. Thanks to the liquid light guide, the image of the optical fiber probe was clearly projected despite the critical illumination optical design.

A DUV imaging lens with a focal length of 105 mm was used in an imaging optical system. The magnification ratio of the imaging optical system was 5.4. The optical fiber probe and sample were imaged by a charged-coupled device camera with UV sensitivity.

The detection optical system consisted of a custom long pass filter and an apochromatic lens with a focal length of 50 mm. The chromatic aberration of this refractive lens was corrected from the DUV to the near-infrared spectral region. The luminescence signals were focused onto the entrance slit of a monochromator, dispersed by a grating, and then electrically detected by a liquid-nitrogen cooled charge coupled device. The whole experimental setup is detailed elsewhere[2].

Figure 3(a) shows the spectrally integrated photoluminescence (PL) intensity mapping images of an $Al_{0.8}Ga_{0.2}N/AlN$ single quantum well structure taken by our DUV SNOM. The strong emission inhomogeneity was observed, which was consistent with the previous cathodoluminescence study[14].

The estimated lateral resolution from **Figure 3**(a) was better than 150 nm. **Figure 3**(b) shows the SNOM-PL spectra of the same sample at room temperature, demonstrating that our DUV-SNOM can detect luminescence signals below λ=240 nm with an excitation wavelength of 210 nm. In conclusion, we developed a DUV SNOM for luminescence spectroscopy which can operate at the shortest wavelength in the world.

P-type electric conductivity control of AlN

Bipolar (*n*- and *p*-type) electric conductivity control is at the heart of semiconductor technologies and has been a major challenge in UWBG semiconductors because of the very high donor and/or acceptor binding energies. In the case of AlN, the *p*-type electric conductivity control by Mg doping is believed to be unfeasible. We casted a doubt on the consensus and experimentally and theoretically revisited the substitutional Mg acceptor binding energy of AlN by means of DUV spectroscopy[4].

Bound exciton PL spectroscopy was conducted using a pulsed ArF excimer laser with an excitation wavelength of 193 nm. The PL signals were dispersed by a 50-cm monochromator and detected by a liquid-nitrogen-cooled charge-coupled device. The spectral resolution was better than 0.7 meV.

Figure 4 shows the PL spectra of unintentionally doped (UID), Si-doped (Si#1), and Mg-doped (Mg#1, Mg#2, and Mg#3) AlN samples at 11 K. The 6.0262 eV (denoted as Γ_5) and 6.039 eV (denoted as Γ_1^L) peaks were assigned to free exciton (intrinsic) emissions, as can be understood from the fact that nearly the same emissions are observed irrespective to Si and Mg doping. On the contrary, the 6.0110 eV peak (denoted as Si^0X) is strongly observed for Si-doped AlN, indicating that the origin is extrinsic (assigned to a neutral Si donor bound exciton). We herein

(a)　　　　　　　　　(b)
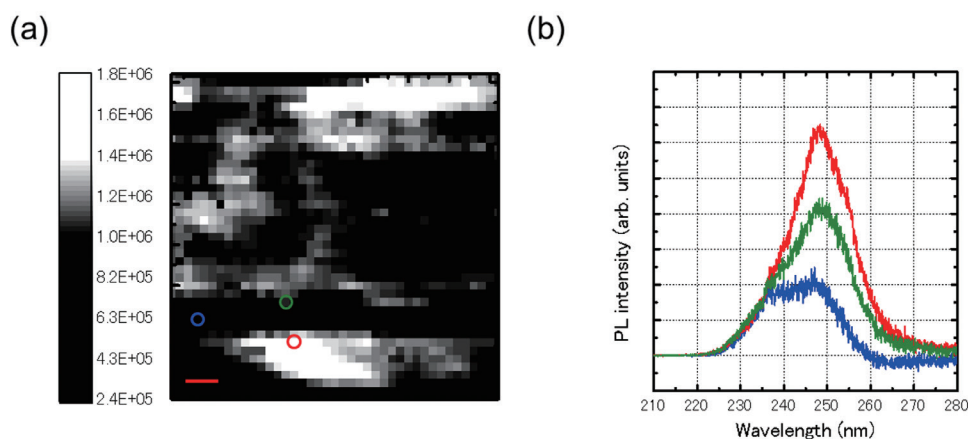
Figure 3　(a) Spectrally integrated PL intensity mapping images (2 μm × 2 μm) of an $Al_{0.8}Ga_{0.2}N/AlN$ single quantum well structure. The red bar denotes 200 nm. (b) The SNOM-PL spectra at room temperature. The color of spectra corresponds to the positions in Figure 3(a).

assigned the 6.0030 eV to a neutral Mg acceptor bound exciton transition (denoted as Mg^0X). The energy difference between the neutral Mg acceptor bound exciton transition and the lowest free exciton transition (Γ_5) was 23.2 meV. Using a well-known empirical rule called Haynes' rule, we tentatively estimated the Mg acceptor binding energy of AlN to 258-390 meV.

We also performed the impurity-related transition luminescence spectroscopy and acceptor-binding-energy calculation using variational methods. The detail is written elsewhere[4]. Our three independent approaches estimated the substitutional Mg acceptor binding energy of AlN to be 330±80 meV which was substantially smaller than the commonly accepted value of at least 500 meV.

Figure 5 summarizes the relation between the room-temperature bandgap and substitutional donor/acceptor binding energies of wide and ultrawide bandgap semiconductors. Because the high *p*-type electric conductivity has been achieved in diamond by boron doping whose acceptor binding energy is 370 meV, our estimated Mg acceptor binding energy of AlN suggested that the *p*-type electric conductivity control by Mg doping is feasible in AlN.

Figure 5   Relation between the room-temperature bandgap and substitutional donor/acceptor binding energies of select wide and ultrawide bandgap semiconductors.

Conclusion

We briefly introduced two of our recent works, the development of a DUV SNOM operating at world's shortest wavelength, and discovery of feasible *p*-type electric conductivity control by Mg doping in AlN using DUV luminescence spectroscopy. We will continue to explore the optoelectronic properties of UWBG semiconductors and DUV spectroscopy to make our future better.

Figure 4   PL spectra of UID, Si-doped, and Mg-doped AlN samples at 11 K.

References

[1] Y. Ozaki and S. Kawata, *"Far- and Deep-Ultraviolet spectroscopy"* (Springer, Japan, 2015).
[2] R. Ishii *et al., APL Photon*. 4, 070801 (2019).
[3] R. Ishii *et al., Phys. Rev. B* 87, 161204R (2013), *Phys. Rev. B* 102, 155202 (2020).
[4] R. Ishii *et al., Jpn. J. Appl. Phys.* 60, 080901 (2021), *Phys. Rev. B* 108, 035205 (2023).
[5] R. Ishii *et al., Appl. Phys. Express.* 13, 102005 (2020), *AIP Adv.* 10, 125014 (2020).
[6] R. Ishii *et al., Jpn. J. Appl. Phys.* 58, 010904 (2019), *Jpn. J. Appl. Phys.* 59, 010903 (2020).
[7] T. Ito and S. Okazaki, *Nature* 406, 1027 (2007).
[8] M. Totzeck, W. Ulrich, A. Göhnermeier, and W. Kaiser, *Nat. Photonics* 1, 629 (2007).
[9] F. Jamme, S. Villette, A. Giuliani, V. Rouam, F. Wien, B. Lagarde, S. Kascakova, S. Villette, F. Allouche, S. Pallu, V. Rouam, and M. Réfrégiers, *Microsc. Microanal.* 16, 507 (2010).
[10] D. W. Pohl, W. Denk, and M. Lanz, *Appl. Phys. Lett.* 44, 651 (1984).
[11] E. Betzig and J. K. Trautman, *Science* 257, 189 (1992).
[12] T. Saiki and K. Matsuda, *Appl. Phys. Lett.* 74, 2773 (1999).
[13] E. Betzig, P. L. Finn, and J. S. Weiner, *Appl. Phys. Lett.* 60, 2484 (1992).
[14] M. Funato, R. G. Banal, and Y. Kawakami, *AIP Adv.* 5, 117115 (2015).

Dr. ISHII Ryota
石井 良太

Assistant Professor,
Department of electronic Science and Engineering,
Kyoto University

Nanoscale Chemical Characterization of Novel Semiconductor Materials using Tip-Enhanced Optical Spectroscopy

チップ増強光分光法を用いた新規半導体材料のナノスケール化学特性評価

Naresh KUMAR

Advancement of next-generation optoelectronic devices and organic photovoltaic (OPV) technologies is underpinned by the development of innovative nanoanalytical tools. In this article, I discuss how our research tackles this challenge by focusing on nanoscale characterization of cutting-edge semiconductor materials including two-dimensional (2D) transition metal dichalcogenides (TMDs) and OPV devices with a unique combination of tip-enhanced optical spectroscopy (TEOS) and electrical-mode atomic force microscopy (AFM). For nanoanalysis of 2D TMDs, we successfully applied TEOS to visualize the distribution of exciton and trion quasiparticles in semiconductors like single-layer (1L) MoS_2, achieving 20 nm-resolution for the first time. Furthermore, by combining TEOS with Kelvin probe force microscopy, we delved into the behavior of grain boundaries in 1L WSe_2, uncovering how their orientation impacts electronic and excitonic properties. For nanoanalysis of OPV devices, we introduced a novel method called simultaneous topographical, electrical, and optical microscopy (STEOM) by combining TEOS with photoconductive-AFM. This allowed us to simultaneously study the surface topography, chemical composition, and electrical properties with sub-20 nm spatial resolution. By applying STEOM to an operating OPV device, we demonstrated direct correlations between surface morphology, nanoscale molecular distribution, and macroscopic device performance. The novel results presented in this article expand the capabilities of optical nanospectroscopy and nanoimaging, shedding light on excitonic processes, material heterogeneity, and device behavior, offering insights crucial for the development of next-gen semiconductor devices. We believe our research in nanoanalytical technologies will facilitate rapid advancements in this field.

次世代のオプトエレクトロニクスデバイスや有機薄膜太陽電池(OPV)技術の進歩は，革新的なナノ分析ツールの開発によって支えられている。ここではチップ増強光分光法(TEOS)と電気特性評価モード原子間力顕微鏡(AFM)を独自に組み合わせ，2次元(2D)遷移金属ジカルコゲナイド(TMD)およびOPVデバイスを含む最先端半導体材料のナノスケール特性評価に焦点を当てることにより，我々がどのように課題に取り組んでいるかについて述べる。まず2次元TMDのナノ解析のために，我々はTEOSを用いて単層(1L)MoS₂のような半導体中の励起子およびトリオンの分布を可視化し，20nmという空間分解能を初めて達成した。次にTEOSとケルビンプローブフォース顕微鏡を組み合わせることで，1L WSe₂の粒界の挙動を掘り下げ，その配向が電子および励起子特性にどのような影響を与えるかを明らかにした。さらにOPVデバイスのナノ解析のためにTEOSと光伝導AFMを組み合わせることで，トポグラフィ・電気・光学同時顕微鏡法(STEOM)と呼ばれる新しい方法を導入した。これにより20nmを切る空間分解能で表面トポグラフィー，化学組成，電気特性を同時に取得することが可能となり，実際に稼働しているOPVデバイスにSTEOMを適用することで表面形状，ナノスケールの分子分布，マクロなデバイス性能の相関関係を実証した。

この論文で紹介する我々の新しい研究成果は光ナノ分光法とナノイメージングの能力を拡張し，励起子プロセス，材料の不均一性，デバイスの挙動に光を当て，次世代半導体デバイスの開発に不可欠な洞察を提供するものである。ナノ分析技術における我々の研究がこの分野における急速な進歩を促進すると信じている。

Introduction

The field of semiconductor devices is rapidly advancing, driven by the demand for high-performance optoelectronic technologies. Two-dimensional (2D) transition metal dichalcogenides (TMDs) and organic photovoltaic (OPV) devices are at the forefront of this revolution. 2D TMD semiconductor materials are composed of a single layer of transition metal atoms (Mo, W, Ga) sandwiched between two chalcogenide atoms (S, Se, Te). They possess unique physical properties, including high electron mobility, large exciton binding energy, and substantial spin-orbit splitting energy. These characteristics make them highly promising candidates for applications in novel optoelectronic devices. Our research specifically focuses on two important members of the 2D TMD family: Single layer (1L) MoS_2 and 1L WSe_2. The exceptional electronic and optical properties of 1L MoS_2 have generated enormous interest for use in 2D optoelectronics, such as photodetectors, solar cells, and light-emitting devices[1]. Unlike graphene, which is a zero band-gap material, MoS_2 exhibits a transition from an indirect band structure in bulk form to a direct band in its 1L structure. This transition results in strong photoluminescence (PL) through excitonic processes. However, the PL process is strongly influenced by various factors, including the local environment, substrate, capping layers, adsorbed molecules, and defects. These factors create non-uniformity within and on the surface of 1L MoS_2, leading to inhomogeneous charge transfer and significant impact on the local population of exciton (exciton) and trion (charged exciton) quasiparticles. To investigate and map these excitonic processes at the nanoscale, we utilized a powerful nanoanalytical tool called tip-enhanced optical spectroscopy (TEOS) that surpasses the limitations of the conventional optical techniques.

Similarly, 1L WSe_2 has attracted significant attention in recent years due to its outstanding optoelectronic properties, positioning it as a promising candidate for various applications, including ultrafast photodetectors, spintronics, light harvesting, light-emitting diodes, and quantum light sources[2]. However, the 1L WSe_2 sheets prepared using chemical vapor deposition are usually polycrystalline in which electronic and excitonic properties are critically influenced by grain boundaries (GBs). Moreover, visualization of the optoelectronic behavior of GBs in the TMDs at nanometer length-scales remains beyond the sensitivity and spatial resolution of the conventional analytical techniques.

Over the last two decades, TEOS, specifically tip-enhanced Raman (TER) and tip-enhanced photoluminescence (TEPL) spectroscopies, have emerged as powerful nanoanalytical tools[3-5]. These techniques overcome the limitations of low sensitivity and spatial resolution of conventional optical analytical tools. By utilizing localized surface plasmon resonance (LSPR) at the apex of a metallic tip, TEOS enhances and confines the electric field to a nanoscopic volume as illustrated in Figure 1. This enhancement enables the observation of excitonic and phononic processes at the nanoscale through intensified local PL and Raman signals. In our first study of 2D TMDs, we employed hyperspectral TEPL imaging to map excitonic processes, including excitons and trions in 1L MoS_2[6]. We achieved an unprecedented spatial resolution
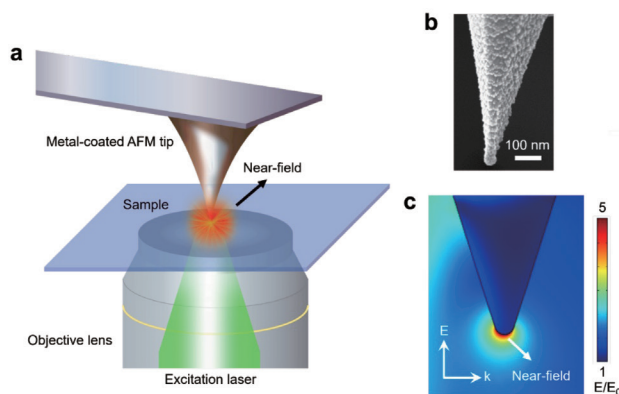
Figure 1   Principle of tip-enhanced optical spectroscopy. (a) A metallic atomic force microscopy (AFM) or scanning tunneling microscopy (STM) tip is placed in the excitation laser spot of an optical microscope. A highly intense electric field localized to a nanoscopic volume (also called near-field) is generated at the tip-apex via LSPR effect, which enhances Raman and PL signals from the sample underneath. By scanning the sample with the near-field, nanoscale Raman and PL images are generated. (b) Scanning electron microscopy image of a representative silver coated AFM TERS probe. (c) Simulated image of the electric field enhancement and localization at the apex of a silver tip. Excitation laser: 532 nm. Figure adapted from reference [8].

of 20 nm, surpassing the confocal optical resolution by a factor of 18. In our second study, we went a step further and demonstrated in situ multiparameter investigation of the optoelectronic behavior of GBs in 1L WSe$_2$ with 50 nm resolution using an innovative combination of light-sensitive Kelvin probe force microscopy (KPFM) and TEOS[7].

In addition to 2D TMDs, our research also addresses the nanoscale characterization of OPV devices. OPV devices have experienced a significant increase in efficiency in recent years, driven by a growing recognition of the crucial role played by the nanomorphology of the active layer in determining device performance[9]. An OPV device comprises two electrodes enclosing an active layer, which is a blend of organic semiconductor materials such as a conjugated polymer (Donor) and a fullerene derivative (Acceptor). Light absorption generates bound excitons that must be dissociated at the Donor-Acceptor heterojunction for efficient charge generation. However, the limited exciton diffusion length in organic semiconductors necessitates optimizing the domain structure within the Donor-Acceptor blend films. This optimization entails achieving efficient charge generation (via exciton dissociation) by controlling the domain structure while ensuring well-connected pathways for charge collection. Coarse phase-separated morphologies (>100 nm) in Donor-Acceptor blends yield low device efficiency due to inadequate charge generation. On the other hand, excessive intimate phase mixing hampers device performance due to inefficient charge collection.

Previous studies have utilized surface imaging techniques like AFM to correlate solar cell performance with the apparent size of observed phase-separated domains. However, the rationale behind relating domain size to device performance lacks consistency and is poorly understood due to the lack of correlative molecular information. Furthermore, conventional optical techniques are limited in their sensitivity and spatial resolution, making it challenging to achieve nanoscale characterization. To address these challenges, we introduced a novel methodology called "simultaneous topographical, electrical, and optical microscopy" (STEOM), which combines TEOS with photoconductive- AFM (PC-AFM) enabling simultaneous characterization of the topographical, electrical, and optical properties of OPV devices at the nanoscale[10]. This innovative approach provides rich correlative information, enabling a comprehensive understanding of the intricate interplay between the local nanomorphology, chemical composition, and photocurrent generation.

Results and Discussion

Nanoscale Characterization of 2D TMDs

In our first study of 2D TMDs, we applied hyperspectral TEPL and TERS imaging techniques to investigate 1L MoS$_2$ (Figure 2(a)) at the nanoscale for the first time[6]. In 1L MoS$_2$, light absorption generates exciton and trion quasiparticles, which are schematically depicted in Figure 2(b). The relative population and energy of the excitons and trions can be measured from the optical spectrum of 1L MoS$_2$, which is depicted in Figure 2(c). The optical spectrum also shows Raman bands, which provide fingerprint information about the vibrational modes. We first examined the effect of silver- and gold-coated AFM probes on the local excitonic processes and electronic population in 1L MoS$_2$. The silver-coated probes exhibited enhanced trion signals in TEPL measurements, while the gold-coated probes displayed enhanced neutral exciton signals. These disparate behaviors resulted from the lower work function of silver (4.3 eV) and the higher work function of gold (5.1 eV) compared to 1L MoS$_2$ (4.7 eV).

Using hyperspectral TEOS imaging, we demonstrated combined nanoscale Raman and PL imaging of a 1L MoS$_2$ sheet for the first time as shown in Figures 2(d) and (e). Furthermore, hyperspectral TEPL imaging allowed visualization of the spatial distribution of neutral excitons and trions in the 1L MoS$_2$ sheet. Intriguingly, excitons and trions exhibited distinct spatial characteristics at the nanoscale. While trions appeared uniformly distributed across the pristine 1L MoS$_2$ sheet (Figure 2(f)) excitons displayed significant spatial variations (Figure 2(g)). These results suggest that local environmental factors, including the substrate, adsorbates, and structural defects, contribute to non-uniform variations in exciton and trion populations in 1L MoS$_2$ that can potentially impact the performance of excitonic devices such as excitonic interconnects. Furthermore, we achieved an unprecedented spatial resolution of 20 nm in TEPL imaging, highlighting the capability of this powerful nanoanalytical tool to provide valuable insights into local changes in the distribution of excitons and trions within 1L MoS$_2$.

In our second study, we joined forces with Dr. Ophélie Lancry and Dr. Marc Chaigneau of Horiba Scientific, France to advance the current state-of-the-art in nanoscale characterization of 2D TMDs. We examined the in-situ light-sensitive electronic and excitonic behavior of GBs in merged 1L WSe$_2$ sheets with a unique combination of TEOS and KPFM using the experimental setup depicted in Figure 3(a)[7]. An optical image of the 1L WSe$_2$ sheets grown using chemical vapor deposition (CVD) is shown in Figure 3(b). Using in-situ TEOS and KPFM imaging, we were able to obtain correlative TEPL, topography, surface potential and capacitance images of the same 1L
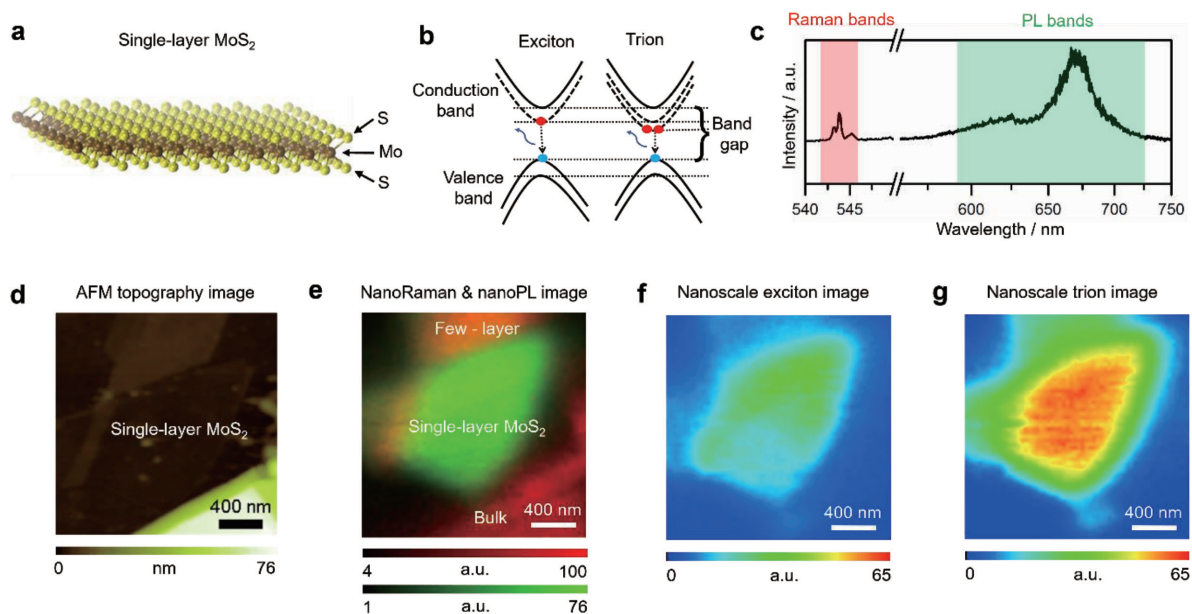
Figure 2 Nanoscale imaging of excitonic processes in 1L MoS₂. (a) Schematic illustration of a 1L MoS₂ sheet, which consists of a layer of Mo atoms sandwiched between two layers of S atoms. (b) Schematic illustration of the exciton and trion formation in 1L MoS₂. Exciton formation occurs when photon absorption generates an electron-hole pair in the conduction and valence bands of 1L MoS₂. Trion formation occurs when photon absorption generates a quasiparticle where two electrons in the conduction band are bound to one hole in the valence band. Trions are also called charged excitons and have lower energy than excitons. (c) Optical spectrum of 1L MoS₂ displaying Raman and PL bands. Raman bands provide fingerprint information about the vibrational modes, whereas PL bands provide information about the relative population and energy of excitons and trions in 1L MoS₂. (d) AFM topography image of a 1L MoS₂ sheet on glass substrate prepared via mechanical exfoliation. (e) Overlay of the TERS (red) and TEPL (green) images of the 1L Mos₂ region shown in Panel d. A strong PL signal is observed at the location of 1L MoS₂. TEPL images of the (f) exciton and (g) trion signals in the 1L MoS₂ region shown in Panel d. Figure adapted from reference [6].

WSe₂ sample as shown in Figures 3(c-f), respectively. A zoomed-in TEPL image of the 1L WSe₂ sample is shown in Figure 3(g). Through correlative topographical, TEPL and electrical imaging with 50 nm spatial resolution, we discovered that the optoelectronic behavior of GBs in 1L WSe₂ is governed by the orientation of the merged sheets. GBs exhibiting tilt angles of 14°, 18°, 38°, 40°, and 60° demonstrated different electronic and excitonic behaviors at the nanoscale. Specifically, the 14°, 38°, and 40° GBs exhibited a comparatively higher work function, lower capacitance, and greater PL quenching than the 18° and 60° GBs. To comprehend this intriguing behavior, density functional theory (DFT) calculations of the GBs' band structure and density of states were performed. The DFT calculations revealed that the 14°, 38°, and 40° GBs encompassed a larger number of midgap states between the valence and conduction bands (Figure 3(h)) compared to the 18° and 60° GBs (Figure 3(i)). These midgap states facilitate non-radiative recombination of excitons, leading to

PL quenching, and the entrapment of charges, resulting in a relatively higher work function in the 14°, 38°, and 40° GBs.
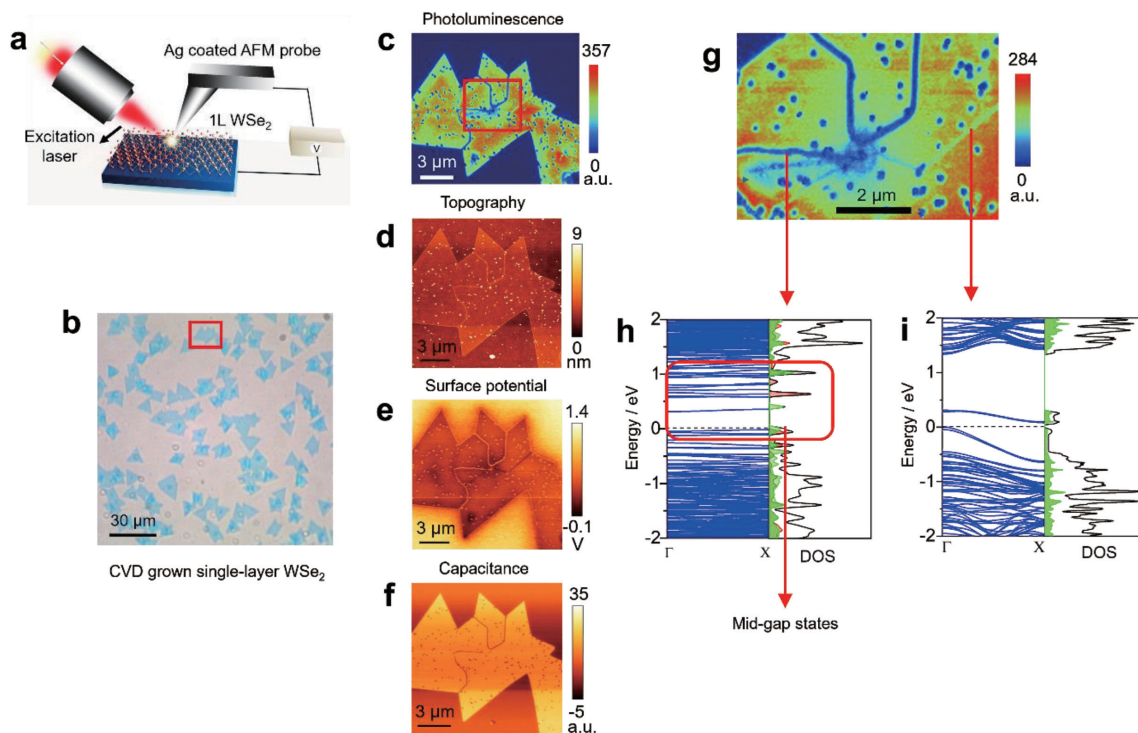
Figure 3 Nanoscale investigation of GBs in 1L WSe₂. (a) Schematic diagram of the experimental setup used to study optoelectronic behavior of GBs in 1L WSe₂. In situ KPFM and TEOS measurements performed in the same experimental setup enabled a direct correlation of topographical, excitonic, chemical, and electrical properties at the nanoscale. (b) Optical image of the CVD-grown 1L WSe₂ sheets. (c) TEPL, (d) AFM topography, (e) surface potential and (f) capacitance images of the 1L WSe₂ sheets measured in the region marked in Panel b. (g) Zoomed-in TEPL image of the region marked in Panel c. DFT calculated band structure (left panel) and DOS (right panel) of GBs with tilt angles of (h) 38° and (i) 60°, which are visible in the blue and green contrast in Panel g. The mid-gap states generated in the 38° GB are highlighted. Figure adapted from reference [7].

Nanoscale Characterization of OPV Devices

For nanoscale characterization of OPV devices, we introduced a novel non-destructive method called STEOM that combines plasmonic optical signal enhancement (TEOS) with electrical-mode scanning probe microscopy (PC-AFM) using the setup shown in **Figure 4(a)**[10]. This novel technique enabled the mapping of morphology, chemical composition, and photoelectrical properties with sub-20 nm spatial resolution. We applied STEOM to investigate an operating OPV device based on the blend of poly[(2,1,3-benzothiadiazole-4,7-diyl)-alt-(4,9-dihydro-4,4,9,9-tetraoctylbenzo[1″,2″:4,5;4″,5″:4′,5′]bissilolo[3,2-b:3′,2 b]dithiophene-2,7-diyl)] (C8SiIDT-BT) and 1′,4′-dihydro-naphtho[2′,3′:1,2][5,6]fullerene-C60 (ICMA). The AFM topography image of the C8SiIDT-BT:ICMA solar cell active layer and the molecular structures of C8SiIDT-BT and ICMA are shown in **Figures 4(b) and (c)**, respectively. In the active layer, the C8SiIDT-BT and ICMA molecules act as electron donor and acceptor, respectively. The optical spectrum of the solar cell is depicted in **Figure 4(d)**, which shows Raman (yellow) and PL (green) signals of C8SiIDT-BT and PL (red) signals of ICMA.

STEOM allowed simultaneous imaging of the solar cell active layer topography, donor Raman, donor PL, acceptor PL and photocurrent signals as shown in **Figures 4(e-i)**, respectively. The rich information provided by these multi-parameter images revealed strong correlations between surface and subsurface molecular distribution of C8SiIDT-BT and ICMA, local photocurrent generation, and macroscopic device performance. Our simultaneous topographic, spectroscopic, and electrical measurements unveiled a hierarchical blend nanostructure in the C8SiIDT-BT:ICMA solar cell, with nanoscale photocurrent hotspots and larger islands of high efficiency dispersed within a low-efficiency blend background. Interestingly, the topographic islands displayed high photocurrent generation due to the presence of large ICMA (acceptor) aggregates surrounded by the C8SiIDT-BT (donor) molecules as illustrated in **Figure 5**. The donor: acceptor interface provided efficient charge separation, whilst the large ICMA aggregates provided well-connected pathways for efficient charge collection.
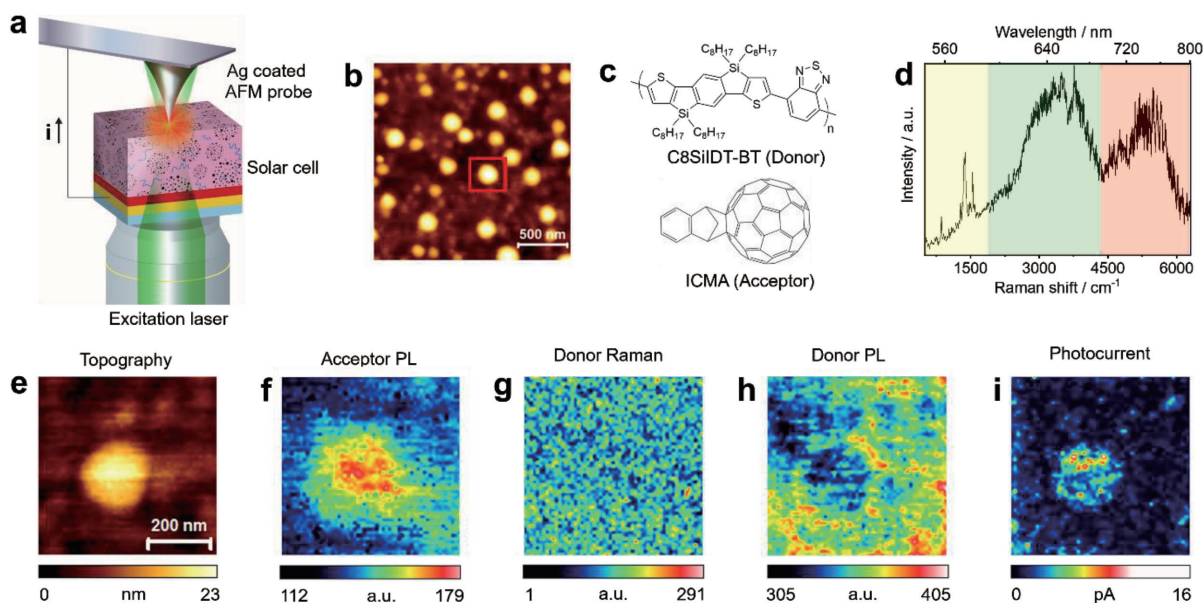
Figure 4 Simultaneous topographical, electrical, and optical microscopy. (a) Schematic diagram of the optical setup used to study operating C8SiIDT-BT:ICMA organic solar cell. (b) AFM topography image of the solar cell active layer containing phase-separated domains of C8SiIDT-BT and ICMA. (c) Structures of C8SiIDT-BT and ICMA molecules, which act as the donor and acceptor in the solar cell. (d) Optical spectrum of the C8SiIDT-BT:ICMA active layer. Raman (yellow) and PL (green) bands of C8SiIDT and PL (red) band of ICMA are highlighted. (e) Topography, (f) acceptor PL, (g) donor Raman, (h) donor PL and (i) photocurrent images measured simultaneously in the region marked in Panel b under operating conditions. Figure adapted from reference [10].
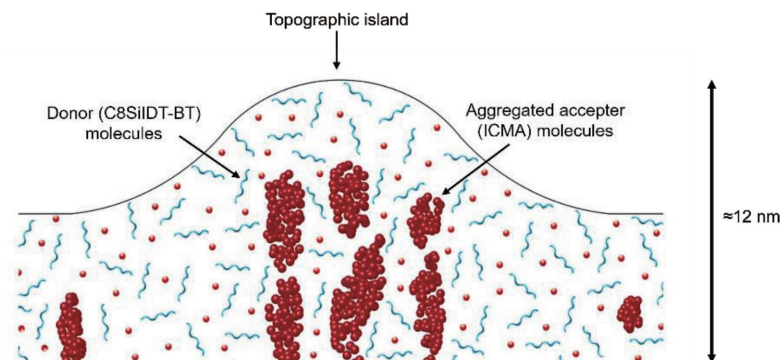
Figure 5 Schematic depiction of the chemical composition in and around a topographic island at the C8SiIDT-BT:ICMA active layer surface revealed using STEOM. Figure adapted from reference [10].

Furthermore, STEOM could distinguish between high purity and lower purity aggregates of ICMA, providing insights into their impact on photocurrent generation and collection. Importantly, we showed that the nanoscale multi-parameter measurements of C8SiIDT-BT:ICMA solar cell are consistent with and can successfully explain the macroscopic device performance. These results validated the ability of STEOM to directly correlate nanoscale characteristics with macroscopic device performance, thus providing a powerful tool for understanding and optimizing OPV devices.

Conclusions and Outlook

In summary, our work focuses on the nanoscale investigation of two classes of novel semiconductor materials, namely, 2D TMDs and OPV devices. As discussed in this article, through our research, we have discovered new insights into the nanoscale properties of these cutting-edge semiconductor materials and demonstrated a novel nanoscale characterization methodology that has the potential to contribute significantly to the advancement of next-generation semiconductor devices.

In 2D TMDs, our research has provided valuable insights into the nanoscale properties of semiconductor materials like 1L MoS_2 and 1L WSe_2. By utilizing TEOS, we have

overcome the limitations of conventional techniques and achieved unprecedented spatial resolutions, enabling the mapping of excitonic processes at the nanoscale. This breakthrough in understanding the behavior of excitons, trions, and grain boundaries in 2D TMDs paves the way for the development of high-performance optoelectronic devices. The ability to manipulate and control the excitonic behavior at the nanoscale opens new avenues for applications in areas such as photodetectors, solar cells, light-emitting diodes, and quantum light sources. The insights gained from our research will likely inspire further exploration and innovation in the field, leading to the design and fabrication of more efficient and advanced semiconductor devices.

Similarly, our research on the nanoscale characterization of OPV devices using STEOM has significant implications for the advancement of organic photovoltaic technologies. The ability to probe the morphology, chemical composition, and photoelectrical properties of OPV devices at the nanoscale provides a comprehensive understanding of the structure-property relationships crucial for device performance. This knowledge can drive the optimization of the active layer's nanomorphology, leading to improved charge generation and collection efficiency in OPV devices. By enabling a direct correlation between nanoscale characteristics and macroscopic device performance, STEOM offers a powerful tool for the rational design and development of high-efficiency OPV devices.

The perspectives resulting from our research contribute to the broader scientific community and semiconductor industry. The innovative methodologies and techniques we have demonstrated push the boundaries of nanoscale characterization and provide researchers with new tools for investigating the properties and behavior of semiconductor materials. The ability to visualize and understand excitonic processes in 2D TMDs and the nanoscale characterization of OPV devices offer critical insights for optimizing their performance and pushing the limits of their efficiency. We anticipate that these advancements will facilitate the development of environmentally friendly and sustainable energy solutions, such as high-performance solar cells and energy-efficient optoelectronic technologies.

Acknowledgements

References

[1] Li X., Zhu H., Two-dimensional MoS2: Properties, preparation, and application. *J. Mater.*, 2015, 1, 33-44

[2] Eftekhari A., Tungsten dichalcogenides (WS2, WSe2, and WTe2): materials chemistry and applications. *J. Mater. Chem.* A, 2017,5, 18299-18325

[3] Mrđenović D., Cai Z.-F., Pandey Y., Bartolomeo G. L., Zenobi R., Kumar N., Nanoscale chemical analysis of 2D molecular materials using tip-enhanced Raman spectroscopy. *Nanoscale*, 2023, 15, 963-974

[4] Cai Z.-F., Kumar N., Zenobi R., Probing On-Surface Chemistry at the Nanoscale Using Tip-Enhanced Raman Spectroscopy. *CCS Chem.*, 2023, 5, 55-71

[5] Kumar N., Weckhuysen B. M., Wain A. J., Pollard A. J., Nanoscale chemical imaging using tip-enhanced Raman spectroscopy. *Nature Protocols*, 2019, 14, 1169-1193

[6] Su W., Kumar N., Mignuzzi S., Crain J., Roy D., Nanoscale mapping of excitonic processes in single layer MoS2 using tip-enhanced photoluminescence microscopy. *Nanoscale*, 2016, 8, 10564-10569

[7] Su W., Kumar N., Shu H., Lancry O., Chaigneau M., In situ Visualization of Optoelectronic Behavior of Grain Boundaries in Monolayer WSe2 at the Nanoscale. *J. Phys. Chem.* C, 2021, 125, 26883-26891

[8] Kumar N., Mignuzzi S., Su W., Roy D., Tip-enhanced Raman spectroscopy: Principles and applications. *EPJ Tech. Instrum.*, 2015, 2, 9

[9] Hu et al., A critical review on semitransparent organic solar cells. *Nano Energy*, 2020, 78, 105376

[10] Kumar N., Zoladek-Lemanczyk A., Gilbert A., Tuladhar S. M., Kirchartz T., Schroeder B. C., McCulloch I., Nelson J., Roy D., Castro F. A., Simultaneous topographical, electrical and optical microscopy of optoelectronic devices at the nanoscale. *Nanoscale*, 2017, 9, 2723-2731

Dr. Naresh KUMAR

Senior Scientist and Lecturer,
Department of Chemistry and Applied Biosciences,
ETH Zurich

Unraveling the Correlation Between Raman and Photoluminescence in Monolayer MoS₂ Through Machine Learning Models

機械学習モデルによる単層MoS₂のラマンとフォトルミネッセンスの相関の解明

Ang-Yu LU

Transition metal dichalcogenides (TMDCs) show strong, tunable photoluminescence (PL), advancing optoelectronic applications. Raman spectroscopy, which is crucial for analyzing 2D materials, discerns crystallinity and material variations such as doping and strain. Nonetheless, the hidden PL-Raman correlations in MoS_2 monolayers are not fully studied. This work methodically investigates PL-Raman interconnections, clarifying the underlying physical mechanisms. Employing machine learning, we differentiate strain and doping effects in Raman data. A DenseNet model predicts PL from Raman maps, while gradient-boosted trees with SHAP assess Raman features' PL influence, elucidating MoS_2's strain and doping. This research offers a machine learning-based methodology for 2D material characterization and informs the tuning of semiconductors for enhanced PL.

遷移金属ジカルコゲナイド（TMDC）は高輝度かつ変化するフォトルミネッセンス（PL）を示し，オプトエレクトロニクス応用を前進させるだろう。ラマン分光法は2次元材料の分析に不可欠であり，結晶性やドーピングやひずみなどの材料変化を解析することができる。にもかかわらず，MoS₂単分子膜における隠れたPL-ラマン相関は十分に研究されていない。本研究ではPL-ラマン相関を系統的に調べ，その奥にある物理メカニズムを明らかにする。機械学習を用いてラマンデータのひずみとドーピングを識別する。DenseNetモデルにより，ラマンマップからPLを予測し，SHAPによる勾配ブースティングツリー（GBT）によりラマンの特長，PLへの影響を評価し，MoS₂のひずみとドーピングを解明することができる。この研究は2次元材料特性評価のための機械学習ベースの方法論を提供し，PL増強のための半導体のチューニングに役立つ。

Introduction to MoS₂ Monolayers and Machine Learning Models

Two-dimensional (2D) materials, distinguished by their ultra-thin structure and high surface-to-volume ratio, exhibit unique physical and chemical characteristics. Among these, monolayer transition metal dichalcogenides (TMDCs) are 2D semiconductors known for their adjustable photoluminescence (PL). This PL can be altered through external factors like strain and doping. For instance, MoS_2, a type of TMDC, shows adjustable band structures and broad-spectrum optical absorption when subjected to strain. These properties make it highly suitable for various advanced applications, such as cutting-edge photovoltaic systems[1] and quantum information science technologies, including single-photon emission[2]. Additionally, the near-perfect PL quantum yield in MoS_2,

achieved through either chemical[3] or electrostatic doping[4], paves the way for creating highly efficient light-emitting diodes[5] and lasers[6]. To analyze these external influences, Raman spectroscopy is employed as an effective and non-invasive method to measure the impact of strain and doping on the properties of MoS_2. While Raman and photoluminescence (PL) spectroscopy have been instrumental in exploring strain and doping effects in MoS_2, the majority of research has treated these effects separately. Discovering the hidden correlations between Raman and PL spectra can enable us to understand the strain and doping effects comprehensively. Recently, the rise of machine learning has revolutionized fields such as computer vision and natural language processing and has made significant inroads in diverse scientific disciplines, including biology[7], mathematics[8], and material science[9]. Although machine learning approaches have been utilized

in research on 2D materials, these efforts remain in the nascent stage[10,11] and hold potential for groundbreaking discoveries.

In this study, we leveraged an array of machine learning algorithms to uncover the hidden patterns linking Raman and PL spectra in MoS_2, providing insights into the physical mechanisms connecting PL and Raman features. Our approach started with the implementation of a DenseNet model, which demonstrated high predictive accuracy for PL features from Raman spectral maps. Subsequently, we integrated a gradient-boosted model with SHapley Additive exPlanations (SHAP) to correlate Raman and PL data, offering both global significance and local interpretability in terms of feature contributions. Lastly, we projected MoS_2 Raman features on frequency scatter plots to decompose strain and doping effects. Our findings illustrate the potent capability of machine learning tools in elucidating complex relationships across different material characterization techniques.

The conceptual illustration provided in Figure 1(a) shows the trajectory of knowledge acquisition through machine learning models (represented by the red line), commencing from the results of material characterization, progressing through established material knowledge, and culminating in the understanding of external perturbations and defect structures. This methodology enables the integration of prior investigations-those that examined changes in Raman and PL spectra due to single external effects such as strain (indicated by the green line) or doping (denoted by the blue line)-into a comprehensive understanding of MoS_2 monolayers. Additionally, the employment of statistical data analysis within our framework serves to reduce potential biases arising from sample selection and experimental setup. By integrating statistical analysis with machine learning, our model

creates a robust connection between Raman and PL characteristics, the crystalline and electronic structures, as well as the effects of strain and electrostatic doping.

Synthesis and Characterization of MoS₂ Monolayers

MoS_2 monolayers are synthesized through chemical vapor deposition (CVD) on 300 nm SiO_2/Si substrates, utilizing molybdenum trioxide (MoO_3) and sulfur (S) powders, each weighing 20 mg, as source materials. Substrates are prepared with a spin-coated layer of Perylene-3,4,9,10-tetracarboxylic acid tetrapotassium (PTAS) solution, which acts as a seeding promoter. To ensure an oxygen and moisture-free environment, the CVD system is flushed with an Argon (Ar) flow of 1000 sccm for 5 minutes. The temperature of the furnace is increased to 625°C at a rate of 30°C per minute. Concurrently, sulfur is maintained at 180°C in an upstream position within the system. The growth of MoS_2 monolayers occurs at 625°C under atmospheric pressure for 3 minutes, with an Ar flow of 20 sccm and an O_2 flow ranging from 0 to 1 sccm, serving as the carrier and reactant gases, respectively. Post-growth, the furnace is allowed to cool to room temperature naturally under a continuous Ar flow of 1000 sccm to avert any additional unintended chemical reactions. The MoS_2 crystals were obtained from SPI Supplies and 2D semiconductors, and then mechanically exfoliated and deposited onto a 300 nm SiO_2/Si substrate. The SPI crystals were naturally grown, while the 2D semiconductor crystals were synthetic. The exfoliated flakes were termed natural and synthetic, accordingly.

We employed the HORIBA LabRAM HR800 spectrometer for Raman and photoluminescence (PL) characterizations, utilizing a 532 nm (2.33 eV) laser source. Due to time constraints associated with each spectral mapping,
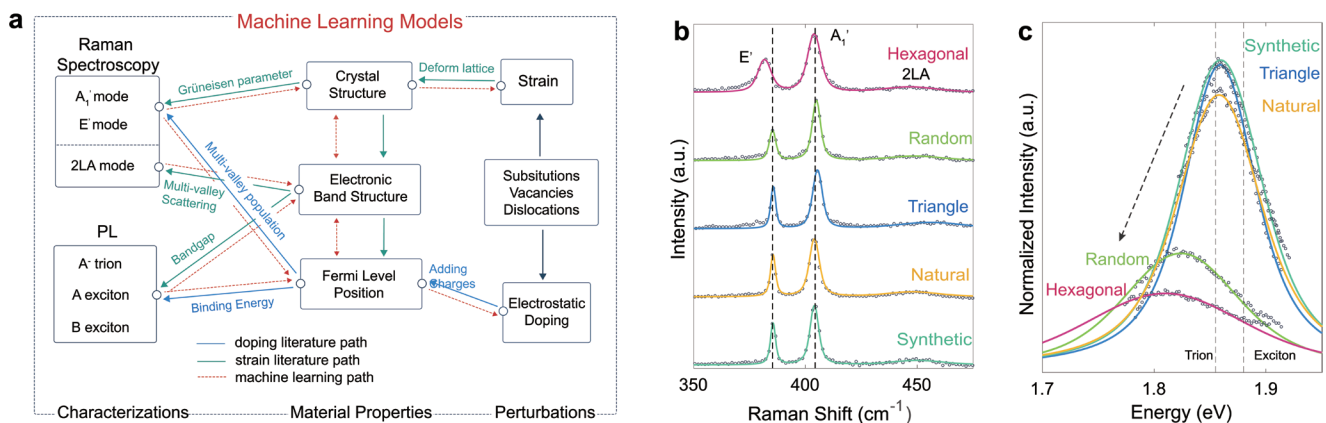
Figure 1 (a) Overview of unraveling correlation between Raman and PL with external perturbations. The green and blue lines correspond to the studies of strain and doping effects, respectively. The red dashed line indicates the discovering path by the machine learning models in this work. (b-c) Raman and PL spectra of CVD-grown MoS₂ monolayers. (b) Raman, and (c) PL spectra of CVD-grown (hexagonal, random, and triangle) and exfoliated (natural and synthetic) MoS₂. The vertical dashed lines denote the Raman E' and A'_1 frequencies for the synthetic MoS₂ in a and the MoS₂ exciton energy of 1.86 and 1.89 eV for trion and exciton, respectively.

the laser power was carefully maintained at approximately 1 mW, and the acquisition time was set to 0.5 seconds.

For our spectral maps, we collected data across 1,600 pixels, corresponding to a spatial dimension of 40 by 40. This process required approximately 30 minutes per spectral map. Consequently, the complete measurement of a single MoS$_2$ crystal, including the necessary system calibrations, amounted to over 1.5 hours. Our Raman and PL measurements utilized a 100X objective lens, which focuses the laser to a 1 μm diameter spot size. The normalization of Raman spectra was conducted against the intensity of the silicon (Si) peak, with calibration referring to the Si Raman frequency established at 520.6 cm^{-1}. We employed spectral gratings of 1,800 grooves per millimeter (gr/mm) for Raman and 300 gr/mm for PL measurements to ensure high-resolution spectral data. The spatial dimensions for the Raman and PL mapping were tailored to match the domain size of the MoS$_2$ flakes under investigation, with a spatial resolution of 1 μm achieved through the precision control of a motorized stage.

The Raman spectra of MoS$_2$ monolayers are characterized by three characteristic features as illustrated in Figure 1(b), which represent the in-plane E' mode at approximately ~385 cm^{-1}, the out-of-plane A'_1 mode near 405 cm^{-1}, and the second-order double resonance 2LA mode around 450 cm^{-1}. These vibrational modes are precisely defined using a Voigt profile for the extraction of key parameters: the frequency (Freq, ω), the full-width-at-half-maximum (FWHM, Γ), and the intensity (Int, I). Figure 1(b) displays the frequency distribution for these modes across the MoS$_2$ monolayers sampled, highlighting a trend of frequency softening for the $\omega_{A'_1}$ mode in naturally-grown MoS$_2$ and for the $\omega_{E'}$ mode in hexagonal-shaped MoS$_2$, in comparison to those exfoliated from synthetic sources. In the context of PL characterization, trions appear to dominate the PL response from MoS$_2$ due to the ~1 mW laser power utilized during our experiments. A closer evaluation of Figure 1(c) indicates that MoS$_2$ flakes with hexagonal and random shapes tend to show lower PL energy, wider FWHM, and reduced intensity in contrast to triangle-shaped and mechanically exfoliated MoS$_2$ crystals.

For the analysis of spectral data, a curve-fitting routine was executed within a Python environment. This routine involved the subtraction of background noise from the spectra by employing the BaselineRemoval package, specifically utilizing the ZhangFit method[12]. To accurately fit the spectral lines, we utilized the Voigt profile function, accessible from the Scipy library, which is defined by a quartet of parameters: the frequency of the Raman feature, σ (which is the standard deviation of the Gaussian

component of the Voigt profile), γ (representing the half-width at half-maximum of the Lorentzian component), and the intensity of the Raman feature. For optimization purposes, the least-squares optimization function from the Scipy library was engaged. The full width at half-maximum (FWHM) is then computed by applying the following equation (1-3):

$$f_G = 2\sigma\sqrt{2ln2} \qquad (1)$$

$$f_L = 2\gamma \qquad (2)$$

$$\Gamma \approx 0.5346f_L + \sqrt{0.2166f_L^2 + f_G^2} \qquad (3)$$

This equation effectively combines the contributions from both the Gaussian and Lorentzian components that make up the Voigt profile, giving a comprehensive measure of the spectral line's width at its half-maximum intensity. Upon capturing the Raman and PL spectra, we channeled the data through a curve-fitting process. Each spectral peak was modeled with a Voigt profile, which yielded three primary parameters: the peak frequencies, the FWHM, and the intensities. We then normalized all characteristic peaks using the intensity of the Raman signal at 520.6 cm^{-1} from the silicon substrates. For MoS$_2$ monolayers with a normalized intensity of the A'_1 mode ($I_{A'_1}$) less than 0.5, we applied a stringent threshold to demarcate regions attributed to multilayer MoS$_2$. Meanwhile, outliers identified in the spectral maps were subsequently eliminated using a binary opening operation.

In the development of our machine learning models - specifically XGBoost and the support vector machine (SVM)-we utilized a total of 7,023 data points. The DenseNet model's training dataset comprised all pixel data, inclusive of those with and without Raman/PL signals. Data augmentation was performed by applying a 90-degree rotation to the pixel maps, accumulating in a dataset encompassing 35,596 patched maps. Statistical analysis was conducted using Matlab and Python, incorporating libraries such as Pytorch, Scipy, and Numpy to facilitate the analysis.

Statistical Analysis for MoS$_2$ Monolayers

To further elucidate the characteristics of PL in MoS$_2$, we graphed the PL FWHM against the normalized PL intensity, as depicted in Figure 2(a). This graph demonstrates a discernible trend: higher PL intensities are associated with narrower PL FWHMs, a pattern typically observed in synthetic and triangle-shaped MoS$_2$ crystals, as shown in Figure 2(b). The PL FWHM (Γ_{PL}) can be represented by a reciprocal relationship with PL intensity (I_{PL}) as shown in Equation (4), which plots as the blue curve in Figure 2(a). When considering potential discrepancies
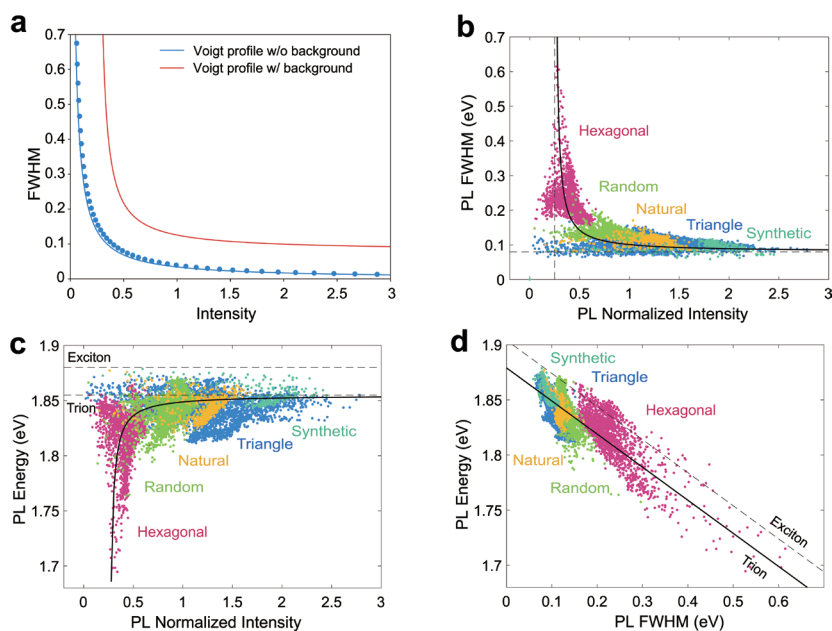
Figure 2 Scatter plots for PL features for MoS₂ monolayers. (a) The correlation between FWHM and intensity in a Voigt function for a fixed area of 0.1 without (blue, Equation (4)) and with (red, Equation (5)) the background. (b) PL FWHM as a function of the normalized intensity following the multiplicative inverse function (solid-black line) described by Equation (5). (c) PL energy as a function of the normalized intensity following the reverse multiplicative function (solid-black line) described by Equation (6). (d) PL energy as a function of the PL FWHM following a linear function (solid black) described by Equation (7).

due to imperfect background subtractions in the spectral data, we adjusted the equation to include an offset for both intensity and FWHM, resulting in Equation (5). This adjusted model corresponds to the red curve seen in Figure 2(a) and aligns well with the distribution observed in Figure 2(b). In addition, we explored the relationship between PL energy (E_{PL}) and intensity (I_{PL}) as shown in Figure 2(c). As the PL spectrum was fitted using a Voigt profile with a fixed integrated area, a reverse reciprocal function illustrated by Equation (6) was employed, indicating that stronger PL intensities are associated with higher PL energies. Moreover, a linear relationship between PL energy and FWHM is depicted in Equation (7), and this is graphically represented in Figure 2(d).

The collective interpretation of these findings suggests that the triangular, as well as natural and synthetic MoS₂ flakes, display PL peaks that are more intense, sharper, and exhibit a blue shift, signaling a higher crystal quality when compared to the random and hexagonal MoS₂ flakes.

$$\Gamma_{PL} = 0.0157/I_{PL} \quad (4)$$
$$\Gamma_{PL} = 0.0157/(I_{PL} - 0.25) + 0.08 \quad (5)$$
$$E_{PL} = 1.855 - 0.0047/(I_{PL} - 0.25) \quad (6)$$
$$E_{PL} = 1.879 - 0.3 * \Gamma_{PL} \quad (7)$$

High Performance of DenseNet

To unravel the hidden relationships within our Raman and PL data, we employed a variety of machine learning techniques, particularly focusing on revealing hidden patterns

and establishing connections to underlying physical phenomena. Deep convolutional neural networks (CNNs), renowned for their proficiency in a multitude of visual recognition tasks, enable the extraction of valuable insights from diverse imaging systems, encompassing the biomedical[13] to the microscopic[14] and hyperspectral domains[15]. Viewing spectral maps as image-based datasets with multiple channels, such as the number of spectral points. Using CNNs, we correlate the Raman spectra with the corresponding PL features for the CVD-grown and exfoliated MoS₂ flakes.

We chose to deploy Dense Convolutional Networks (DenseNet)[16] for their efficiency in predicting three PL features from the Raman spectral images. DenseNet has been demonstrated to require fewer parameters and less down-sampling compared to other advanced CNN models, such as U-Net[17] and SegNet[18], while still delivering comparable accuracy. This characteristic makes DenseNet particularly advantageous for handling small datasets and small pixelated inputs, aligning perfectly with the scope of our research. The DenseNet architecture[16] implemented in our study was a tailored version of the original design, adapted to comprise two dense blocks. Preceding the entry to the first dense block, the input image undergoes a convolution with an output of 12 channels; the specifics of this step are illustrated in Figure 3(a). Each dense block is constructed with several layers: batch normalization, ReLU activation, convolutions with 1x1 and 3x3 kernel sizes, and is followed by a dropout rate set at 0.1 to prevent overfitting. The transition layer that bridges the two dense blocks includes batch

normalization, a ReLU layer, a convolutional layer with a 1x1 kernel size, and concludes with an average pooling layer. Upon the completion of the final dense block, an adaptive average pooling operation is executed, outputting three channels, which are then connected to a linear layer designed to produce three final output values. The deployment of DenseNet was facilitated through the PyTorch framework. To evaluate the performance of DenseNet, we utilized the relative absolute error, articulated by the following Equation (8):

$$RAE = \frac{[\sum_{i=1}^{n}(y'_i - y_i)^2]^{\frac{1}{2}}}{[\sum_{i=1}^{n} y_i^2]^{\frac{1}{2}}} \qquad (8)$$

In this equation, y'_i represents the predicted values obtained from DenseNet, and y_i denotes the actual experimental values acquired from the PL measurements. This metric allows for the quantification of the prediction accuracy of the network relative to the true data values.

To explore the relationship between the spatial information contained within Raman patched maps and the performance of the DenseNet architecture, we experimented with various sizes of Raman patched maps. These ranged from a local spatial size of 1x1 to a more extensive spatial size of 11x11 for the intensity data of hexagonal MoS_2, an

example of which is shown in Figure 3(b-d). It was observed that the smaller 1x1 patch size yielded a higher error rate of 21.48%, which can be attributed to the limited spatial information provided by the Raman maps. On the other end of the spectrum, the 11x11 patch size resulted in a marginally increased relative error of 11.86%, potentially due to zero padding implemented around the edges of the patched inputs. Out of all the patch sizes tested, the 5x5 configuration achieved the most favorable balance, exhibiting the lowest relative absolute error (RAE) of 10.31% for the PL intensity of a triangle-shaped MoS_2. This particular patch size managed to integrate adjacent Raman signals while avoiding the inclusion of extraneous spatial information.

The central columns of Figure 3(e-g) illustrate typical predictions for PL energy, FWHM, and intensity as derived from the trained DenseNet model when applied to a random-shaped MoS_2 using a 5x5 patch size. For model performance assessment, the experimentally measured PL maps were considered as the benchmark (ground truth), displayed in the left column. The relative errors computed are shown in the right column of Figure 3(e-g). The RAEs for the PL energy and FWHM were notably low, at 0.25% and 4.61% respectively. However, the RAE for PL intensity was higher, recorded at 10.93%, which may be
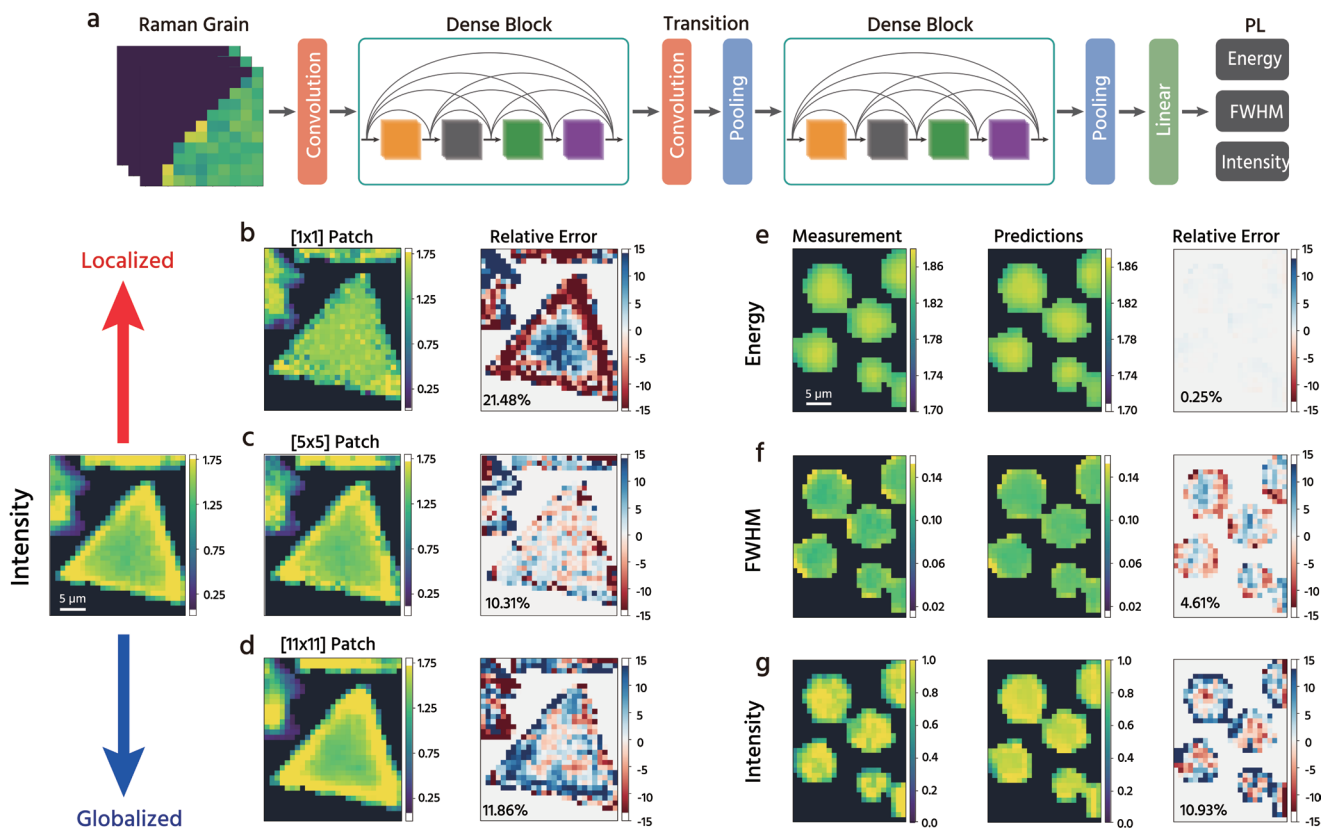
Figure 3   (a) Schematic illustration of a DenseNet model with two dense blocks. (b-d) PL predictions from the trained DenseNet. The patch size effect on the DenseNet for the predicted intensity of a triangle MoS_2. (b) 1-by-1, (c) 5-by-5, and (d) 11-by-11 with 21.48%, 10.31 and 11.86% relative absolute errors, respectively. (e-g) The PL mapping predictions of (e) energy, (f) FWHM, and (g) intensity for CVD-grown MoS_2 with random shape. Left: the measured PL maps as the ground truth for the DenseNet model. Middle: the predicted results by the trained DenseNet with 5-by-5 patch inputs. Right: the relative error between measured and predicted PL maps.

indicative of non-ideal experimental conditions or errors in the data processing stages, including spectroscopic measurements, background spectral subtraction, and the fitting procedures.

XGBoost Model with SHAP Explainer

Although CNNs represent the state-of-the-art model to make inferences on image- or spectral-based tasks, their multilayer nonlinear structures are often criticized as non-transparent and non-explainable[19]. In response to this, we transformed spectral maps into a tabular dataset comprising roughly 7000 discrete data points. An extreme gradient boosting (XGBoost) model, trained on this tabular dataset, was utilized to discern the correlations between Raman characteristics and corresponding PL features in MoS₂ monolayers.

XGBoost, an ensemble learning model constructed from decision trees[20], is widely recognized for its effectiveness in supervised learning tasks, especially when dealing with tabular datasets featuring individually significant attributes that do not incorporate temporal or spatial structures[20]. The optimization of the XGBoost regressor's hyperparameters was conducted via Bayesian Optimization[21], with the model configured to include 700 gradient-boosted trees, a learning rate of 0.05, and a maximum tree depth of 15. Root mean square log error (RMSLE) was employed as the evaluative metric to minimize the impact of outliers on error calculation.

To interpret the XGBoost model predictions and link them to their physical underpinnings, we applied Shapley Additive exPlanations (SHAP)[22], which acts as a tree
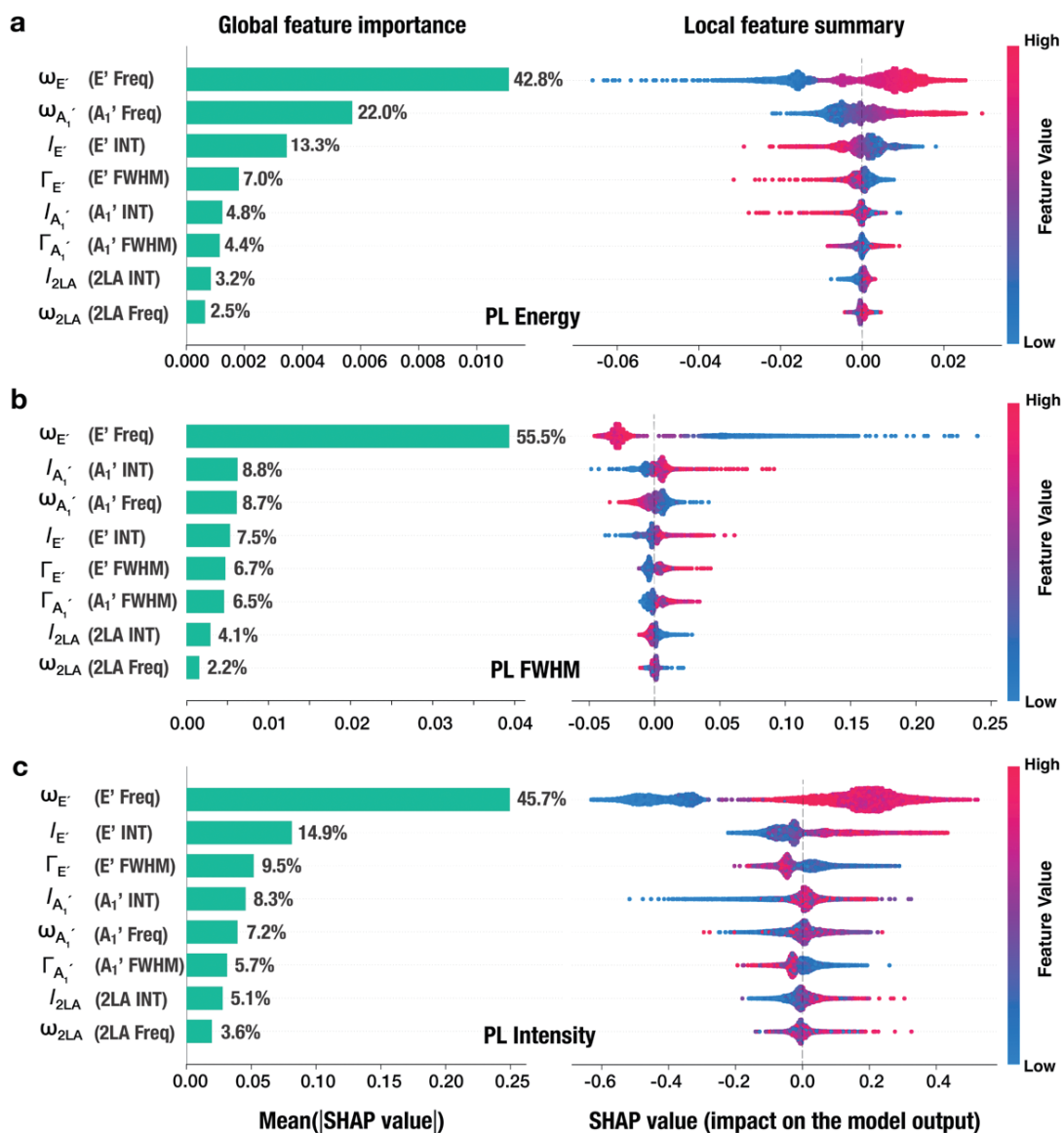
Figure 4   Correlation analysis for Raman and PL by XGBoost with SHAP values. (a) PL energy, (b) PL FWHM, and (c) PL intensity results are interpreted by the trained XGBoost model by Shapley additive explanations (SHAP). The Raman features are sorted in descending order according to global parameter importance. Left: the global importance of Raman features based on the average SHAP value magnitude for PL features. Right: a set of beeswarm plots corresponding to a single pair of Raman and PL. The vertical axis displays the sorted Raman features, while the horizontal axis shows the impact of the model output. Each data point represents a predicted output, and the color indicates the Raman features values.

explainer. SHAP provides both local and global insights based on game theory principles, elucidating the connections between Raman and PL spectra.

In Figure 4, SHAP summary plots visualize the influence of specific Raman feature values on the predicted PL features. Individual dots on these plots represent model predictions, with colors encoding the value of a particular Raman feature. For instance, a higher frequency of the E' Raman mode ($\omega_{E'}$, indicated by a red color) correlates with an increased SHAP value, suggesting a heightened PL energy. Moreover, bar charts in Figure 4 detail the SHAP importance values, offering a global perspective on the contribution of each Raman parameter to the PL features.

Analysis of the SHAP values revealed that the Raman features, $\omega_{E'}$, $\omega_{A'_1}$, and $I_{E'}$ are the most impact factors in predicting PL features. The average SHAP importance for the E', A'1, and 2LA modes with respect to the PL features are 67.6%, 25.5%, and 6.9%, respectively. This distribution of importance is consistent with prior studies indicating that the E' Raman mode is sensitive to in-plane strain but less affected by doping[23], whereas the A'1 mode's

sensitivity is reversed, being more responsive to doping than to strain[23-25]. Given that the E' mode exhibits the most significant SHAP importance (67.6%) for PL prediction, we infer that the PL response within our dataset is predominantly influenced by strain effects rather than doping.

Scatter Plots for Decomposition of Raman Frequencies

The differentiation of strain and doping effects on the vibrational properties of graphene has been established through the shifting of G and 2D band frequencies. Extending this methodology to monolayer MoS$_2$[26,27], the SHAP importance results have highlighted that the frequencies of the $\omega_{E'}$ and $\omega_{A'_1}$ modes predominantly influence the PL characteristics. While similar strategies have been previously applied to MoS$_2$, the hidden details of these physical phenomena have not been fully discerned from the Raman frequency analyses.

In our investigation, we demonstrated the decomposition of strain and doping effects as functions of $\omega_{E'}$ and $\omega_{A'_1}$ in Figure 5(a). We begin by identifying the intrinsic point,
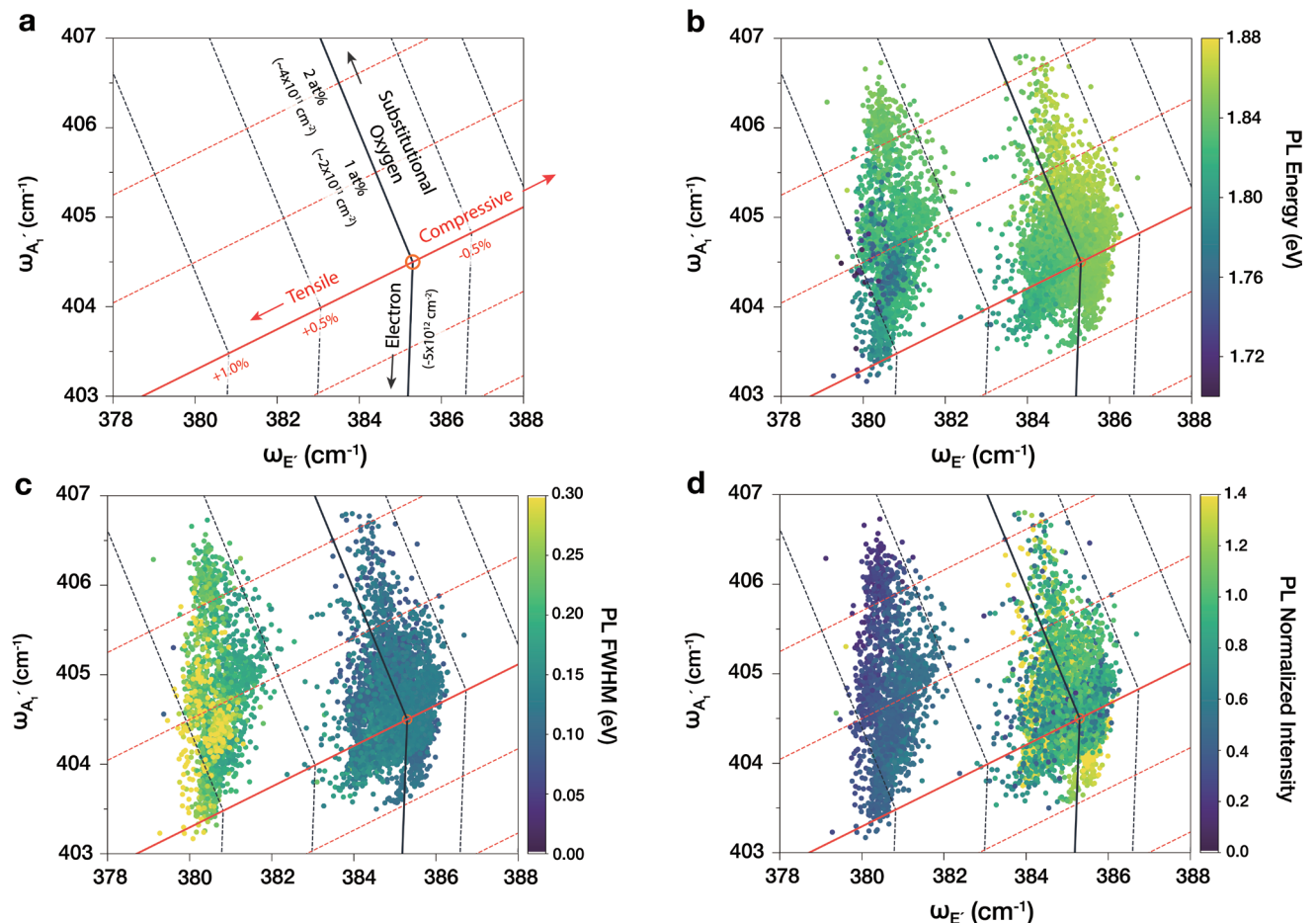
Figure 5 (a) Schematic representation of strain and doping base vectors for ($\omega_{E'}$, $\omega_{A'_1}$) coordinates. The red and black solid line corresponds to strain and doping, respectively. The orange circle is denoted as the intrinsic point, defined as the charge-neutral and unstrained state. (b-d) Scattered plots of CVD-grown and exfoliated MoS$_2$ monolayers on Raman features of $\omega_{A'_1}$ versus $\omega_{E'}$. The coded colors indicate (b) PL energy, (c) PL FWHM, and (d) PL intensity.

which is characterized as the undoped and unstrained state of MoS₂. The intrinsic Raman frequencies of the $\omega_{E'}$ and $\omega_{A'_1}$ modes are somewhat elusive; however, by comparing a range of E' and A'_1 data from both literature and our own studies, we find that most data align with the established frequency difference of $\omega_{A'_1} - \omega_{E'} = 19$ cm^{-1}[28], which is the recognized standard for monolayer MoS₂. We have designated the Raman frequencies from exfoliated synthetic MoS₂, located centrally within our data distribution, as the intrinsic point, marked at (385.3, 404.5) for ($\omega_{E'}$, $\omega_{A'_1}$), respectively. This point is indicated by an orange circle in our representations. Regarding strain effects, we observe that tensile strain induces shifts in the $\omega_{E'}$ and $\omega_{A'_1}$ of 4.48 and 1.02 cm^{-1}/%, respectively. This observation is aligned with the ratio of the Grüneisen parameters of the E' and A'_1 phonons[29]. The impact of compressive strain, for which Raman studies on MoS₂ are scarce, has been inferred from literature, suggesting that Raman frequency shifts due to tensile strain are 1.56 times greater than those due to compressive strain[30]. Doping effects are represented by a black line, with recent studies indicating that the $\omega_{A'_1}$ mode softens with electron accumulation but remains unaltered with hole doping[24]. Thus, the vector for electron doping in the low electron concentration region has been quantified as ($\omega_{E'}$, $\omega_{A'_1}$) is (-0.15, -1.19) cm^{-1}/1013 cm^{-2}[25] as shown in **Figure 5(a)**. The hardening of $\omega_{A'_1}$, potentially caused by substitutional doping during the CVD growth process, is exemplified by shifts of -0.18 and 0.2 cm^{-1}/at% due to substitutional oxygen doping[31]. The scatter plot in **Figure 5(b-d)** of $\omega_{E'}$ and $\omega_{A'_1}$ which considers both strain and doping effects, reveals that the intrinsic point corresponds to higher PL energy, increased intensity, and reduced FWHM. This relationship is visualized with color coding that represents the PL energy, intensity, and FWHM across various data points.

Conclusion

In conclusion, we have demonstrated a framework for capturing the correlations between Raman and PL essential to tune MoS₂ optical properties by external perturbations to understand, predict, and design next-generation devices. We utilize the DenseNet model to build end-to-end connections from Raman spectral maps to photoluminescence. To gain more comprehensive insights into the physical mechanisms of strain and doping effects, we adopt the XGBoost model with the SHAP explainer and reveal that $\omega_{E'}$, $\omega_{A'_1}$, and $I_{E'}$ are the three dominant Raman characteristics for PL feature predictions, which further indicates that the strain effects govern the PL response more than the doping effects in our dataset. We further disentangle strain and doping effects and predict the location of the intrinsic point on the Raman frequency plot. The proposed methodology establishes an analysis

approach to comprehensively interpret experimental observations to explore novel physics, which is suitable for Raman spectra and PL on 2D materials and for many other types of spectroscopies and condensed matter.

[10] K. Tanaka, K. Hachiya, W. Zhang, K. Matsuda, Y. Miyauchi, *ACS Nano* **2019**, *13*, 12687.

[11] Y. Mao, N. Dong, L. Wang, X. Chen, H. Wang, Z. Wang, I. M. Kislyakov, J. Wang, *Nanomaterials (Basel)* **2020**, *10*, 2223.

[12] M. A. Haque, *BaselineRemoval: Python Package Code Repo for BaselineRemoval. It Has 3 Methods for Baseline Removal from Spectra for Baseline Correction, Namely ModPoly, IModPoly and Zhang Fit. The Functions Will Return Baseline-Subtracted Spectrum*, Github, **n.d.**

[13] A. Srivastava, D. Jha, S. Chanda, U. Pal, H. Johansen, D. Johansen, M. Riegler, S. Ali, P. Halvorsen, *IEEE J. Biomed. Health Inform.* **2022**, *26*, 2252.

[14] J. M. Ede, *Mach. Learn. Sci. Technol.* **2021**, *2*, 011004.

[15] B. Fang, Y. Li, H. Zhang, J. Chan, *Remote Sens. (Basel)* **2019**, *11*, 159.

[16] G. Huang, Z. Liu, L. Van Der Maaten, K. Q. Weinberger, in 2017 *IEEE Conference on Computer Vision and Pattern Recognition (CVPR)*, **2017**, pp. 2261-2269.

[17] O. Ronneberger, P. Fischer, T. Brox, *arXiv [cs.CV]* **2015**.

[18] V. Badrinarayanan, A. Kendall, R. Cipolla, *IEEE Trans. Pattern Anal. Mach. Intell.* **2017**, *39*, 2481.

[19] V. Buhrmester, D. Münch, M. Arens, *arXiv [cs.AI]* **2019**.

[20] T. Chen, C. Guestrin, in *Proceedings of the 22nd ACM SIGKDD International Conference on Knowledge Discovery and Data Mining*, Association For Computing Machinery, New York, NY, USA, **2016**, pp. 785-794.

[21] fernando, *BayesianOptimization: A Python Implementation of Global Optimization with Gaussian Processes*, Github, **n.d.**

[22] S. M. Lundberg, G. Erion, H. Chen, A. DeGrave, J. M. Prutkin, B. Nair, R. Katz, J. Himmelfarb, N. Bansal, S.-I. Lee, *Nat Mach Intell* **2020**, *2*, 56.

[23] C. Rice, R. J. Young, R. Zan, U. Bangert, D. Wolverson, T. Georgiou, R. Jalil, K. S. Novoselov, *Phys. Rev. B Condens. Matter Mater. Phys.* **2013**, *87*, DOI 10.1103/physrevb.87.081307.

[24] T. Sohier, E. Ponomarev, M. Gibertini, H. Berger, N. Marzari, N. Ubrig, A. F. Morpurgo, *Phys. Rev. X* **2019**, *9*, 031019.

[25] Z. Melnikova-Kominkova, K. Jurkova, V. Vales, K. Drogowska-Horná, O. Frank, M. Kalbac, *Phys. Chem. Chem. Phys.* **2019**, *21*, 25700.

[26] A. Michail, N. Delikoukos, J. Parthenios, C. Galiotis, K. Papagelis, *Appl. Phys. Lett.* **2016**, *108*, 173102.

[27] W. H. Chae, J. D. Cain, E. D. Hanson, A. A. Murthy, V. P. Dravid, *Appl. Phys. Lett.* **2017**, *111*, 143106.

[28] H. Li, Q. Zhang, C. C. R. Yap, B. K. Tay, T. H. T. Edwin, A. Olivier, D. Baillargeat, *Adv. Funct. Mater.* **2012**, *22*, 1385.

[29] H. Li, A. W. Contryman, X. Qian, S. M. Ardakani, Y. Gong, X. Wang, J. M. Weisse, C. H. Lee, J. Zhao, P. M. Ajayan, J. Li, H. C. Manoharan, X. Zheng, *Nat. Commun.* **2015**, *6*, 7381.

[30] S. Pak, J. Lee, Y.-W. Lee, A.-R. Jang, S. Ahn, K. Y. Ma, Y. Cho, J. Hong, S. Lee, H. Y. Jeong, H. Im, H. S. Shin, S. M. Morris, S. Cha, J. I. Sohn, J. M. Kim, *Nano Lett.* **2017**, *17*, 5634.

[31] J. Tang, Z. Wei, Q. Wang, Y. Wang, B. Han, X. Li, B. Huang, M. Liao, J. Liu, N. Li, Y. Zhao, C. Shen, Y. Guo, X. Bai, P. Gao, W. Yang, L. Chen, K. Wu, R. Yang, D. Shi, G. Zhang, *Small* **2020**, *16*, e2004276.

References

[1] J. Feng, X. Qian, C.-W. Huang, J. Li, *Nat. Photonics* **2012**, *6*, 866.

[2] A. V. Tyurnina, D. A. Bandurin, E. Khestanova, V. G. Kravets, M. Koperski, F. Guinea, A. N. Grigorenko, A. K. Geim, I. V. Grigorieva, *ACS Photonics* **2019**, *6*, 516.

[3] M. Amani, D.-H. Lien, D. Kiriya, J. Xiao, A. Azcatl, J. Noh, S. R. Madhvapathy, R. Addou, S. Kc, M. Dubey, K. Cho, R. M. Wallace, S.-C. Lee, J.-H. He, J. W. Ager, X. Zhang, E. Yablonovitch, A. Javey, *Science* **2015**, *350*, 1065.

[4] D.-H. Lien, S. Z. Uddin, M. Yeh, M. Amani, H. Kim, J. W. Ager 3rd, E. Yablonovitch, A. Javey, *Science* **2019**, *364*, 468.

[5] F. Withers, O. Del Pozo-Zamudio, A. Mishchenko, A. P. Rooney, A. Gholinia, K. Watanabe, T. Taniguchi, S. J. Haigh, A. K. Geim, A. I. Tartakovskii, K. S. Novoselov, *Nat. Mater.* **2015**, *14*, 301.

[6] O. Salehzadeh, M. Djavid, N. H. Tran, I. Shih, Z. Mi, *Nano Lett.* **2015**, *15*, 5302.

[7] J. G. Greener, S. M. Kandathil, L. Moffat, D. T. Jones, *Nat. Rev. Mol. Cell Biol.* **2022**, *23*, 40.

[8] A. Davies, P. Veličković, L. Buesing, S. Blackwell, D. Zheng, N. Tomašev, R. Tanburn, P. Battaglia, C. Blundell, A. Juhász, M. Lackenby, G. Williamson, D. Hassabis, P. Kohli, *Nature* **2021**, *600*, 70.

[9] K. T. Butler, D. W. Davies, H. Cartwright, O. Isayev, A. Walsh, *Nature* **2018**, *559*, 547.

Dr. Ang-Yu LU

PhD Student,
Department of Electrical Engineering and
Computer Science,
Massachusetts Institute of Technology

Deep Learning Processors Based on Si Photonic Circuits
シリコン光回路を用いた深層学習プロセッサ

TAKENAKA Mitsuru
竹中 充

We have conducted research on deep learning processors using programmable Si photonic integrated circuits. By integrating compound semiconductors and phase-change materials into Si photonic circuits, we have successfully achieved precise control and measurement of optical phase within the circuits, as well as highly sensitive optical intensity detection. This enables precise control of large-scale programmable photonic circuits with high speed and low power consumption. Additionally, by using the newly proposed photonic circuits, we have demonstrated the potential to accelerate learning through on-chip error back-propagation, in addition to inference, greatly contributing to the early realization of deep learning processors based on Si photonic circuits. Here, we present our recent research on deep learning processors based on Si photonic circuits.

我々は，プログラミング可能なシリコン光回路を用いた深層学習プロセッサに関する研究を進めてきた。化合物半導体や相変化材料をシリコン光回路の集積することで，回路中の光位相の精密な制御・計測や高感度な光強度検出に成功した。これにより大規模なプログラマブル光回路を高速・低消費電力で精密に制御することを可能とした。更に，新しく提唱した光回路を用いて，推論に加えて，オンチップ上での誤差逆伝播による学習加速も可能であることを明らかにするなど，シリコン光回路を用いた深層学習プロセッサの早期実現に大きく資する研究成果を挙げた。ここでは，我々のシリコン光回路を用いた深層学習プロセッサに関する最近の取り組みについて述べる。

Introduction

Over the past 50 years, the miniaturization of transistors has progressed to the point of reaching 3 nm, and research and development for further miniaturization is ongoing worldwide[1]. However, as semiconductor miniaturization becomes even more challenging, it is believed that improving computing performance through optoelectronic fusion will be necessary for the beyond 2 nm generation. In particular, the development of artificial intelligence (AI), represented by ChatGPT, has been remarkable, and new computing technologies that go beyond conventional principles are truly sought after. Against this background, optical operations using large-scale Si photonic circuits has attracted much attention[2-3]. By using programmable Si photonic circuits[4], arithmetic operations such as multiply-accumulate (MAC) operation can be performed using light, and it is expected that the performance of deep learning will be significantly improved. Active research is being conducted worldwide for this purpose. However, various challenges remain to achieve large-scale programmable photonic circuits, as shown in Figure 1. In order to program photonic circuits, precise control of the phase of optical signals in the circuit is required. However, the currently mainstream optical phase shifter that uses heater heating consumes a large amount of power and is not suitable for large-scale integration[5]. In addition, in order to precisely control parameters such as optical phase, it is necessary to integrate numerous optical power monitors for measuring circuit operations, but there are challenges in sensitivity and optical insertion loss. High-speed and low-power operation is required for photodetectors that read out optical operations as electrical signals, but sensitivity and parasitic capacitance are also challenges.
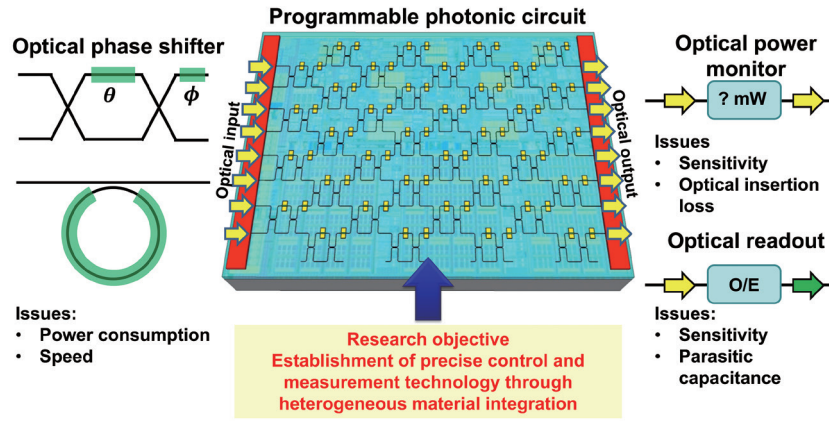
Figure 1 Tehcnology issues in programmable photonic circuits.

To overcome these technological challenges, we have conducted research to establish precise control and measurement techniques for photonic circuits by integrating compound semiconductors and phase-change materials heterogeneously into Si photonic circuits. Additionally, we have developed unique programmable photonic circuits capable of performing both learning and inference functions in the optical domain. In this paper, we present our recent research, which advances the early realization of deep learning processors through optoelectronic fusion.

Optical phase shifters

An optical phase shifter is a device that can manipulate the phase of an optical signal as it passes through a photonic circuit. Since the programming of a photonic circuit relies on optical phase tuning, it is essential to integrate numerous optical phase shifters into the photonic circuit. To control optical phase, a thermo-optic phase shifter, as depicted in Figure 2(a), is widely employed in Si photonic circuits due to its simple fabrication procedure and low optical insertion loss[6]. When heating a Si waveguide by current injection, the refractive index of Si increases due to the thermo-optic effect, resulting in an optical phase shift. However, it requires approximately 10 – 20 mW of heating power to achieve a π phase shift, which hinders large-scale integration. Moreover, thermal crosstalk between neighboring thermo-optic phase shifters makes precise control of optical phase difficult. As a substitute for power-hungry thermo-optic phase shifters, various device candidates are being intensely investigated around the world[7-10].

As an energy-efficient optical phase shifter, we have investigated a metal-oxide-semiconductor (MOS) capacitor-based device using heterogenous integration of III-V semiconductor on Si, as depicted in Figure 2(b)[11]. Using direct wafer bonding technology, a thin n-type InGaAsP is bonded onto a p-type Si rib waveguide with an Al_2O_3 bonding interface[12]. We employed an Al_2O_3 layer deposited through atomic layer deposition (ALD) to passivate the InGaAsP surface, which is essential for the MOS-based optical phase shifter. The ALD Al_2O_3 layer also facilitates a hydrophilic surface, enabling wafer bonding without the need for a plasma surface activation process. When a gate voltage (Vg) is applied between the InGaAsP membrane and Si waveguide, electrons and holes accumulate at the InGaAsP and Si MOS interfaces, respectively. The electron-induced refractive index change in InGaAsP is more than ten times greater than in Si Moreover, the hole-induced absorption in InGaAsP, which is significantly greater than in Si, can be completely removed since hole accumulates only on the Si side. As a result, efficient, low-loss optical phase modulation is achieved using the InGaAsP/Si hybrid MOS capacitor. The energy consumption required to sustain a π phase shift, predominantly influenced by gate leakage current through a MOS capacitor, is less than 1 nW[13]. This value is more than one million times smaller than that of a thermo-optic phase shifter. Therefore, we anticipate a significant reduction in the power consumption of a programmable PIC through the utilization of III-V/Si hybrid MOS optical phase shifters.
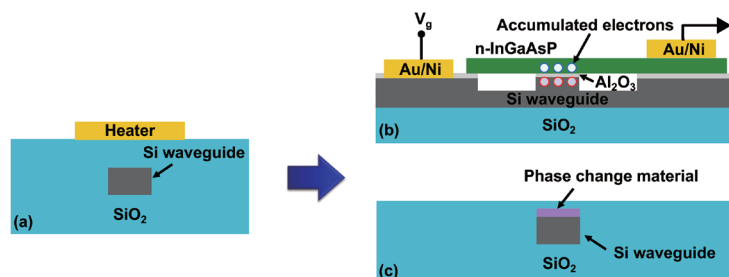

Figure 2 (a) Optical phase shifter based on thermo-optic effect. (b) Optical phase shifter based on heterogeneous integration of III-V compound semiconductor and Si. (c) Optical phase shifter using phase change material.

Non-volatile optical phase shift is also crucial to achieve in-memory computing, which can help overcome the von Neumann bottleneck. In addition to ferroelectric materials, phase change materials are promising candidates for achieving non-volatile optical phase shift[14]. A significant contrast in optical constants exists between the amorphous and crystalline states of a phase-change material. By depositing a phase change material on a Si waveguide as shown in Figure 2(c), this large contrast in optical constants can be used for optical modulation. $Ge_2Sb_2Te_5$ (GST), widely employed in rewritable optical disks, was initially introduced into a Si waveguide for non-volatile optical intensity modulation at near-infrared wavelengths. However, optical phase modulation is not achievable due to the significant absorption in GST. To address this issue, we have proposed to use GST in mid-infrared (MIR) wavelengths[15]. We experimentally demonstrated the band-edge absorption of GST can be reduced using a longer operating wavelength and achieved 2.6 dB loss for a p phase shifter at a 2.32 μm wavelength. To further reduce optical loss, we have developed $Ge_2Sb_2Te_3S_2$ (GSTS), where the bandgap energy of GSTS is increased through sulfur doping into GST[16]. Using GSTS, we achieved 0.29 dB of π phase shift at a 2.34 μm wavelength, which is one of the lowest values among phase change material-based optical phase shifters. We applied the GSTS optical phase shifter to a ring resonator and successfully tuned the resonance wavelength of the resonator without significant degradation in its Q-factor. Owing to the non-volatility in the phase change material-based optical phase shifter, the standby power consumption can be zero after tuning optical phase, enabling the large-scale integration of optical phase shifters into a programmable photonic circuit.

Optical power monitor and photodetector

The monitoring of optical power in a Si waveguide is crucial for a programmable photonic circuit. Since initial phase errors are unavoidable due to fabrication variations in Si waveguides, the initial state of a programmable photonic circuit must be calibrated in some way. Monitoring optical outputs by tuning optical phase shifters on a chip is the most common method for indirectly estimating the circuit state. However, this method is applicable only to specific circuits. A more direct method of measuring the circuit state is to embed numerous optical power monitors directly into a photonic circuit. A Ge photodetector can be easily integrated with a Si photonic circuit; however, tapping waveguides are additionally required for power monitoring, which increases optical loss and complicates the circuit further. Reading a small change in the conductance of a Si waveguide due to the increase in free carriers resulting from optical absorption is another potential method for power monitoring. This method enables low insertion loss; however, its low sensitivity necessitates a phase-sensitive detection circuit, which complicates the overall circuit design.

To address the challenges in power monitoring, we have proposed a waveguide-coupled phototransistor, as shown in Figure 3(a)[17]. A thin InGaAs membrane is bonded onto a Si waveguide to serve as an absorber. When the light signal propagates through the Si waveguide, the evanescent light is absorbed in the InGaAs layer. The absorbed light generates photocarriers in the InGaAs layer, which are detected as a photocurrent between the source and drain terminals. Unlike conventional photodetectors, we propose utilizing the Si waveguide as a gate
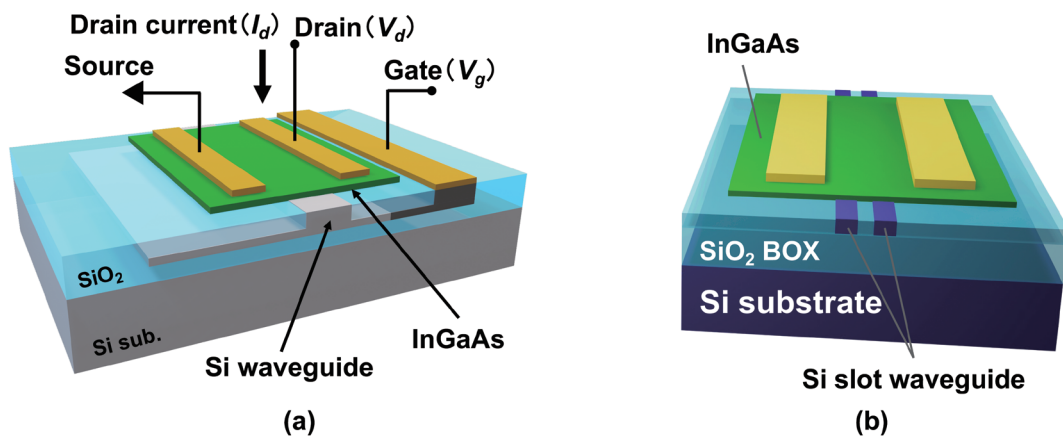

Figure 3 (a) Waveguide-coupled phototransistor for optical power monitoring.
(b) Waveguide-coupled photodetector with InGaAs membrane on Si slot waveguide.

electrode by applying a gate voltage. Here, we employ an Al_2O_3 bonding interface between the InGaAs and Si layers to achieve superior surface passivation, enabling electron accumulation at the InGaAs MOS interface. By applying a positive gate voltage to the InGaAs layer through the Si gate electrode, the InGaAs layer functions as a transistor channel, controlling the drain current flowing between the source and drain terminals. Through transistor operation, the photocurrent is amplified, leading to a significant increase in responsivity. Previously reported waveguide phototransistors have utilized metal gate electrodes, which are positioned far from the channel to minimize optical loss caused by the electrodes. Consequently, gate controllability is compromised. By employing a Si waveguide as a gate electrode, we can position the Si gate electrode underneath the InGaAs channel, enabling effective gating without a significant increase in optical loss. Leveraging these advantages in our proposal, we have achieved approximately 10^6 A/W responsivity, which represents the highest value among waveguide-coupled phototransistors. We found that the switching speed ranges from 1 μs to 100 μs, which is sufficient for power monitor applications. Thanks to its high responsivity, we can reduce the device length to minimize optical insertion loss. Hence, we can achieve a high-responsivity, transparent optical power monitor without the need for additional complicated electrical circuits.

To further reduce the optical insertion loss of the presented phototransistor, we proposed employing an InP membrane instead of an InGaAs membrane[18]. Since the bandgap energy of InP is greater than the photon energy of interest, InP is essentially transparent for light at a 1.55 μm wavelength. Consequently, photodetection using InP is not feasible. However, we have observed substantial photocurrent in the InP/Si waveguide-coupled phototransistor. We expect that a small optical absorption in InP related to the crystal defects in InP is amplified through the phototransistor operation. As a result, the responsivity of greater than 1 A/W is experimentally demonstrated even using InP. Since the strong band-edge absorption is not used, we achieved an optical insertion loss of less than 0.25 dB. Since we do not rely on strong band-edge absorption, we have achieved an optical insertion loss of less than 0.25 dB. Additionally, we have monolithically integrated the waveguide-coupled phototransistor and MOS-based optical phase shifter by bonding the same InP membrane onto the Si waveguides. The output from a Mach-Zehnder interferometer controlled with the MOS-based optical phase shifter is monitored by the InP/Si phototransistor, exhibiting the feasibility of power monitoring a programmable photonic circuit.

High-speed and low-power photodetectors are also crucial for reading the results of optical operations performed by a programmable photonic circuit. If low-power MOS or phase change material-based optical phase shifters are utilized, the power required for the optical operation itself becomes negligibly small. Consequently, the power consumption of a programmable photonic circuit for deep learning is primarily dominated by optical input and output interfaces. Therefore, the low power consumption of the optical receiver system is crucial for reducing the operating power of deep learning. A conventional optical receiver system necessitates a transimpedance amplifier to convert photocurrent into a voltage signal, resulting in significant electricity consumption. To resolve this issue, the receiver-less system was proposed, in which a transimpedance amplifier is replaced by a load resistor[19]. However, to obtain sufficient voltage across the load resistor, its resistance must be greater than 1 kΩ. In this scenario, the operation speed is greatly limited by the RC constant of the receiver system. To achieve an operation speed greater than 10 GHz, the capacitance of a photodetector must be reduced to approximately 1 fF. However, achieving such a small capacitance is challenging without compromising responsivity, as there is a trade-off relationship between responsivity and capacitance in a photodetector. To overcome this trade-off relationship, we have proposed a III-V/Si hybrid photodetector, wherein a thin InGaAs absorber is bonded onto a Si slot waveguide, as illustrated in **Figure 3** (b)[20]. A Si slot waveguide enables the confinement of propagating light into a narrow gap between two Si rails. Consequently, optical absorption in the InGaAs is enhanced, allowing us to reduce the device length to lower the capacitance without sacrificing responsivity. We experimentally demonstrated a low capacitance of 1.9 fF and a high responsivity of 1.0 A/W at a wavelength of 1.55 μm wavelength simultaneously. The capacitance is expected to be further reduced to less than 1 fF by eliminating the parasitic capacitance of the electrodes. Hence, the presented photodetector contributes to the realization of a receiver-less system for a low-power readout of a programmable photonic circuit.

Photonic crossbar array

A programmable photonic circuit based on nested Mach-Zehnder interferometers arranged in a triangle or rectangular mesh is the most common circuit topology for deep learning applications because of its universality in optical operations. However, the size of a single Mach-Zehnder interferometer is large, which makes it unsuitable for large-scale integration. To overcome this issue, we have proposed photonic crossbar array based on ring resonators, as depicted in Figure 4[21]. Add-drop ring resonators, which can selectively drop a specific wavelength signal into a drop waveguide, are arranged in a lattice fashion. As indicated in Figure 3(a), each ring resonator is tuned so that drop wavelengths do not overlap either in row and column. For the inference operation, a multiple-wavelength optical signal serving as an input vector is injected from the left-hand side of the crossbar. Subsequently, each wavelength signal is dropped at its respective ring resonator. Through optical phase shifters integrated with ring resonators, the amount of the dropped signal can be tuned, akin to the weight of a matrix for multiplication. Consequently, the multiplication between each input vector element and matrix weight can be executed. Finally, the dropped multiple-wavelength signal are simultaneously converted into electrical signal, which

corresponds to the add operation. As a result, we can perform multiply-accumulation operation in optoelectronic fashion with the photonic crossbar array. One of the unique features of the proposed crossbar array is that it can be also used for accelerating learning[22]. As shown in Figure 4(b), when a multiple-wavelength optical signal serving as an error vector is injected from the top side of the crossbar, multiply-accumulation operation between the error vector and transposed matrix used for inference can be obtained from the right-hand side of the circuit. This multiply-accumulate operation is utilized in backpropagation for the learning of neural networks. Hence, the photonic crossbar array enables on-chip backpropagation in the optical domain. To show the feasibility of our proposal, we fabricated the photonic crossbar array using Si photonics platform as shown in Figure 4(c). We have successfully demonstrated inference and learning operations using this photonic crossbar array chip. In this demonstration, we utilized thermo-optic phase shifters to tune the ring resonators on the crossbar array. To reduce the power consumption of the phase shifters and mitigate thermal crosstalk between the ring resonators, we are now aiming for the integration of MOS-based or phase change material-based optical phase shifters with the crossbar array.
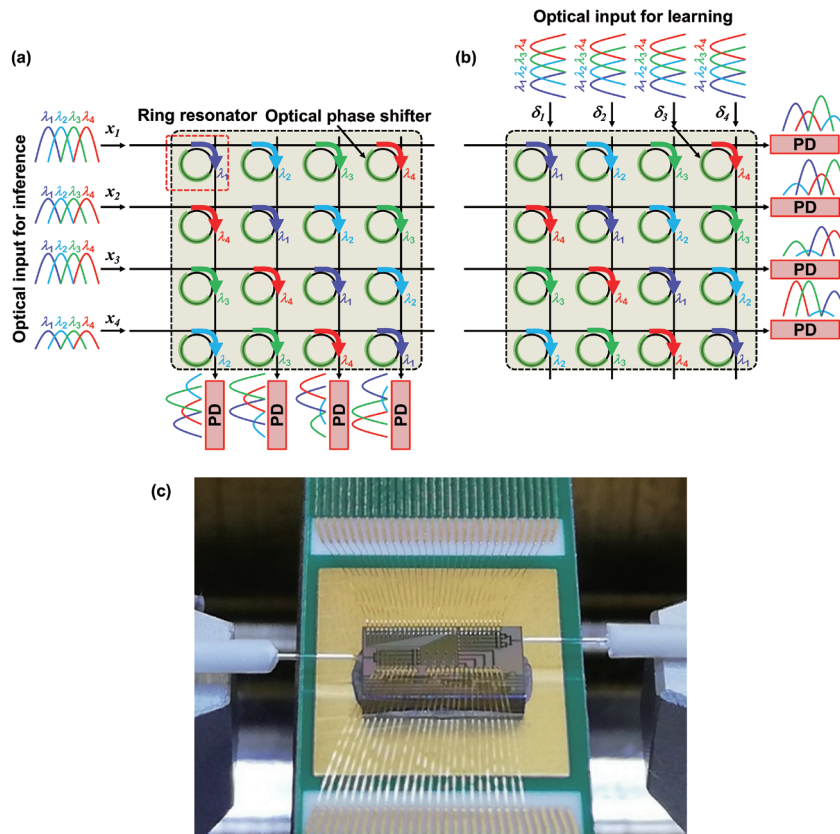

Figure 4   Photonic crossbar array based on ring resonators.
(a)Inference operation. (b) Learning operation with on-chip backpropagation. (c)Photograph of photonic crossbar array chip fabricated by Si photonics platform.

Conclusion

In this paper, we have explored the possibilities of a programmable photonic circuit based on Si photonics in advancing computing technologies, particularly in the domain of deep learning processors. As Moore's law begins to slow down, the fusion of electronics and photonics becomes increasingly crucial for overcoming the limitations posed by conventional computing architectures. Our research, which is based on innovative materials integration and new circuit architectures such as a photonic crossbar array, will contribute to the realization of large-scale programmable photonic circuits. With ongoing research and development efforts, we anticipate the creation of deep learning processors that harness the power of light to redefine the boundaries of computational efficiency and intelligence.

References

[1] W. Cao *et al*., "The future transistors," *Nature*, vol. 620, no. 7974, pp. 501–515, Aug. 2023.

[2] Y. Shen *et al*., "Deep learning with coherent nanophotonic circuits," *Nat. Photonics*, vol. 11, no. 7, pp. 441–446, Jun. 2017.

[3] B. J. Shastri *et al*., "Photonics for artificial intelligence and neuromorphic computing," *Nat. Photonics*, vol. 15, no. 2, pp. 102–114, Jan. 2021.

[4] W. Bogaerts *et al*., "Programmable photonic circuits," *Nature*, vol. 586, no. 7828, pp. 207–216, Oct. 2020.

[5] M. Takenaka *et al*., "III–V/Si Hybrid MOS Optical Phase Shifter for Si Photonic Integrated Circuits," *J. Lightwave Technol.*, vol. 37, no. 5, pp. 1474–1483, Mar. 2019.

[6] S. Liu *et al*., "Thermo-optic phase shifters based on silicon-on-insulator platform: state-of-the-art and a review," *Frontiers of Optoelectronics*, vol. 15, no. 1, p. 9, Apr. 2022.

[7] M. Dong *et al*., "High-speed programmable photonic circuits in a cryogenically compatible, visible–near-infrared 200 mm CMOS architecture," *Nat. Photonics*, vol. 16, no. 1, pp. 59–65, Dec. 2021.

[8] J. Geler-Kremer *et al*., "A ferroelectric multilevel non-volatile photonic phase shifter," *Nat. Photonics*, vol. 16, no. 7, pp. 491–497, May 2022.

[9] D. U. Kim *et al*., "Programmable photonic arrays based on microelectromechanical elements with femtowatt-level standby power consumption," *Nat. Photonics*, pp. 1–8, Nov. 2023.

[10] R. Tang *et al*., "Non volatile hybrid optical phase shifter driven by a ferroelectric transistor," *Laser Photon. Rev.*, vol. 17, no. 11, Nov. 2023.

[11] J.-H. Han, F. Boeuf, J. Fujikata, S. Takahashi, S. Takagi, and M. Takenaka, "Efficient low-loss InGaAsP/Si hybrid MOS optical modulator," *Nat. Photonics*, vol. 11, no. 8, pp. 486–490, Jul. 2017.

[12] J.-H. Han, M. Takenaka, and S. Takagi, "Study on void reduction in direct wafer bonding using Al_2O_3/HfO_2 bonding interface for high-performance Si high-k MOS optical modulators," *Jpn. J. Appl. Phys.*, vol. 55, no. 4S, 04EC06, Mar. 2016.

[13] Q. Li, J.-H. Han, C. P. Ho, S. Takagi, and M. Takenaka, "Ultra-power-efficient 2×2 Si Mach-Zehnder interferometer optical switch based on III-V/Si hybrid MOS phase shifter," *Opt. Express*, vol. 26, no. 26, p. 35003, Dec. 2018.

[14] C. Ríos *et al*., "Integrated all-photonic non-volatile multi-level memory," *Nat. Photonics*, vol. 9, no. September, pp. 725–732, 2015.

[15] Y. Miyatake *et al*., "Non-volatile Compact Optical Phase Shifter based on $Ge_2Sb_2Te_5$ operating at 2.3 μm," Opt. Mater. Express, vol. 12, no. 12, pp. 4582–4593, Oct. 2022.

[16] Y. Miyatake *et al*., "Proposal of low-loss non-volatile mid-infrared optical phase shifter based on $Ge_2Sb_2Te_3S_2$," *IEEE Trans. Electron Devices*, vol. 70, no. 4, pp. 2106–2112, Apr. 2023.

[17] T. Ochiai *et al*., "Ultrahigh-responsivity waveguide-coupled optical power monitor for Si photonic circuits operating at near-infrared wavelengths," *Nat. Commun.*, vol. 13, no. 1, p. 7443, Dec. 2022.

[18] T. Akazawa, K. Sumita, S. Monfray, F. Boeuf, K. Toprasertpong, S. Takagi, M. Takenaka, "Transparent in-line optical power monitor integrated with MOS optical phase shifter using InP/Si hybrid integration," *European Conference on Optical Communication (ECOC2023)*, We.D.4.5, Glasgow, UK, 1–5 October 2023.

[19] C. Debaes et al., "Receiver-less optical clock injection for clock distribution networks," *IEEE J. Sel. Top. Quantum Electron.*, vol. 9, no. 2, pp. 400–409, Mar. 2003.

[20] T. Akazawa *et al*., "Low-Capacitance Ultrathin InGaAs Membrane Photodetector on Si Slot Waveguide Toward Receiverless System," *IEEE Trans. Electron Devices*, vol. 69, no. 12, pp. 7184–7189, Dec. 2022.

[21] S. Ohno, K. Toprasertpong, S. Takagi, and M. Takenaka, "Si microring resonator crossbar arrays for deep learning accelerator," *Jpn. J. Appl. Phys.*, vol. 59, no. SG, GGE04, Feb. 2020.

[22] S. Ohno, R. Tang, K. Toprasertpong, S. Takagi, and M. Takenaka, "Si Microring Resonator Crossbar Array for On-Chip Inference and Training of the Optical Neural Network," *ACS Photonics*, vol. 9, no. 8, pp. 2614–2622, Aug. 2022.

Dr. TAKENAKA Mitsuru

竹中 充

Professor,
School of Engineering,
Department of Electrical Engineering
and Information Systems,
The University of Tokyo

Development of a Compact Deep-Ultraviolet Laser Source for Precision Microstructure Measurement

微細構造計測に向けた小型深紫外レーザー光源の開発

KUSHIMOTO Maki

久志本 真希

This article presents advancements in deep-ultraviolet (DUV) laser diodes (LDs) based on nitride semiconductors, particularly focusing on achieving room-temperature continuous-wave lasing. DUV LDs emitting in the UV-C wavelength range (<280 nm) hold promise for various applications, including disinfection, medical diagnostics, and industrial processes. Key breakthroughs in AlGaN-based DUV LDs are discussed, including crystal quality improvement through pseudo-morphic AlGaN growth on single-crystal AlN substrates and electrical conductivity control using distributed polarization doping. The process of suppressing process-induced crystal defects and achieving room-temperature continuous-wave lasing will also be discussed. This achievement is a successful realization of a room-temperature continuous-wave oscillation laser, which expands the possibilities of DUV LDs in various technological fields.

本稿では，窒化物半導体をベースとした深紫外（DUV）レーザーダイオード（LD）の進展について，特に室温連続発振の実現に焦点を当てて紹介する。UV-C波長領域（<280 nm）で発光するDUV LDは，殺菌，医療診断，工業プロセスなど，さまざまな用途への応用が期待されている。AlGaNベースのDUV LDにおける主要なブレークスルーとして，AlN単結晶基板上の擬似格子整合AlGaN成長による結晶品質の改善や，分布分極ドーピングを用いた電気伝導度の制御などが議論されている。さらに，プロセスに起因する結晶欠陥を抑制し，室温連続波発振を達成した経緯についても解説する。本成果は室温での連続波発振レーザーの実現に成功したものであり，多様な技術領域におけるDUV LDの可能性が広げるものである。

Introduction

Our research group is studying the deep-ultraviolet (DUV) laser diodes (LDs) based on nitride semiconductors. The DUV laser sources in the wavelength range of 280 nm or less, called UV-C, are attracting attention because of their high absorption property by biomolecules such as DNA. They can be applied to disinfection and in medical fields. UV-C-emitting lasers can also be used in a wide range of industrial applications, such as the detection of minute particles, high-accuracy distance measurement, and semiconductor exposure apparatuses. In addition, if the laser output is improved to watt levels, UV-C-emitting lasers may be used for laser machining apparatuses capable of printing and machining without causing thermal damage because of their high absorbance by materials. Our research group has been at the forefront of DUV LD

technology; room-temperature pulsed oscillation with a wavelength of 271.8 nm was demonstrated in 2019[1] and room-temperature continuous-wave lasing was achieved in 2022[2]. In this article, we explain the key technologies employed to realize the room-temperature continuous-wave lasing of DUV LDs and present the characteristics of the lasers used in the demonstration.

Breakthroughs in DUV LDs

The LDs in the UV range have been studied using AlGaN-based nitride semiconductors after the oscillation of InGaN-based blue-violet LDs was achieved. AlGaN is a direct transition semiconductor with high luminous efficiency. Light emission in a wide wavelength range, including UV-C, can be obtained by controlling the mixed ratio of the crystals. Control of refractive index is also

possible. In addition, AlGaN is suitable for Fabry–Perot LDs because a resonator end face that is smooth at the atomic level can be formed by cleaving crystals. However, after the report of laser oscillation with a wavelength of 336 nm in the UV-A range in 2008[3], there had been no report about the lasing of LDs with a shorter wavelength. The major issues preventing such an achievement were the quality of AlGaN crystals and inadequate control of the electrical conductivity.

Figure 1(a) shows the DUV-LD structure we proposed to solve the above issues. First, we worked on the fabrication of LDs by the pseudo-lattice matching of AlGaN grown on a single-crystal AlN substrate with the aim of improving the crystal quality. The dislocation density of the single-crystal AlN substrate is less than 10^4/cm^2. The dislocation density of pseudo-morphic AlGaN grown on this substrate was equal to that of the substrate, which meant a high-quality laser structure. The results of the characteristic evaluation by optical excitation showed that the threshold excitation power density was significantly reduced in the laser structure fabricated on the single-crystal AlN substrate compared with the laser structure fabricated on a dissimilar substrate.

The main point of the issue of electrical conductivity control was whether a sufficient hole density can be achieved in the p-cladding layer. A sufficient hole density was not achieved by conventional electrical conductivity control using doping owing to the limitation of the material properties. To solve this issue, we applied distributed polarization doping (DPD)[4] to the p-cladding layer. This technique used the polarization generated in AlN and GaN crystals and AlGaN crystals as a result of distortion from a regular tetrahedral structure, as shown in Figure 1(b). The amount of polarization differs among AlGaN crystals with different AlN molar fraction. The higher the AlN molar fraction, the greater the polarization. This means that there is a polarization difference on the interface between the AlGaN crystals with different AlN molar fractions. As a result, an amount of free carriers corresponding to the difference in the amount of polarization accumulates on the interface so that the charge neutral condition is satisfied. As shown in Figure 1(c), the polarization charge is dispersed in the thickness direction when the amount of polarization is distributed in the thickness direction (the direction toward [0001]) by continuously varying the AlN molar fraction of AlGaN crystals. Because the accumulation of free carriers is also dispersed in the thickness direction corresponding to the dispersion of polarization charge, a state where free carriers exist across the entire film is produced effectively (Figure 1(c) shows the accumulation of holes). We became the first in the world to demonstrate the room-temperature pulsed oscillation of the DUV LD through the development of technologies and the design of laser structures based on the above concepts[1].
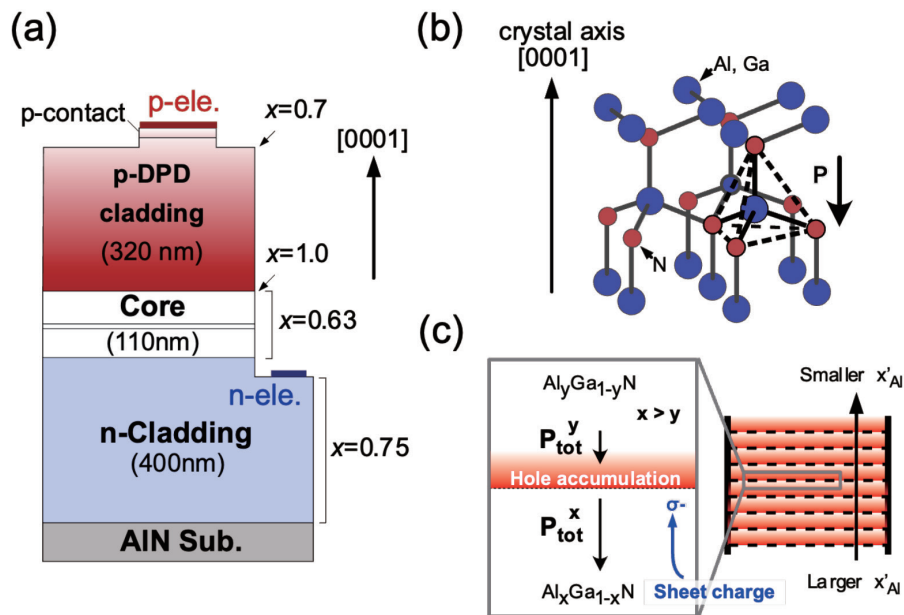

Figure 1   (a) Schematic of DUV LD. (b) Polarization in wurtzite structure. (c) Diagram of DPD.

Barrier to continuous-wave lasing : process-induced formation of crystal defects

Although we demonstrated the pulsed lasing of the DUV LD, we could not achieve the continuous-wave lasing because of the high driving power of the DUV LD. The major cause was the process-induced formation of crystal defects. While the generation of new dislocations was suppressed in the thin AlGaN film grown pseudomorphically, strain remained in the thin film. The DUV LD was fabricated by the AlGaN with a large lattice constant on a single-crystal AlN substrate with a small lattice constant. Therefore, new crystal defects were not formed at the time of film growth. However, the strain in AlGaN was relaxed by the heat treatment during the DUV LD fabrication process, resulting in the formation of crystal defects. The upper panel of Figure 2(a) shows the plan-view TEM image of the mesa stripe formed perpendicular to the wafer plane. Numerous dislocation lines were observed in the range of ~12 µm from near the mesa edge to the center of the mesa stripe. Some of the defects passed through the emission layer, which significantly deteriorated the emission properties. The threshold current of the LD with its p-electrode placed in an area containing the dislocation was higher than that of the LD with its p-electrode placed in an area without the dislocation[5]. DUV LDs must have a horizontal conductive device structure with the electrodes placed on the surface side because no fabrication technology for a conductive single-crystal AlN substrate has been established. The current pathway from the p-electrode to the n-electrode is extended if the electrode arrangement is constrained by the presence of crystal defects, which results in increased device resistance. As explained above, the LDs that we developed to demonstrate the pulsed lasing had the problem of a trade-off between threshold current density and driving voltage because of the crystal defects.

Improvement of device properties by suppressing crystal defect

With the aim of suppressing the formation of crystal defects, we controlled the distribution of the residual-strain-induced stress in the mesa stripe[6]. Figure 2(b) shows the results of the simulation of stress distribution by the finite element method and the maximum shear stress concentrating at the bottom edge of the mesa at each slope angle of the edge of the mesa stripe. The restrain of the mesa edge was released when the mesa stripe was formed by etching. At that time, the shear stress induced by the residual strain in the AlGaN thin film concentrated at the bottom edge of the mesa in the n-cladding layer. The results of the simulation showed that the maximum shear stress reached 9 GPa in the vertically etched mesa stripe. On the other hand, the shear stress was dispersed when the slope angle of the mesa stripe was small, indicating that the stress concentration at the bottom edge of the mesa can be reduced.

Considering the above finding, we fabricated a mesa structure with a slope angle of 15°. Although the stress concentration can be reduced as the slope angle decreases, the disadvantage of the small slope angle is the increased distance between electrodes. The lower panel of Figure 2(a) shows the plan-view TEM image of the LD subjected to heat treatment after the formation of the sloped mesa. The crystal defects observed in the vertical mesa structure were not observed in the sloped mesa structure. These results indicated that the process-induced crystal defects was suppressed by controlling the stress distribution by means of the sloped mesa.

(a) Plan-view

Conv. side wall Slope=90°

1µm

New side wall Slope=15°

⊙→[11$\bar{2}$0]
[1$\bar{1}$00]

1µm

Mesa edge

(b) Cross-sectional view

Maximum shear stress (GPa) / Slope (degrees)

Conv. Slope=90°

p-cladding
Waveguide
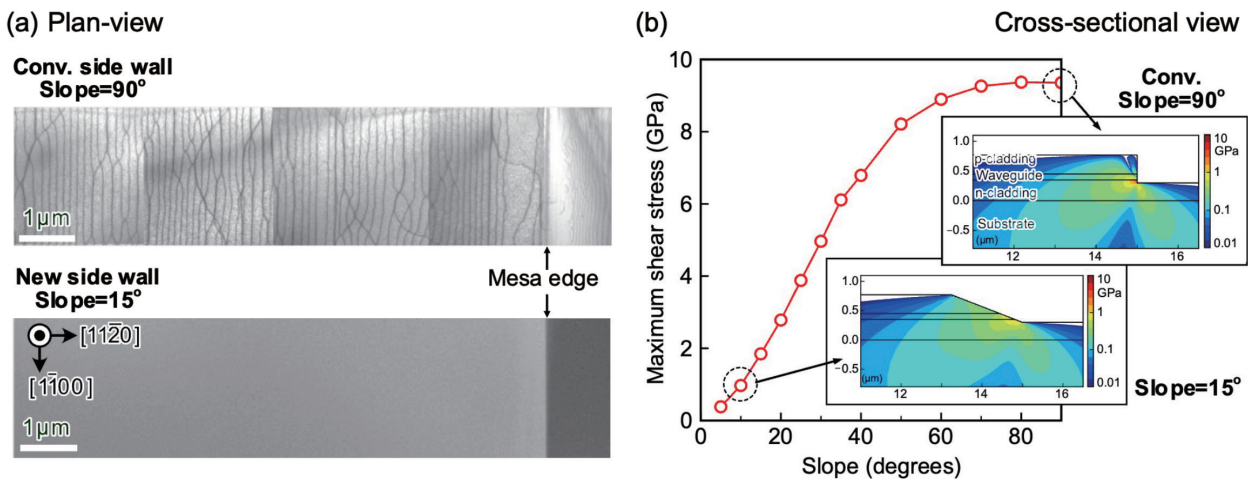n-cladding
Substrate

Slope=15°

Figure 2 (a) Difference in slope angle of mesa stripes. (a) Plan-view TEM images at the edge of mesa stripe.
(b) Schematics of UV-C LD and conceptual images of residual-film-stress-induced basal plane slip.

Characteristics of DUV LDs

From the results of the calculation in which the characteristic temperature of threshold current and the thermal resistance of the package were taken into account, it was estimated that the driving power should be reduced to 1 W or lower to achieve room-temperature continuous-wave lasing[2]. To reduce the threshold current density, the distance between p- and n-electrodes, d, in the conventional vertical mesa structure should be 20 μm. The resistance of the n-cladding layer was proportional to d and accounted for at least half of the device resistance of the LD with a cavity length of 600 μm. On the other hand, d was reduced to 5 μm in the sloped mesa structure in which the formation of crystal defects was suppressed. As a result, the resistance in LD with the sloped mesa structure was significantly reduced. Also, the n-electrodes were placed on both sides of the mesa stripe in order to reduce the resistance compared with the LD with the n-electrode placed on one side. We significantly reduced the device resistance from the initial value of 16 Ω to 8.3 Ω by adopting those resistance reduction methods in the device design. Finally, we achieved the lasing of DUV LD under DC at room temperature. **Figure 3** shows the $L–I–V$ characteristics of DUV LDs. The room-temperature continuous-wave lasing of the LD with a sloped mesa structure was observed with threshold current I_{th} = 125 mA, threshold voltage V_{th} = 8.7 V, and lasing wavelength of 274 nm. The input power at that time was 1.1 W, which is close to 1 W, the target value mentioned at the beginning of this section.
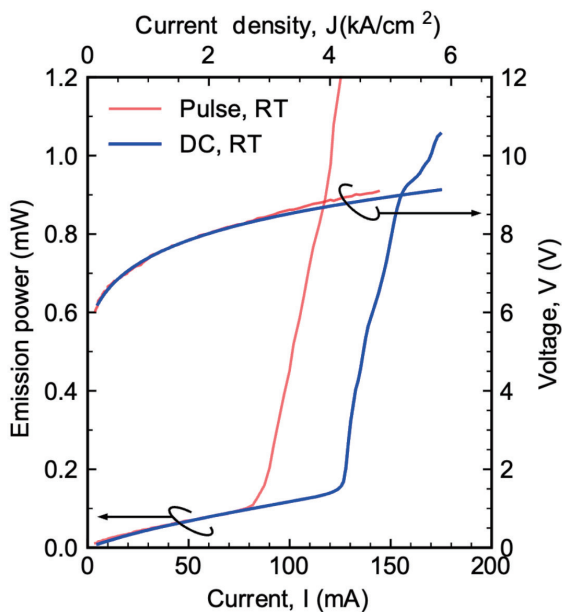
Conclusion

In this article, we explained two key technologies in realizing AlGaN-based DUV LDs. The improvement of crystal quality by means of pseudo-morphic growth of AlGaN on a single-crystal AlN substrate and electrical conductivity control in the p-cladding layer of high-Al-composition AlGaN using DPD significantly contributed to the realization of the long-desired DUV LDs. Then, we described the process-induced crystal defects, which had prevented the room-temperature continuous-wave lasing of DUV LDs. The crystal defects were induced by the shear stress distribution after LD fabrication, which was caused by residual stress in the thin film. The formation of crystal defects was suppressed by controlling the stress distribution using a sloped mesa structure. The control of residual stress in the pseudo-morphic grown film is an important issue not only in LDs but also in the design of device structures. We were able to reduce the device resistance and realize the continuous-wave lasing of DUV LDs by adopting the measures described above. DUV LDs are brand-new laser sources that can be implemented in a variety of applications. Further improvement of the LD characteristics and increasing the output by using a combination of LDs are expected.

Figure 3 $L–I–V$ characteristics of DUV LDs under DC and pulsed current drive.

References

[1] Z. Zhang, M. Kushimoto, T. Sakai, N. Sugiyama, Leo J. Schowalter, C. Sasaoka, and H. Amano, *Appl. Phys. Express* 12 (2019) 124003.

[2] Z. Zhang, M. Kushimoto, A. Yoshikawa, K. Aoto, C. Sasaoka, Leo J. Schowalter, and H. Amano, *Appl. Phys. Lett*. 121 (2022) 222103.

[3] H. Yoshida, Y. Yamashita, M. Kuwabara, and H. Kan, *Appl. Phys. Lett*. 93 (2008) 241106.

[4] D. Jena, S. Heikman, D. Green, D. Buttari, R. Coffie, H. Xing, S. Keller, S. DenBaars, J. S. Speck, U. K. Mishra, and I. Smorchkova, *App. Phys. Lett*. 81 (2002) 4395.

[5] M. Kushimoto, Z. Zhang, N. Sugiyama, Y. Honda, L. J. Schowalter, C. Sasaoka, and H. Amano, *Appl. Phys. Express* 14 (2021) 051003.

[6] M. Kushimoto, Z. Zhang, A. Yoshikawa, K. Aoto, C. Sasaoka, Leo J. Schowalter, and H. Amano, *Appl. Phys. Lett*. 121 (2022) 222101.

Dr. KUSHIMOTO Maki

久志本 真希

Associate Professor/ Lecturer,
Graduate School of Engineering,
Nagoya University

Optical Smart Sensing

光学スマートセンシング

Introduction

Ramdane BENFERHAT

During the last 70 years, HORIBA has developed a large portfolio of optical technologies to meet the specific needs of the automotive industry, the environment, medical and material research. From Xray to Infrared, these technologies are widely used all over the world by leading end-users and organizations. Today, emerging applications, driven by the demand for faster data communication along with powerful artificial intelligence (AI) capabilities, high-performance and low-cost power conversion products for longer battery life, faster phones charging and electric vehicles (EVs) batteries, are creating new demand to the semiconductor industry.

Previously, these demands have been met through the continuous miniaturization of silicon-based complementary metal–oxide–semiconductor (CMOS) integrated circuits and by the development of a new generation of compound semiconductors. While for integrated circuits the technology enters the sub-2 nm node, with a lateral size of silicon transistors rapidly approaching its physical limits, leading to increased leakage current and degradation of mobility, the power and high frequency devices require a technology which is able to reduce the size of the devices, produced in large volume in existing fab.

These limitations of conventional silicon-based devices led to the exploration of new materials, such as 2D materials for the expansion below 2nm node and wide band gap compound semiconductors for the production of low-cost power and high frequency devices. For many field experts, the semiconductor industry is changing era from node era to the "Material Era".

Adopting new materials in the semiconductor industry is a disruptive process. Thus, achieving desired yields and equivalent product quality requires smart manufacturing processes, which must include process control, chamber health monitoring and metrology.

While semiconductor metrology and inspection are essential for the management of the manufacturing process at all stages from R&D in the laboratory to prototyping, fabrication, assembly and packaging, and performance verification prior to final deployment, process monitoring is focused on yield improvement by monitoring the tool/chamber health, preventive maintenance for fault detection and for matching the performance of parallel tools/chambers at all production steps.

The production of the latest generation of devices requires sophisticated deposition, etching, lithography and chemical mechanical polishing tools. To support the deployment of smart processes in the semiconductor industry, HORIBA decided to leverage all its technologies for the development of a

wide range of "Optical Smart Sensing" probes, by using the expertise of its global R&D organization (America, France, Japan and Germany) and by collaborating with leading research centers for semiconductors. These probes address the needs of the current and future needs for process monitoring and metrology. Some of them, will be briefly described in this readout.

Etching process

Dry etch is a critical step in the production of Semiconductor, MEMS, Photonics devices, Display and others. The production of the latest generation of devices requires sophisticated etching tools and involve complex processes. To avoid ordinary tool fluctuations, tool-to-tool variations, and tool/process variations after chamber maintenance, routine endpoint detection and chamber health monitoring are required to increase the yield.

Optical Emission Spectroscopy (OES) is a very flexible endpoint detection and plasma monitoring method, which measures the amplitude or amplitude-ratio changes of emission lines emitted by a plasma. OES is the technique with the greatest potential to satisfy the present and future requirements of plasma technology as all plasmas emit radiation depending on their gas composition and plasma parameters.

Figure 1 High throughput and high resolution optical emission spectrometer.

Because it is a rich real-time source of information for plasma etch and deposition monitoring, OES has been used for years by the Semiconductor industry. In reactive ion etching (RIE), induced coupled plasma (ICP) and deep reactive ion etching (DRIE) processes where endpoint monitoring is critical, OES is the preferred technique. It is noninvasive and easily adjusted for any chemistry or film to be etched. In addition to Endpoint monitoring, OES is used for detailed diagnostics such as tool fluctuations, tool-to-tool variations, and tool/ process variations after routine chamber maintenance or repair by means of plasma process-spectra matching.

Typical OES systems involve three main components, a spectrometer, a CCD array detector for recording emission intensity, and software for data processing. A fiber optic probe is used to collect the light at the window of a plasma chamber and transmit that light to the spectrometer. OES data is normally very high in dimensionality and volume, and data analysis and processing methods are required. Effective OES data processing methods could provide significant benefits for prediction of crucial system parameters, system condition monitoring, amongst other etch process control applications.

Figure 2 Optical fibered chemical concentration.

Because the open area becoming smaller and smaller (below 0.5%) OES spectrometers need to provide high throughput and high spectral resolution. To achieve this, specific gratings and optimized optical coupling are required. HORIBA with its long experience and leadership in designing diffraction gratings and optical design, developed a new compact generation of OES (Figure 1). Combined with a patented optical coupling and advance data processing, this new system is the right tool for end point detection and chamber health monitoring.

Besides, HORIBA is also working on other technologies such as Non-Dispersive InfraRed absorption, to improve endpoint detection for low open area. This new technology will be described later in a separate paper.

A dry etch process is always followed by a photoresist stripping and cleaning step. Photoresist stripping, or simply 'resist stripping', is the removal of unwanted photoresist layers from the wafer by using a chemical. The objective is to eliminate the unwanted remaining photoresist material from the wafer as quickly as possible, without allowing any surface materials under the resist to get attacked by the chemicals used. To monitor the cleaning and resist stripping process, HORIBA developed a wide range of chemical concentration monitors to measure the concentration of various chemical. HORIBA's chemical concentration monitors can measure single components as well as up to eight components simultaneously (Figure 2).

Deposition Process

Atomic layer deposition (ALD) is rapidly becoming a standard technique for a wide range of thin film materials and is an essential tool in the semiconductor industry. ALD relies on self-limiting surface reactions of two gaseous reactants in sequential mode to obtain sub-nanometer control of the thickness and conformity of a thin film. The physicochemical properties of the deposited films depend mainly on surface decomposition reactions and growth mechanisms. Therefore, it is important to monitor the flow rate of the reactant gases and fully characterize and understand these processes by utilizing metrology tools that shorten the process optimization cycle and provide real-time monitoring and control in a production environment.

Spectroscopic ellipsometry is a sensitive non-destructive, noncontact, and non-invasive optical technique which is based on the change in the polarization state of light as it is reflected obliquely from a thin film sample. Ellipsometry uses a model-based approach to determine thin film, interface, and surface roughness thicknesses, as well as optical properties (and much more!) for thin films ranging in thickness from a few A to several tens of microns. Spectroscopic Ellipsometry is widely used in the semiconductor industry for the quality check of the different material used during the manufacturing process of a device. It is also used for real time growth monitoring for process optimization and development of new materials.

To monitor the ALD deposition process, traditional spectroscopic ellipsometers are facing some limitations due to the data acquisition rate (0.5 s per spectra) which is not compatible with the frequency of the sequential mode used in this process. To overcome this, HORIBA with its long experience in spectroscopic ellipsometry developed a new generation of spectroscopic ellipsometers capable of acquiring data with a high accuracy at a high speed down to 5 ms per spectra. This new patented technology based on spectral polarimetry (Figure 3) has the merit of no moving parts and fast data acquisition. Currently at a research level, this technology was used to monitor the growth of Al_2O_3 on saphire. Preliminary results are shown in Figure 4.
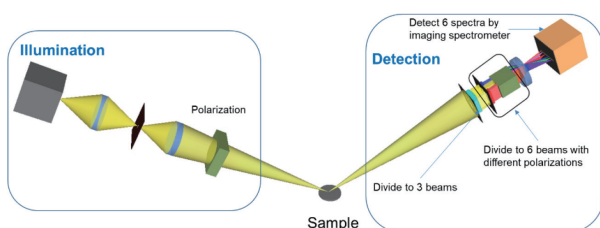

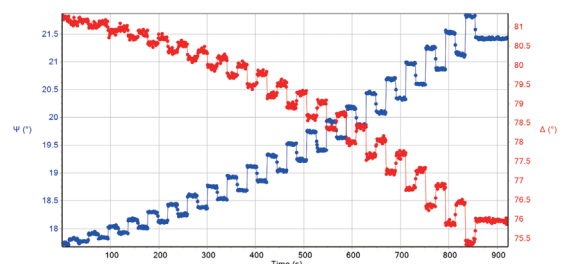Figure 3   Schematic diagram of the fast ellipsometer.

Figure 4   Real time of the Ellipsometric parameters (Y, D) during the ALD deposition of Al_2O_3 on saphire.1&2 are deposition step and 3&4 are passivation step

Lithography process

A pellicle is a membrane used to protect the photomask from contamination during high-volume semiconductor manufacturing. It is mounted a few millimeters above the surface of the photomask. Highly particle free and transparent pellicle is critical to enable high yield and throughput in advanced semiconductor manufacturing. While for Deep Ultraviolet (DUV) lithography, there are established material for the pellicle, Extreme Ultraviolet (EUV) process requires the development of new materials as 13.5nm light is absorbed by most of them. In addition to transparency, stringent thermal, chemical, and mechanical requirements must be achieved. We have seen tremendous progress in carbon nanotube membrane development in the past year and, based on our strong collaborations with our partners, we believe that it will result in a high-performance pellicle solution in the near future. Beside the transparency, one of the challenges during the lithography process, is the particle inspection onto the pellicle and frame and the pellicle health monitoring during the lifetime of its use. To improve the lithography process yield, HORIBA, after more than 40-year experience in photomask inspection by laser scattering technology, has developed a new Particle detection system integrating several proprietary technologies to count, localize and identify the particles, while at the same time evaluating the health of the pellicle. This system (Figure 5) is based on a modular design approach, combining several HORIBA proprietary technologies such Laser scattering, Raman Spectroscopy and Spectroscopic Ellipsometry. It allows the user to evaluate the particle distribution on a pellicle with a high efficiency (minimizing the false detection), to identify the particles location and composition and to evaluate the health of the pellicle.

Figure 5   Photomask inspection system with particle remover and metrology probes.

Chemical Mechanical Polishing

The chemical mechanical polishing (CMP) is a polishing process which uses a chemical slurry formulation and mechanical polishing process to remove unwanted conductive or dielectric materials on the silicon wafer, achieving a near perfect flat and smooth surface upon which layers of integrated circuitry are built. The process involves both chemical attack and abrasive removal by using CMP slurry. The CMP slurry, a polishing powder, can be divided into oxide slurry and metal slurry depending on the film to be polished. The use of CMP slurries, and number of CMP steps in Integrated Circuit processing is growing exponentially. As, it is becoming a critical step for the manufacturing leading edge devices, slurry quality control is critical to achieving the lowest defectivity and cost of ownership. To monitor the quality of the slurry, HORIBA by using its expertise in Laser scattering and Dynamic scattering technologies (Figure 6) has developed a smart particle size analyzer which integrated in the CMP tool provide in real time the particle size distribution form few tenth of nm to several microns. Traditional laser scattering method is limited to particle bigger than 80 nm and not able to analyze multi-model size distributions with a high resolution as most CMP slurries contain a mixture of particle sizes. To overcome this challenge, HORIBA developed a new sensor based on the measurement in real time of the optical absorption of a solution under Centrifugal sedimentation. The dynamic measurement of the light optical absorbance variation due to a particle crossing the light beam is correlated to the particle size distribution by using a dedicated mathematical model. This new technology allows the quality control of the slurry with a high accuracy. In Figure 7, is displayed the picture of the system.

Figure 6   Dynamic Light Scattering particle size analyzer.

Figure 7   Dynamic absorption particle size analyzer.

Material characterization

High quality materials are necessary to improve the performance and reliability of the devices. The reliability of the devices is tightly related to the presence of defects such as dislocations, stacking faults or non-uniformity of thickness, composition and properties, which can be created during the different technological steps followed to build up the device.

Raman Spectroscopy and photoluminescence are non-destructive and non-invasive light scattering technique, whereby a sample scatters incident light from a high intensity laser light source (Figure 8). Most of the scattered light is at the same wavelength (or color) as the laser source and does not provide useful information. However, a small amount of light is scattered at different
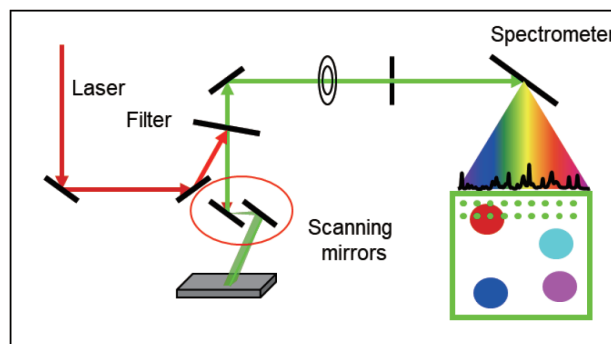

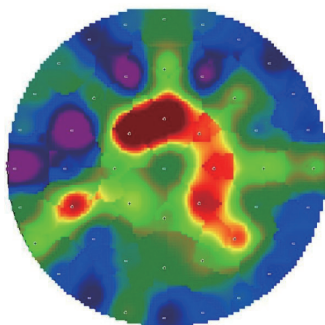Figure 8   Schematic diagram of the Raman/PL probe.

Figure 9　Germanium composition in $Si_{(1-x)}Ge_x$ as measured by Raman spectroscopy
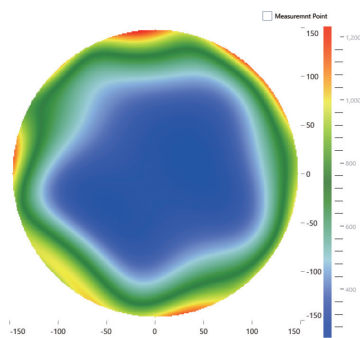

Figure 10　Defects distribution of a graphene film deposited on c-Si as measured by Raman spectroscopy (D band intensity)

Figure 11　Bench-top Micro-XRF analyzer.

wavelengths (or colors). While in Raman spectroscopy, the emitted spectrum is a fingerprint of the chemical structure, phase, polymorph, crystallinity, and molecular structure of the sample, in photoluminescence the emitted light is a fingerprint of the bandgap and electronic properties of the materials. Both techniques are analytically very powerful, as they provide information with submicrometric spatial resolution on defects and material properties. While in R&D both technologies are used for process optimization and the development of new materials, in production only low throughput photoluminescence systems are used for quality control of compound semiconductors. To be used in production for screening 2D materials at the different steps of the devices production without damaging the sample, high sensitivity Raman spectroscopy, and high throughput (fast measurement time) system is required.

To achieve these requirements, HORIBA by using its long experience in Raman spectroscopy, is developing a new generation of Raman and photoluminescence probes which combined with a fast data acquisition system, allows the user to evaluate the composition and localize defects on a large wafer at a high speed with a high sensitivity and without damaging the sample.

These new probes are compact and fully automated. They are based on the use of patented HORIBA technologies for fast laser scanning and on the fly data acquisition processing. Performances like evaluating the quality of 2D materials deposited on a 12" wafer size have been achieved in less than 100s for 49 points. Such performances, allow the user to optimize their deposition process and can also be used for screening defects in the production line with a high throughput. In Figure 9,10 are displayed the distribution of the composition of germanium composition in a film of $Si_{(1-x)}Ge_x$ deposited on a 8" c-Si wafer size and the intensity of the Raman D band of a graphene film deposited on a 12" wafer size have been achieved in less than 100 s, to be replaced by 12" wafer size have been achieved in less than 2 nm.

As the current yield of the deposition tools of 2D, is not very well controlled, Integrated metrology is needed to monitor the quality of the deposited material. Thanks to the compactness of these probes, they use as integrated metrology can be considered.

Besides the defects, contamination and impurities which might happened during the different step of the manufacturing process, are also a concern in the semiconductor industry. X-ray fluorescence (XRF) is a non-destructive elemental analytical technique to identify what elements are contained and to determine how much concentration of the elements are contained in a material. It is based on the measurement of the fluorescence signals emitted from a material under X-Ray excitation. Among XRF analyzers, energy dispersive X-ray fluorescence (EDXRF) analyzers are more suitable for screening materials from the initial stage to the end.

Since 1956, HORIBA continuously developed Energy Dispersive XRF analyzers. HORIBA XRF analyzers can be used for metal film thickness, failure analysis and for the detection of impurities and contamination. HORIBA XRF technology can be used in-line and off-line. In Figure 11, is provided an image of the bench-top system used for failure analysis.

Conclusion

In this material "era" where integration of new materials is required, the control of the different processes involved in the manufacturing of semiconductor devices is critical. HORIBA with its long expertise in developing solutions for flow control and material characterization are addressing these new needs with innovation. For each step of the production process, HORIBA is able to provide a solution capable to provide valuable information on the process tool by collecting data around the process chamber and by analyzing the results of the process with analytical technologies. To achieve this, HORIBA is strengthening its global R&D organization and collaboration with key R&D organizations and will continue to look for innovative technologies.

* Editorial note: This content is based on HORIBA's investigation at the year of issue unless otherwise stated.

Ramdane BENFERHAT
OSS Manager,
Corporate Strategy Division
HORIBA STEC, Co., Ltd.

Feature Article

Raman Microscopy Applied to the Development and Characterization of Next Generation Cutting-Edge Semiconductor Devices

次世代最先端半導体デバイスの開発および特性評価へのラマン顕微鏡の応用

Fran ADAR

Raman spectroscopy has been used since the early 1960's for the analysis of semiconductor materials, at a time when visible lasers became available and became the default source for Raman measurements. In the mid 1970's the Raman microscope was introduced[1]. Consequently as the integrated circuit business was developing, the application of Raman microscopy to the characterization of the materials for the analysis of device performance and engineering became important. Clearly applications to silicon were most relevant and included the measurement of stress, p-type doping (at high levels), crystallite size in polysilicon, and orientation as well as contaminant identification. In compound semiconductors more phenomena were explored. These included composition in alloyed semiconductors, doping of all types, and surface electrical fields which affect the doping and the depth of the surface depletion layer. Consequently, by tuning the excitation laser wavelengths different depths of the materials could be probed because of the dependence of the light penetration depth on wavelength. This enables differentiation of the characteristics of the surface depletion layer from the bulk. In this article we will review these effects historically in order to suggest how these phenomena can be pursued in wide bandgap semiconductors being developed for the next generation of devices. The article will also include a description of measurements on the nano scale, and the integration of photonics in integrated circuits.

ラマン分光法は1960年代初頭から半導体材料の分析に用いられてきた。当時は可視レーザーが利用できるようになり、ラマン測定の励起光源として標準的に使われるようになった時期である。1970年代半ばにはラマン顕微鏡が開発され[1]、集積回路の発展に伴って、デバイスの性能解析などにつながる材料の特性評価の分野で重要な位置を占めるようになった。その典型例がシリコン半導体への応用であり、応力測定、p型ドーピング（高濃度）、ポリシリコン中の結晶サイズ、配向性評価、不純物同定などが行われた。化合物半導体では合金組成や様々な種類のドーピング、表面空乏層の深さに影響を与える表面電解など、さらに多くの特性が評価されるようになった。光が材料に浸透する深さは波長に依存するため、励起レーザーの波長を調整することによって材料表面から深さ方向に異なる位置の分析が可能になり、表面空乏層の特性をバルク特性と区別して評価できるようになった。本稿ではこれまでの様々な評価とその効果についてレビューし、次世代半導体デバイスとして開発されているワイドバンドギャップ半導体においてどのように適用できるのかを提案する。また、ナノスケールでの測定や集積回路における光集積化についても解説する。

Introduction

The title for this year's Masao Horiba Award was "Analysis and measurement technologies that contribute to the development of next-generation semiconductor devices." The next generation of semiconductor devices

1. will be continuing reduction of the size of the device structures below μm resolution,
2. will include optical integration on the integrated circuits, and

3. will include the use of high bandgap materials for high power applications.

Sub µm technology

Sub µm lithography developments go back at least to 1983 and were reviewed in 1986 when the field was still in the regime of university research[2]. The goal is to enable the production of a two-dimensional pattern of arbitrary structure with sharp sidewalls that are significantly smaller than what is possible with conventional optical methods that are determined and limited by the wavelengths of the light. Not only is the method of patterning the photoresist important but the ability of the photoresist itself to produce the desired pattern is considered. Several schemes for producing the lithographic images were reviewed in the above mentioned publication - optical projection photolithography, contact photolithography, holographic lithography, electron beam lithography, X-ray lithography, and ion lithography. Degradation of intensity contrast at the recording plane can result from diffraction, scattering, secondary electrons, penumbra, aberrations, distortions, etc. In addition, registration of subsequent masks can be a problem. This early work produced feature sizes of the order of 100 nm. Spatial resolution has been improved to better than 50 nm[3,4] using electron beam lithography and then 10 nm most recently[5]. For me tools of interference lithography are of particular interest because there are clever ways to pass coherent light through multiple transmission gratings and produce patterns. Interestingly, this technique depends on diffraction gratings with short pitches, fabricated from, for example, metals on Si_3N_4 membranes, materials very different from the gratings that we use in our instruments. As an example reference [4] discusses the use of electrohydrodynamic lithography (EHL) for sub-50 nm patterning and shows the successful use of a wedge geometry for varying hole patterns.

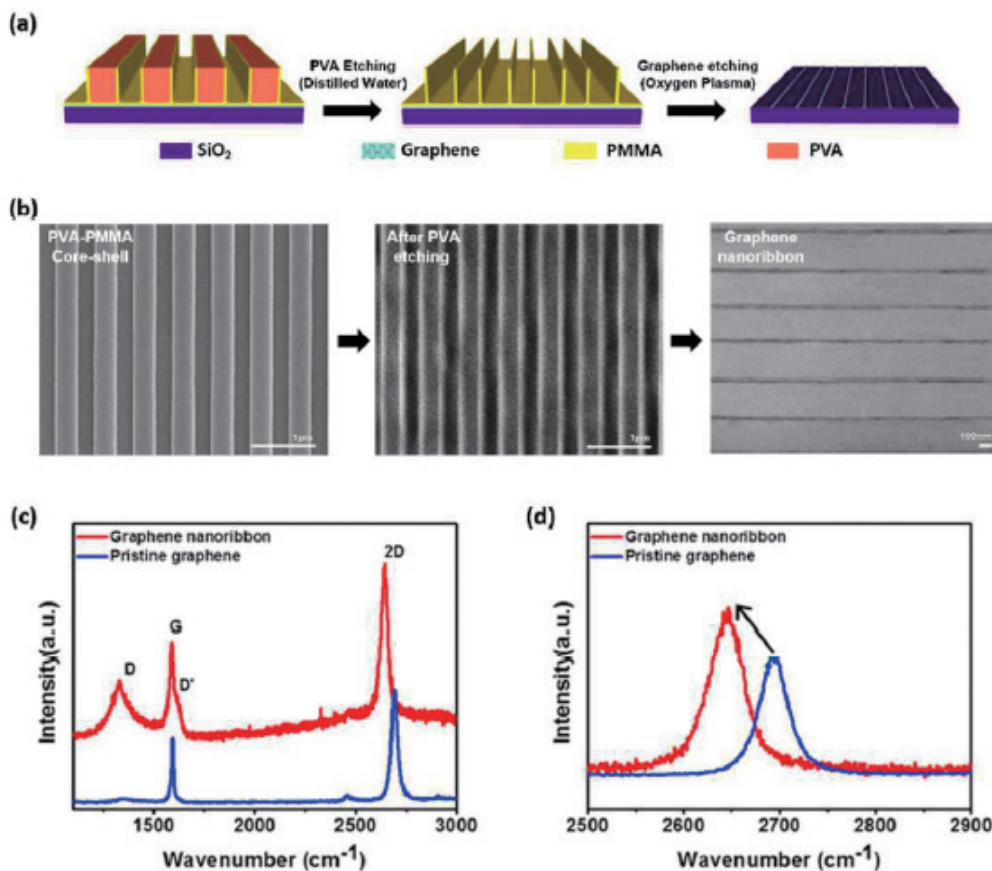Figure 4 in that publication (reproduced here as Figure 1)

Figure 1   (a) Experimental procedure for the fabrication of a ~30 nm wide GNR array and (b) SEM images of the fabrication process for GNR's using core-shell-like nanostructures. (c) Raman spectra of pristine graphene and GNR's. D and D' bands appear in the GNR's. (d) 2D band is red-shifted owing to the strain in the GNR. Reproduced with permission from RSC Nanoscale 2017 00 1-3 Figure 4.
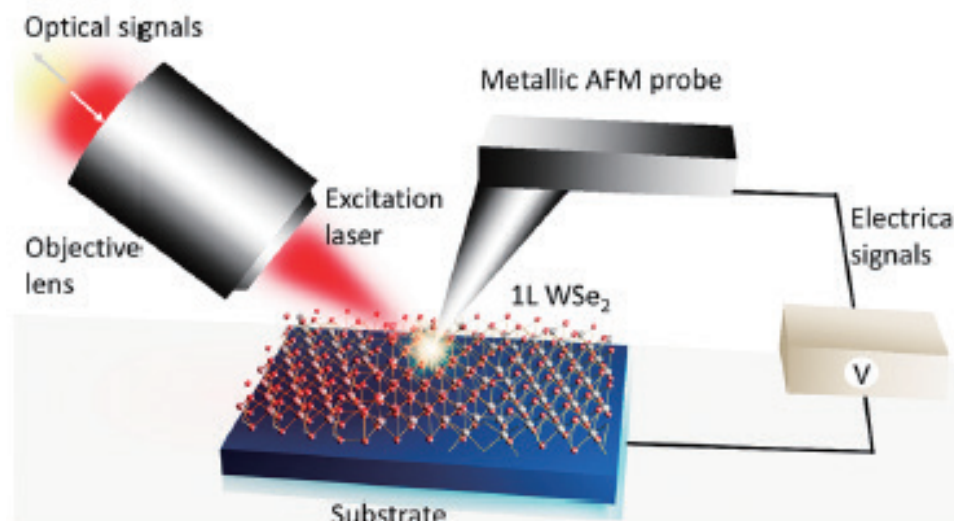
Figure 2 Experimental setup. Schematic diagram of the experimental setup used in the work of reference [8] to study the optoelectronic behavior of grain boundaries in 1L WSe2. *In situ* KPFM (Kelvin Probe Force Microscope) and TEOS (Tip Enhanced Optical Spectroscopy) measurements performed in the same experimental setup enable a direct correlation of topographical, excitonic, chemical, and electrical properties at the nanoscale. Reproduced with permission from W. Su, et.al, J. Phys. Chem. C 2021 125 26883 Figure 1.

shows the fabrication technology for a 30 nm wide graphene nano-ribbon (GNR) array. Note that the ability to fabricate this pattern depends on the properties of the polymer photoresist as well as the patterning technology. And the Raman spectrum indicates the nano-ribbon structure (by the presence of the D band) and strain (by the shift of the 2D band).

Nanoscale Raman microscopy

Since the mid 1970's the Raman microscope has been useful in analyzing spots as small as 0.5 μm in order to measure strain in silicon[6], and contaminating spots, among other things. In order to achieve comparable information on this nano-spatial scale, an AFM (atomic force microscope) coupled to a Raman microscope has been employed. Especially when TERS (tip-enhanced Raman spectroscopy) is employed, Raman signals from a region comparable to the size of the tip have been recorded[7]. While this reference (7) reviews much of the work until then (2013), it does not show spectra of silicon although it does treat carbon nanotubes and photovoltaic materials. One of the awardees at the Masao Horiba Awards was one of the earliest innovators of this technology[8] in which metal dichalcogenide (MDC) films were studied, and a Raman microscope with an AFM "accessory" is now commercially available from HORIBA. Note that in order to achieve nm scale resolution in the Raman analysis it is necessary to implement TERS. A typical scheme in which TERS is implemented for opaque materials is shown in Figure 2, which has been extracted from reference [8]. The excitation laser impinges on the sample from the side so that the AFM probe with a SERS-active coating (surface enhanced Raman spectroscopy) of silver or gold can be brought into close proximity to the surface. Typically measurements are made with the TERS probe close to the surface and then retracted; with the tip retracted the signal is the standard far-field signal, but with the probe close to the surface, the signal contains the near field contribution as well; the difference between the two signals is the TERS signal.

Because of the enhancement in carrier mobility when silicon is stressed, Si_xGe_{1-x} buffer layers were introduced to produce strain in silicon active layers and enable production of ultra-large integrated electronic circuits. But nanoscale fluctuations in the strain distribution were known to reduce the performance of the devices. Consequently, there was interest in recording Raman spectra on the nm scale in order to control the device quality. TERS Raman signals from strained silicon were reported in 2007[9]. Figure 3 is reproduced from that publication and the spatial resolution, in nm rather than μm, was determined by the diameter of the tip.

The following paragraphs describe various phenomena in silicon that can be studied by Raman and followed on the nm scale with TERS.
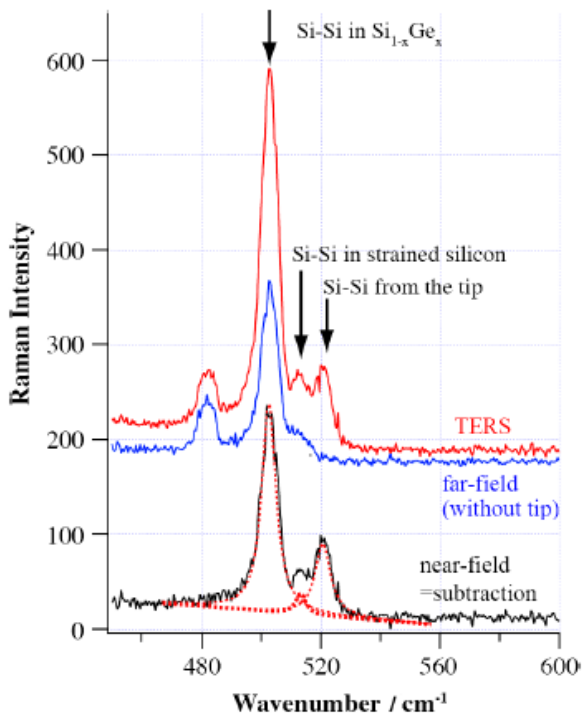
Figure 3   TERS spectra of strained silicon and the far-field spectrum. The black line is the subtracted spectrum (near-field spectrum) between TERS and far-field spectrum. Dotted lines are the Lorentzian curve-fitting for the near-field spectrum. Reproduced with permission from N. Hayazawa, et.al,. J. Raman Spectrosco 2007 38 684 Figure 6.

Group IV Semiconductors, especially Si

With lasers in the visible part of the spectrum, scattering is always done in the back-scattering configuration, and this is always the case when using a microscope for excitation. In Si, one can monitor the orientation (using polarization conditions), strain (by measuring spectral shift due to the geometry of the integrated circuit), crystallite size in polysilicon (by measuring spectral shift and linewidth), and temperature (by taking the ratio of the anti-Stokes to Stokes scattering). Information on this can be found in references [6 and 9].

There is one more phenomenon seen in silicon that is rather interesting and potentially useful. When Si is heavily doped with ions producing p-type doping, there are possible electronic transitions between levels of the valence band. Because these transitions are of the order of 500 cm^{-1} which is a value quite close to the phonon value, there is an interaction called the Fano interaction which describes coupling between a state with a narrow set of values (the phonon) and a continuum of states with a larger set of values (the electronic transitions). This phenomenon has been known in Si for many years, and the result is a distorted lineshape of the phonon[10]. Figure 4 is reproduced from reference 10 (Figure 2). The authors even discuss how Raman measurements can be used for
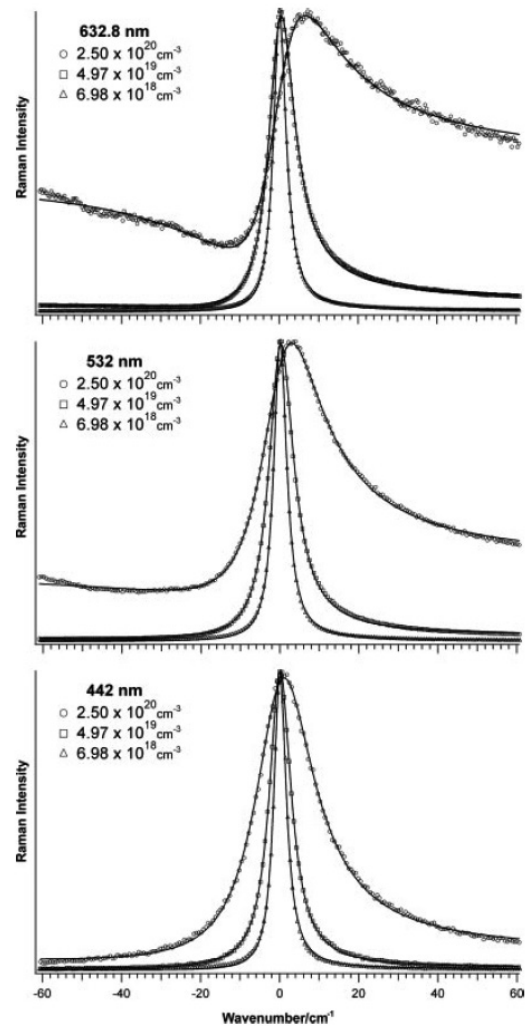

Figure 4   Raman lineshapes versus scattering wavelength for three thermally diffused boron doped Si(100) samples at excitation wavelengths 632.8, 532, and 442 nm. The experimental data (discrete points) were fitted with the modified Fano function (solid lines) with a least-squares computer fit which used q and Γ as adjustable parameters, defined in the reference. The spectra were normalized by the maximum peak value of each concentration. Reproduced with permission from B.G. Burke, et.al., Raman study of Fano interference in p-type doped silicon J Raman Spectrosc. 2010 41 1759-1764 - Figure 2.

diagnostics of doping in circuits as they are being fabricated.

The other Group IV semiconductor of interest is Ge. Even though the first transistor was made in Ge before 1950, since about 1960 all commercial transistors have been based on Si. That is until SiGe has been implemented. SiGe introduces strain which enhances carrier mobility, provides the ability to engineer the bandgap and to integrate CMOS logic with heterojunction bipolar transistors allowing it to be used on mixed signal integrated circuits for applications such as telephones[11]. In principle the frequency of the Raman bands should enable one to calculate the composition, but in this system, strain induced by the differences in atomic size and interatomic spacings also cause spectral shifts. However, using polarization
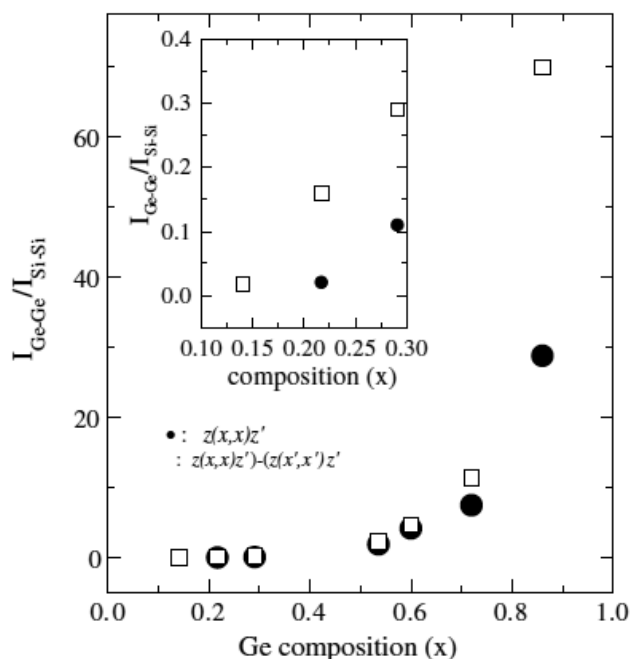
Figure 5   Calibration curve for x, the proportion of Ge in a SiGe alloy, based on I_{Ge-Ge}/ I_{Si-Si} ratio obtained from curve-fitting of the unsubtracted: $z(x.x)z'$ ● and subtracted: $[z(x.x)z']-[z(x',x')z']$ □ spectra. Reproduced with permission from S. Rath, et. al,. Semicond. Sci. Technol. 2003 18 566 Figure 10.

Figure 6   Combined dispersion curves using data from four polytypes. For each polytype, the Raman accessible values of $x=q/q_{max}$ are marked at the top of the figure. Reproduced with permission from D.W. Feldman, et.al., Phonon Dispersion Curves by Raman Scattering in SiC, Polytypes 3C, 4H, 6H, 15R and 21R Phys. Rev. 1968 173 3 787-793.

measurements to separate the various effects, a calibration protocol based on intensities was established[12]. Figure 5 shows the calibration curve of Ge in Si.

Before leaving this review of Group IV semiconductors, there is another system that has to be mentioned. SiC is analogous to silicon, germanium, and diamond, except that one atom in the cubic unit cell is Si while the second is C. Like silicon, germanium and diamond, it is also an indirect gap material (E_g ~3eV) making it one of the wide bandgap materials that will be exploited in the next generation of semiconductor devices; its large bandgap makes it a good substrate for working at higher temperatures and consequently higher power.

SiC actually occurs in many polytypes that are related to each other by systematic rotations around the (111) axis of the cubic phase. The Raman spectra of these materials are quite interesting, and it is not difficult to differentiate them[13]. Figure 6 is extracted from reference 13 and represents a consolidated dispersion curve for several polytypes. The X axis corresponds to the Brillouin zone of the cubic polytype. For each of the other polytypes the Brillouin zone of the cubic phase is folded to accommodate the number of layers in the identified phase. H indicates a hexagonal phase and R indicates a rhombohedral phase. The mode derived from the cubic TO for all polytypes is close to 800 cm^{-1} and would not easily enable
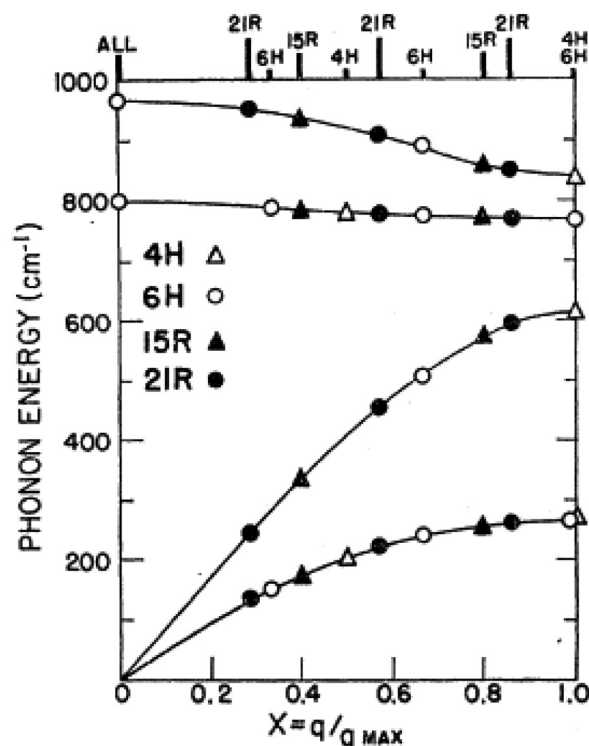
identification. The mode derived from the cubic LO mode does vary from about 970 to 830 cm^{-1}, but it can also be affected by doping[14]. Graded doping was used to study the interaction between carrier transport and phonon properties; it was shown that line shape analysis provided information on the damping of free carriers as well as carrier concentrations. The effects of doping in SiC are analogous to those in III-V semiconductors which will be discussed in the following section. (The meaning of TO, transverse optical, and LO, longitudinal optical, modes will become clear in the next section on III-V semiconductors.) However, the folded acoustic modes, especially the LA (longitudinal acoustic) mode varies quite a bit in the different polytypes, in Figure 6 between about 240 and 600 cm^{-1}. Because of the ability to form polytypes easily by rotations around the cubic (111) axis, defects are common in engineered materials[15] and can be analyzed by their Raman spectra. This is actually discussed in detail in reference 15. The effects of strain[16] in SiC have also been documented.

III-V Semiconductors

While the longitudinal and transverse optical phonons in Group IV semiconductors (Si, Ge, and Diamond) are degenerate (ie,. they have the same energy), in III-V semiconductors the two are split because of the electric field that the inequivalent ions create during vibrational

motion. A good reference for many semiconductor materials is the European Commission's "Nostradamus" project[17]. From this reference the LO (longitudinal optical) and TO (transverse optical) frequencies of most of the semiconductors of interest can be found.

There is another effect in III-V semiconductors that results from the fact that free electrons from doping can shield the electric field of the LO phonons[18]. In fact, the free electrons form a plasmon in the material and the plasmon interacts with the LO phonon producing the L+ and L- modes seen on the left side of Figure 7. When the density of free electrons is very high, the frequency of the L- phonon collapses to that of the TO phonon and the frequency of the L+ plasmon follows the trajectory of a free plasmon. The next figure, reproduced from reference 18 shows the spectrum of a GaAs sample doped at 1.9×10^{18} cm^{-3} (left, for different polarization conditions) and then the dependence of the energies of the LO phonon and plasmon on the square route of the dopant levels (right). This is the earliest measurement of the coupled LO phonon-plasmon modes of which I am aware. Note that the measurement was made with a Nd:YAG laser whose emission wavelength is below that of the bandgap; the measurements were made in the bulk and avoided surface field effects.

When using a visible laser investigating III-V semiconductors, the depth of penetration of the laser and the thickness of the surface depletion layer will affect these measurements. Much of the information necessary for design and interpretation of such measurements are available in reference [17].

Semiconductor engineers often are interested in tuning the properties of semiconductors for devices by alloying materials that have (almost) equal interatomic spacings; $In_xGa_{1-x}As$ is a good example. The reason to select a pair with almost equal interatomic spacings is to minimize strain and to maintain single crystal structure, ie,. minimize dislocations and avoid cracking. There is a good reference that discusses how alloying affects the phonons[19]. By alloying, the engineer can tailor the bandgap for a particular application. For instance, communication lasers use a bandgap that matches the wavelength where fiber optics that carry the laser signals have minimum losses (1.5 µm), and InGaAsP is used in the design of the laser.

In understanding the observed phonon behavior of III-V alloys there are two possibilities - two- and one-mode behavior. Figure 8 reproduces the behavior for the two types of mixed phonons and is reproduced from reference [19].
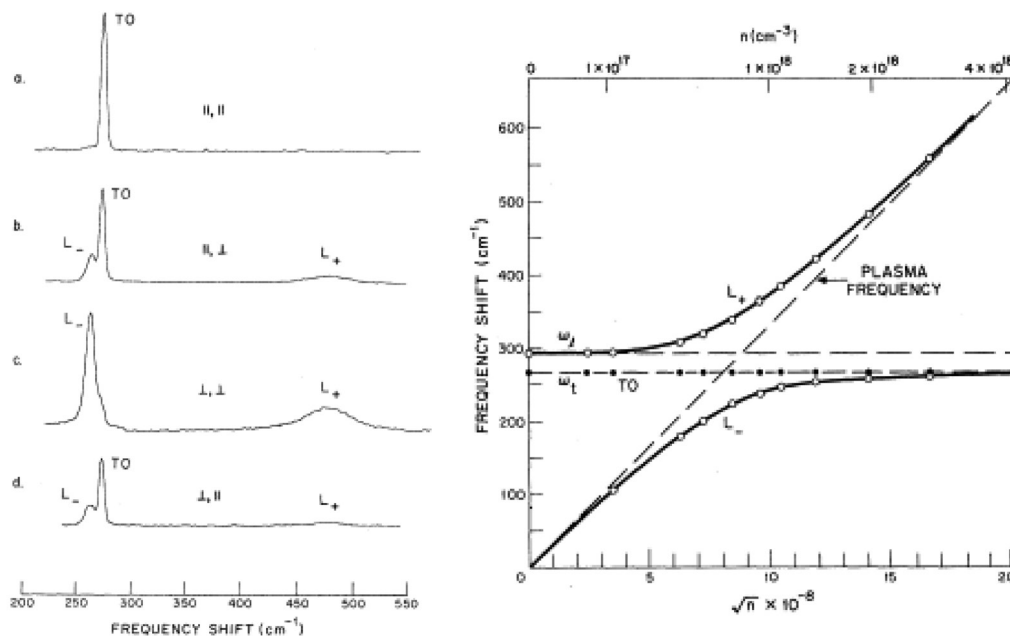

Figure 7 Left: Intensity and polarization properties of the Raman-scattered light from GaAs at liquid He temperature for a sample with n=1.9x10^{18} cm^{-3}. The scattering angle is 90° with the incident and scattered light propagating along a (100) direction. The ‖ and ⊥ symbols indicate the polarization of the incident and scattered light with respect to the plane of scattering. These traces are uncorrected for the system response, and the gain in b is lower than the others. Right: Frequencies of the L+ and L- modes (mixed longitudinal phonon-plasmon modes) as a function of the square root of the carrier concentration. Reproduced with permission from A. Mooradian and A.L. McWhorter 1967, Polarization and Intensity of Raman Scattering from Plasmons and Phonons in Gallium Arsenide Phys. Rev. Let. 19 15 849-852 Figures 1 and 2.
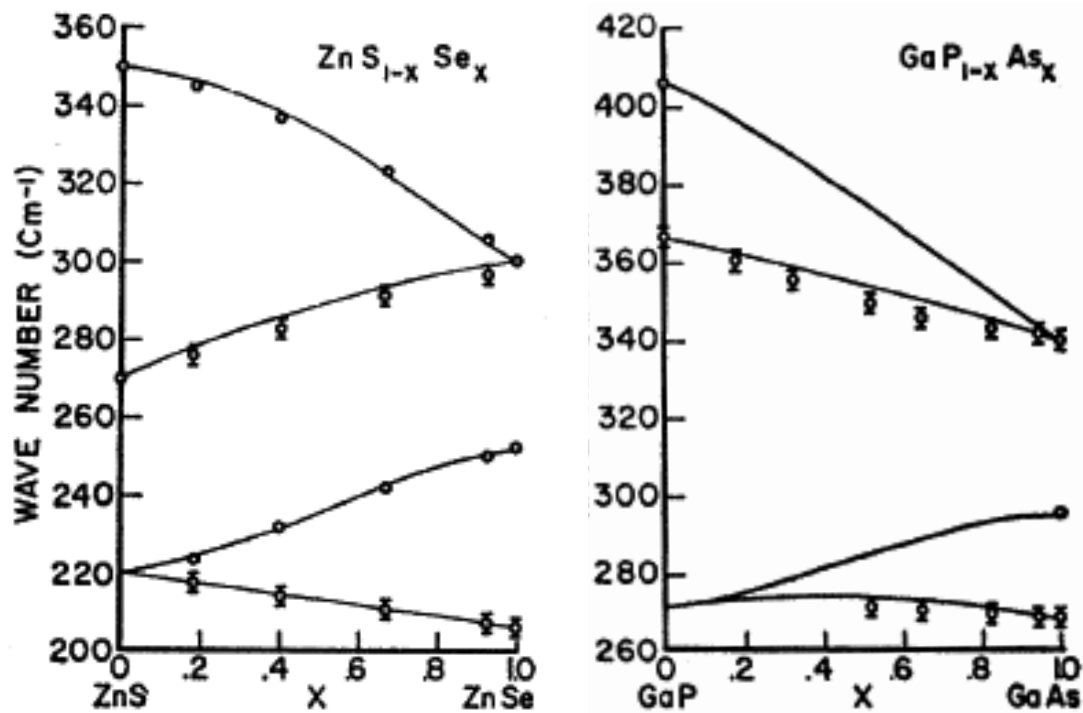
Figure 8   Left: Two mode behavior in ZnS$_{1-x}$Se$_x$. The open circles O represent the measured LO phonons and Φ represents the measured TO phonons. Right: One Mode Behavior in GaP$_{1-x}$As$_x$. The solid lines in the figures, ———— indicate theoretical predictions explained in the publication. Reproduced with permission from I.F. Chang and S.S. Mitra. Application of a Modified Random-Element-Isodisplacement Model to Long-Wavelength Optic Phonons of Mixed Crystals Phys Rev 1968 172 3 924-933 Figures 2 and 3.

In both figures the measured phonon frequencies at the endpoints represent the pure materials. In the two-mode behavior of ZnS$_{1-x}$Se$_x$ at any x different from 0 or 1 there is a set of LO and TO phonons whose behavior represents a mixture of the two pure materials. In the one mode behavior of GaP$_{1-x}$As$_x$ there is only one TO mode and one LO mode for any value of x. The cited reference [19] describes the origins of these differences.

There is another phenomenon that the analyst needs to keep in mind. Because of pinning of electronic states at the surfaces of doped III-V semiconductors there is a layer depleted of electrons. Consequently if one measures a Raman signal with a laser that does not penetrate deeper than that surface depletion layer, the LO phonon frequency will reflect a carrier-free material. If a longer wavelength laser is used that does penetrate through the surface depletion layer, then the contributions to the scattering from that region will reflect the carrier concentration. The wavelength dependence of the absorption region and a means to calculate the space charge layer are included in reference [17].

Transition metal dichalcogenides

Probably the most exciting and active area in semiconductor research now is that of the transition metal dichalcogenide (TMD) films. Because of the potential to tailor their electronic and optical properties they are being considered for design into the next generation of devices. Raman microscopy, including TERS, provides the ability to observe the effects of crystal edges and internal twin boundaries with up to ~15 nm spatial resolution, correlating spectral shifts with PL (photoluminescence intensity) and the exciton diffusion length[20].

Optical Integration on Integrated Circuits

The next generation of technology will make use of chips that integrate photonics with electronics in order to increase speed of data transfer, speed of calculations, simplify design, and reduce energy consumption. The goal is to perform all functions on a silicon substrate. But a major hurdle is the intrinsic characteristic of silicon, that it is an indirect gap material and therefore is not an immediate choice for light generation. In addition, the integration of materials not normally used on a silicon integrated circuit (IC) will also be a challenge.

While a final solution for full integration is not yet available, considerable strides have been made, and are reviewed in a 2024 publication[21]. The ultimate goals include the ability to fabricate in silicon foundries, to shrink the chips, to increase the number of devices that can be integrated on a chip, and to minimize power consumption. Currently photonic integrated chips are dominated by communications applications, but it is foreseen that such technology can accommodate quantum

computing and sensors, especially for biomedical application, while photonics provides data links, electronics control readout and digital signal processing. Because photons do not interact with each other, they transmit information with fidelity, but electrons do interact and can therefore be used for switching and computing. On the other hand, silicon photonics carrier waves are in the 100's of THz range whereas silicon electronics are in a range less than THz. Hurdles to be overcome include: Hurdles to be overcome include:

• identifying an appropriate laser source. If it will be something like InAsP, it has to be incorporated on the chip, and possibly designed as a comb for multiwavelength output

• designing the I/O for the photonics and incorporating them on the chip.

• designing high confinement waveguides for modulation, integrating Wavelength Division Multiplexer (WDM) (for disentangling parallel transmission of multiple signals over different wavelengths) and incorporating focal plane array detector systems in order to detect simultaneously the various channels.

• Incorporating Si/Ge avalanche photodiodes (APD's).

• integrating a variety of dissimilar materials.

Raman microscopy can assist in analyzing materials in all of the above. In addition to the excellent review of the engineering challenges described in reference [21] there are some developments that are worthy of note.

In 2004 it was reported that full optical control of light on a silicon chip was achieved by using an "all-optical gate based on a silicon micrometer-size planar ring resonator" operator with low pump-pulse energies[22]. A continuous wave laser was produced on silicon in 2005[23] by launching a pump laser into a low-loss silicon-on-insulator rib waveguide by using a p-i-n structure on either side of the waveguide to reduce the two-photon absorption losses due to free carriers. The origin of the lasing was the stimulated Raman signal of the silicon of the waveguide. Note that this design requires a pump laser so the requirement for non-silicon materials is not eliminated.

Another innovation of note is inclusion of a Mode Division Multiplexer (MDM) in addition to the WDM; the MDM independently separates spatial modes of each wavelength and ultimately provides a multiplicative effect on the bandwidth of the optical link. Chip to chip transmission was demonstrated between separate silicon

chips[24]. For sure there are, and will continue to emerge, new technologies that will further enable integrated electronics/photonics.

Next Generation Semiconductor Devices; Analysis by Raman Microscopy

The potential of Raman microscopy to the analysis and characterization of the next generation of semiconductor devices requires an understanding of what type of information Raman spectroscopy can provide. This required an extensive review of the contributions of Raman spectroscopy to the analysis of classical semiconductors and which appeared earlier in this document.

One of the most important areas for the future of semiconductor devices is the use of high bandgap semiconductors for high power applications such as for electrical vehicles. This would include SiC, GaN or AlN, and Ga_2O_3. The last one is surprising because until now oxides have been considered insulators but the ability to fabricate field effect transistors has been demonstrated[25]. Polarized Raman spectra from single crystals of Ga_2O_3 have been recorded so it can be assumed that Raman is available for analysis of this material as well[26].

As was stated earlier in this document, work on thin layer metal dichalcogenides is active because of the potential to tune their properties which will provide new capabilities in devices (20). And the article cited above shows a clear path between Raman analysis and electronic properties.

In considering the production of nano-sized electronic devices, we should mention the potential of optical metasurface engineering for large scale production of devices with sub 50 nm scale in silicon foundaries. This is currently not a reality but is certainly being pursued (reference 21).

One last area to be mentioned is the re-engineering of packaging to accommodate the coming requirements for performance, power (heat dissipation), and cost[27]. The trend is seen to be moving from polymeric materials to inorganic materials such as silicon and ceramics in addition to metals for the interconnects. Note that the Raman spectra of ceramics[28] are strong and quite diagnostic of crystallographic phase (which determines the properties of the materials) making Raman an appropriate analysis method.

Conclusion

Raman analysis of semiconductors goes back at least to the late 1960's, about the time that lasers first became available as excitation sources. The wealth of information and effects documented over the years provide fertile ground for the use of Raman microscopy in the design, characterization, and analysis of next generation devices. The phenomena that are amenable to detection by Raman microscopy are well known so it will be straightforward to know how the technology can aid in the characterization of devices under development - whether that means measuring strain produced by the materials used or the local geometry of the device, or measuring composition of alloyed materials (SiGe or III-V semiconductors), or measuring the effects of free carriers which determine device performance. While proof of concept for these innovations is ongoing both in industry and academia, national efforts such as the Chip Act in the United States indicates the high level of awareness for the need for investment.

* Editorial note: This content is based on HORIBA's investigation at the year of issue unless otherwise stated.

[9] N. Hayazawa, et.al, Viualization of localized strain of a crystalline thin layer at the nanoscale by tip-enhanced Raman spectroscopy and microscopy, *J. Raman Spectrosc* 2007 38 684-696

[10] B.G. Burke, et.al., Raman study of Fano interference in p-type doped silicon *J Raman Spectrosc*. 2010 41 1759-1764

[11] Silicon-germanium - Wikipedia

[12] S. Rath, M.L. Hsieh, P. Etchegoin, and R.A. Stradling Alloy effects on the Raman spectra of $Si_{1-x}Ge_x$ and calibration protocols for alloy compositions based on polarization measurements 2003 *Semicond. Sci. Technol.* 18 566-575 2003

[13] D.W. Feldman, et.al, Phonon Dispersion Curves by Raman Scattering in SiC, Polytypes 3C, 4H, 6H, 15R, and 21R *Phys. Rev.* 1968 173 3 787-793

[14] S. Nakashima, et.al., Raman scattering study of carrier-transport and phonon properties of 4H-SiC crystals with graded doping, *Phys Rev.* B 76 2007 245208

[15] P-C Chen. et.al., Defect Inspection Techniques in SiC, *Nanoscale* Res ett 2022 17:30

[16] W.L. Zhu. J.L. Zhu, S. Nishino and G. Pezzotti, Spatially resolved Raman spectroscopy evaluation of residual stresses in 3C-SiC layer deposited on Si substrates with different crystallographic orientations *Appl Surface Sci* 2006 252 2346-2354

[17] Raman and Luminescence Spectroscopy for Microelectronics ISBN 92-828-5011-0

[18] A. Mooradian and A.L. McWhorter 1967, Polarization and Intensity of Raman Scattering from Plasmons and Phonons in Gallium Arsenide *Phys. Rev. Let.* 19 15 849-852

[19] I.F. Chang and S.S. Mitra. Application of a Modified Random-Element-Isodisplacement Model to Long-Wavelength Optic Phonons of Mixed Crystals *Phys Rev* 1968 172 3 924-933

[20] K-D Park, et.al, Hybrid Tip-Enhanced nanospectroscopy and Nanoimaging of Monolayer WSe2 with Local Strain Control *Nano Lett* 2016 16 2621-2627

[21] S. Shakhar, et.al,. Roadmapping the next generation of silicon photonics *Nature Commun* 2024 15.751

[22] V.R. Almeda, C.. Barries, R.R. Panepucci and M. Lipson, All-optical control of light on a silicon chip *Nature* 20014 431 1081-1084

[23] H. Rong et.al,. A continuous-wave Raman silicon laser *Nature* 2005 433 725-728

[24] A.I.Kuznetsov, et.al,. Roadmap for Optical Metsurfaces *ACS Photonics* 2024 doi 10.1021/acsphotonics.3c00457

[25] M. Higashiwaki, et.al,. Gallium oxide (Ga_2O_3) metal-semiconductor field-effect transistors on single-crystal β- Ga_2O_3 (010) substrates, *Appl Phys*. Let 2012 100 013504

[26] B.M. Janzen, et.al, Comprehensive Raman study of orthorhombic κ/ε- Ga_2O_3 and the impact of rotational domains *J. Mater Chem C* 2021 9 14175

[27] The growth of advanced semiconductor packaging | McKinsey and/ or The Five Keys to Next-Generation IC Packaging Design: Part 1 - Semiconductor Packaging (siemens.com)

[28] Database of Raman spectroscopy, X-ray diffraction and chemistry of minerals (rruff.info)

References

[1] George Turrell and Jacques Corset. Raman Microscopy Developments and Applications Academic Press London (1996) and references therein that describe the original publications

[2] H.I. Smith. A Review of Submicron Lithography. 1986 *Superlattices and Microstructures* 2 2 129-142

[3] A. Kojima, H. Ohyl, and N. Koshida Sub-50 nm resolution surface electron emission lithography using nano-Si ballistic electron emitter 2008 J *Vac Sci Technol* B 26 6

[4] S. Lee, et.al. Innovative Scheme for Sub-50 nm Patterning via Electrohydrodynamic Lithography 2017 RSC *Nanoscale* 00 1-3 1-7

[5] N.Mojarad, J. Gobrecht, and Y Ekinci Interference lithography at EUV and soft X-ray wavelengths: Principles, methods, and applications 2015 *Microelectron Eng* 143 55-63

[6] I. De Wolf. H. Norstrom. And H.E. Maes, Process-induced mechanical stress in isolation structures studied by micro-Raman spectroscopy, 1993 J *Appl Phys* 74 7 4490-4500

[7] T. Schmid. L. Opilik. C. Blum. And R. Zenobi, Nanoscale Chemical Imaging Using Tip-Enhanced Raman Spectroscopy: A Critical Review *Angew. Chem. Int. Ed*. 2013 52, 5940-5954

[8] W. Su, N. Kumar, H. Shu, O. Lancry and M. Chaigneau *In Situ* Visualization of Optoelectronic Behavior of Grain Boundaries in Monolayer WSe_2 at the Nanoscale J *Phys Chem* C 2021 125 26883-26891

Fran ADAR

Principle Raman Applications Scientist,
HORIBA Instruments Incorporated,
Ph.D.

Characterization Methods Shaping the Future of 2D Materials in the Semiconductor Industry

半導体産業における二次元材料の未来を拓く特性評価方法

Marc CHAIGNEAU

The integration of 2D materials into the semiconductor industry presents a paradigm shift, promising enhanced performance and efficiency in semiconductor devices. Graphene and Transition Metal Dichalcogenides (TMDs) stand out among these materials, offering unique properties suitable for various semiconductor applications. However, realizing their potential requires overcoming synthesis challenges and ensuring precise characterization. This article explores the role of characterization and wafer inspection methods in shaping the future of 2D materials in the semiconductor industry. It discusses synthesis techniques compatible with their scale up and highlights the current challenges such as uniformity, and defect minimization. The article also focuses on the key characterization properties, thus emphasizing the importance of techniques like Raman spectroscopy and Photoluminescence (PL) spectroscopy, crucial for the successful integration of 2D materials in the semiconductor technology.

半導体産業における二次元材料の活用は半導体デバイスの性能および効率を向上させるパラダイムシフトをもたらす。グラフェンや遷移金属ダイカルコゲナイド(TMD)は数々の二次元材料の中でも特に注目されており, 様々な半導体用途に適しているユニークな性質を持つ材料である。しかし, その特性を生かすには合成方法における課題の克服やより正確な特性評価が求められる。本稿では半導体産業における二次元材料の未来を拓くための特性評価およびウェハの検査方法が果たす役割について述べる。特にスケールアップを実現する合成方法, 均一性が高く欠陥が少ない材料の実現における課題に焦点を当てる。また, 半導体分野への二次元材料の適用に欠かせない特性評価手法であるラマン分光法やフォトルミネッセンス(PL)についても述べる。

Introduction

The world of semiconductors is constantly evolving, and one of the most exciting developments in recent years is the emergence of 2D materials. Among the pioneers in this field is graphene, a single layer of carbon atoms arranged in a two-dimensional honeycomb lattice. Graphene exhibits remarkable properties, such as high electrical and thermal conductivity, exceptional mechanical strength, and extraordinary electron mobility. Alongside graphene who by nature is semi-metallic, Transition Metal Dichalcogenides (TMDs) have gained attention for their band gap, making them suitable for semiconductor applications (Figure 1). Moreover, other 2D materials like h-BN, black phosphorous, and MXenes have also demonstrated promising characteristics. The unique properties of 2D materials open up a myriad of potential applications. These materials hold great promise in energy storage devices, sensors for various industries, optical lighting technologies, healthcare biosensors, photovoltaics, and electronics, including transistors and memories. This article explores the potential of these materials in the semiconductor industry and the characterization and inspection methods that are helping their integration.

Roadmap and Scaling Techniques

In the semiconductor industry, the technology roadmap has been guided by Moore's Law, with a focus on miniaturization and integration of components on silicon chips. However, as traditional scaling approaches face

limitations, the introduction of 2D materials offers a new dimension to continue progress. Happy scaling involved reducing the size of transistors to maintain performance, but heterogeneous scaling now introduces new materials with unique properties to improve overall performance and energy efficiency **Figure 2**[1]. 2D materials present exciting prospects for both front-end-of-line (FEOL, i.e. all the process steps that are related to the transistor itself)
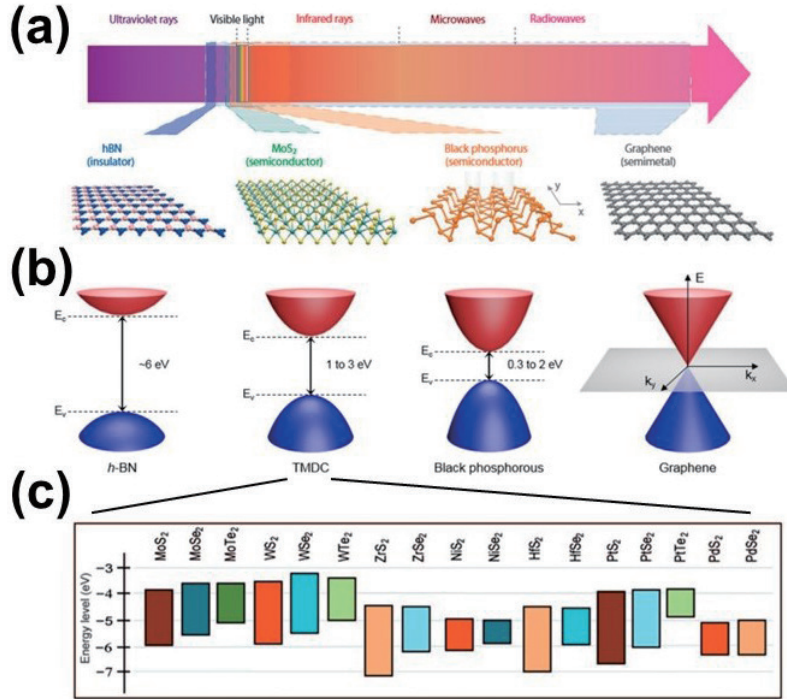

Figure 1　Optical response and electronic bandgaps of typical 2D materials. (a) Energy spectrum of various two-dimensional (2D) materials and their atomic crystal structures. (b) Electronic band structures of hexagonal boron nitride (*h*-BN), transition metal dichalcogenides (TMDCs), black phosphorous, and graphene. (c) Energy level diagrams of selected semiconducting TMDCs.
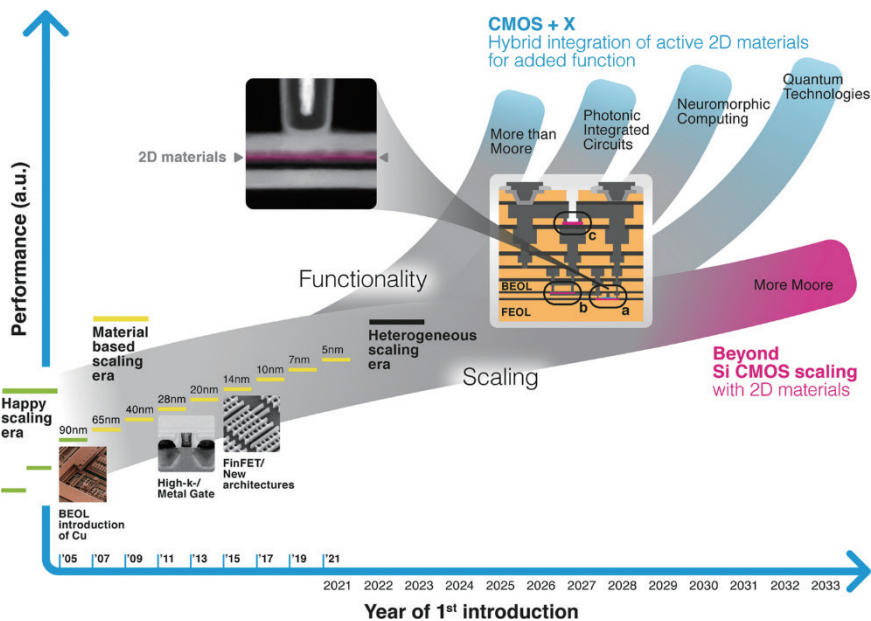

Figure 2　The era of geometrical scaling of silicon technology ended around the turn of the century (green lines, "happy scaling"). Since then, material and architecture innovations like copper interconnects, high-*k* dielectrics with metal gates and FinFETs continued to drive Moore's law (yellow lines, "less happy scaling"). Future scaling, or "More Moore", may require thin nanosheet transistors, where 2D materials are considered ideal candidates (magenta, inset a and transmission electron micrograph). Reproduced with permission from Lemme, M.C., Akinwande, D., Huyghebaert, C. *et al.* 2D materials for future heterogeneous electronics. *Nat Commun* 13, 1392 (2022) Figure 1.

and back-end-of-line (BEOL, i.e. the interconnects between the transistors are formed within a device) applications.

In FEOL, TMDs possess exceptional carrier mobility and bandgap properties, making them suitable candidates for next-generation transistors. These 2D materials can potentially replace traditional silicon-based transistors, leading to faster switching speeds, reduced power consumption, and increased device performance. In BEOL, as integrated circuits become smaller and more complex, interconnects play a vital role in ensuring efficient signal transmission. Graphene with high electrical conductivity and low resistivity can be utilized as interconnect materials, reducing signal delay and enhancing overall chip performance. Still in BEOL, barrier layers are used to protect underlying layers from diffusion and contamination. Hexagonal Boron Nitride (h-BN), known for its excellent dielectric properties, can serve as an ideal barrier material to protect sensitive components in the semiconductor device.

Synthesis Challenges and Methods

Efficient synthesis methods are essential to harness the potential of 2D materials for semiconductor applications. Two main approaches commonly employed in the synthesis of these materials are the top-down approach and the bottom-up approach. The top-down approach involves exfoliating bulk materials to obtain 2D layers. The most well-known example of this approach is the exfoliation of graphite to produce graphene layers. While this method provides a starting point for research and small-scale applications, the scalability and precise control provided by the bottom-up approach with Chemical Vapor Deposition (CVD) make it a leading contender for large-scale commercial production of 2D materials. Indeed, CVD (and its variant MOCVD, Metal-Organic Chemical Vapor Deposition) offers several advantages over the top-down approach, including better scalability to large wafers, the control over layer thickness, and the possibility to easily change the precursors for the growth of heterostructures. However, it also presents its own set of challenges:

a. Precursor Selection: Choosing the appropriate precursor gases is critical to achieving high-quality 2D materials. The selection influences the growth rate, crystallinity, and defect density of the synthesized layers.

b. Substrate Compatibility: The choice of substrate plays a crucial role in CVD synthesis. Different 2D materials require specific substrates with matching lattice constants and thermal properties to ensure successful growth and adhesion. For instance, when growing graphene using CVD, copper foils or nickel foils are often used as substrates. The carbon atoms in graphene align with the lattice structure of the metal substrate during the growth process, promoting the formation of a single-layer graphene with good adhesion to the substrate. Similarly, in the growth of TMDs like molybdenum disulfide (MoS_2), sapphire substrates are frequently utilized due to their close lattice match with the TMD material, facilitating high-quality growth. In both cases, the choice of substrate with appropriate lattice constants and thermal expansion coefficients helps to minimize strain and defects during the growth process, resulting in high-quality 2D materials that are well-suited for subsequent integration into semiconductor devices.

c. Uniformity and Defects: Achieving uniform and defect-free 2D layers across a large-area wafer is a significant challenge in CVD. Factors like temperature, gas flow rates, and reaction time must be precisely controlled to minimize defects and ensure uniform growth.

d. Transfer and Stacking: Once the 2D material is synthesized on a growth substrate, it needs to be transferred from the initial growth substrate onto the desired semiconductor device substrate while maintaining its structural integrity. The choice of the target substrate depends on the specific application and requirements of the semiconductor device. For instance, if the 2D material is intended for FEOL applications, it may be transferred onto a silicon wafer. Integrating the 2D material onto a silicon substrate enables compatibility with existing silicon-based processes current used in semiconductor fabs. On the other hand, in BEOL applications, the target substrate might include various insulating or conducting materials, depending on the intended use of the 2D material. For example, if the 2D material is to be used as a barrier layer or interconnect, it might be transferred onto an insulating material like silicon dioxide (SiO_2) or a conducting material like copper.

The transfer process itself can be delicate and challenging, as it involves peeling the 2D material off the growth substrate and carefully placing it onto the target substrate. Techniques such as dry transfer, wet transfer, and polymer-assisted transfer play a crucial role in the successful integration of 2D materials into semiconductor devices. These methods are employed to preserve the crystalline quality of the 2D material, cover as large an area as possible, and prevent doping from contamination and defects like wrinkles and cracks.

Overcoming the challenges associated with CVD synthesis methods is of paramount importance to fully harness

the potential of 2D materials in the semiconductor industry and facilitate the development of innovative and high-performance devices. To this end, current efforts are being directed towards directly growing 2D materials on silicon or silicon dioxide substrates. This approach offers significant advantages, including streamlining the device fabrication process.

Characterization Techniques for 2D Materials in Semiconductor Applications

As the potential applications of 2D materials continue to expand and are becoming concrete on the market, the semiconductor industry is taking notice. Leading manufacturers of deposition systems are investing in R&D to meet the growing demand, and new deposition systems that enable their synthesis on large wafers are emerging on the market. Meanwhile, major players in the semiconductor industry are exploring actively the possibility to incorporate 2D materials into their next-generation devices. To ensure the successful integration, precise and reliable characterization techniques are essential to check the quality and uniformity of 2D materials.

Characterization encompasses the growth optimization of the 2D materials on template wafers and the quality of the materials after transfer. Several key parameters are of interest (in brackets the main techniques used):

- Thickness and number of layers (Raman spectroscopy, AFM (Atomic Force Microscopy), Reflectometry, Ellipsometry)

- Crystalline quality (Raman spectroscopy)

- Band Gap and stress (Raman spectroscopy and Photoluminescence)

- Carrier concentration and doping level (Raman spectroscopy and Photoluminescence)

- Identification and quantification of defects (point defects, but also cracks, wrinkles, grain boundaries and holes) or contaminants (polymeric, metallic) (Raman spectroscopy and Photoluminescence, AFM)

Indeed, Raman spectroscopy is extensively used for characterizing graphene. Figure 3 illustrates the Raman map of graphene on a 4" sapphire wafer. The Raman spectra of graphene are characterized by three main bands referred to as the G, 2D-bands, and the D-band which appears in the presence of defects within the carbon lattice[2]. Histograms of Raman parameters present the distributions of (upper) the Full Width at Half Maximum (FWHM) of the 2D band, (middle) the D/G intensity ratio, and (bottom) the 2D/G intensity ratio. These Raman parameters respectively provide insights into the crystalline quality (2D FWHM $\sim$ 40 cm^{-1} for graphene grown on pristine sapphire), the defect density (low value is a D/G ratio of $\sim$ 0.13)[3-4], and the doping level through the charge carrier concentration (2D/G ratio $\sim$1.80 for grown graphene on pristine sapphire, carrier concentration estimated to be around 5 x 10^{12} cm^{-2})[5] and the layer thickness[6].

For 2D Transition Metal Dichalcogenides (TMDs), Raman and Photoluminescence (PL) spectroscopy are particularly useful in determining the number of layers[7-9], stoichiometry[10], carrier density[11-12] and the presence of defects[4]. Figure 4 shows Photoluminescence and Raman maps of tungsten disulfide (WS_2), a member of the 2D TMD family, on a 12" Si wafer. The Photoluminescence spectra are primarily characterized by exciton and trion bands, and their intensity ratio enables differentiation between various regions based on charge carrier concentration[13]. The Raman spectra of WS_2 exhibit prominent peaks: E2g (in-plane mode) and A1g (out-of-plane mode)[14]. The
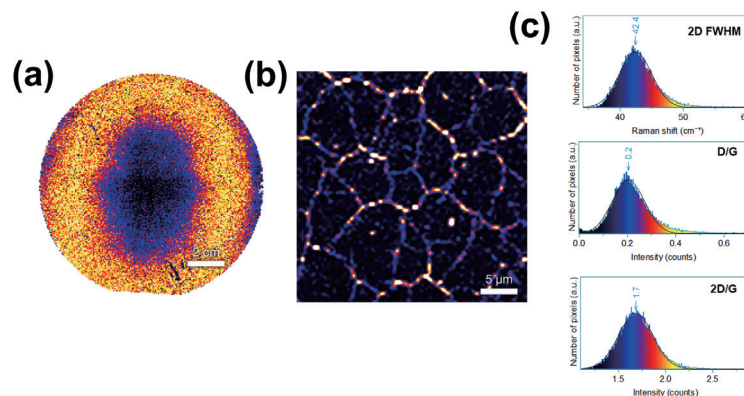

Figure 3 (a) Raman map of graphene on a 4" sapphire wafer, (b) high resolution Raman image on defects, (c) Histograms of Raman parameters (Full Width at Half Maximum (FWHM) of the 2D band, D/G intensity ratio, and 2D/G intensity ratio).
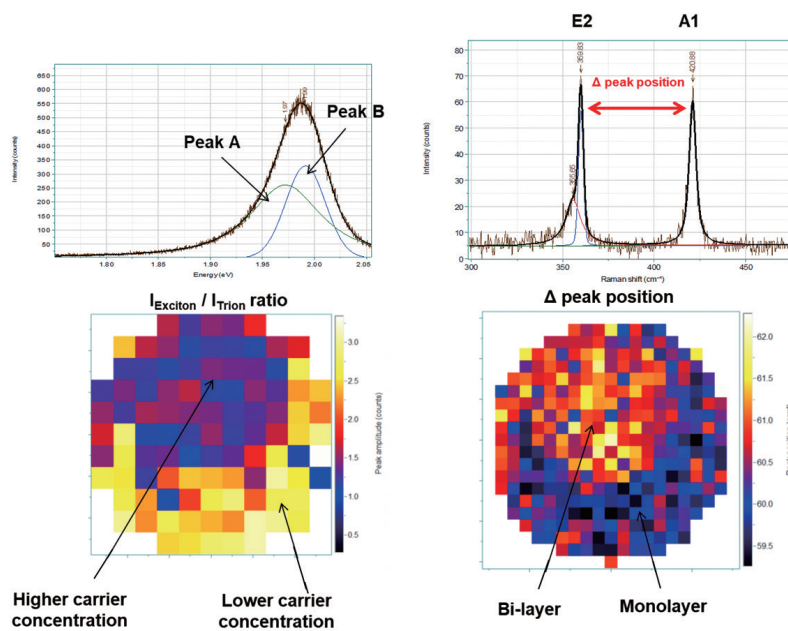
Figure 4   Photoluminescence (left) and Raman maps (right) of tungsten disulfide (WS$_2$) on a 12" Si wafer.

Figure 5   HORIBA LabRAM Odyssey Semiconductor. Photoluminescence and Raman imaging on wafers up to 300 mm diameter for 2D materials wafer uniformity assessment and defects inspection.

frequency difference between these two Raman bands directly correlates with the number of layers of the 2D materials.

Both techniques, Raman and Photoluminescence, can be used on the same instrument for wafer imaging, offering insights into the distribution and quality of 2D materials over large areas (Figure 5).

Conclusion

The advent of 2D materials has opened new possibilities for the semiconductor industry. Graphene and TMDs hold immense promise for both FEOL and BEOL applications, paving the way for more efficient, compact, and powerful semiconductor devices. However, significant challenges remain in the synthesis, transfer, and integration of 2D materials. For the compatibility with fabrication rules and successful integration on 300 mm flows, substantial efforts focus on defect reduction and large-scale deposition, emphasizing the need of efficient characterization techniques. HORIBA offers solutions tailored for this industrial research with Raman and PL imaging systems designed for full wafer imaging. Nevertheless, as progress continues, the demand for rapid online metrology is growing and collaborations between semiconductor players and HORIBA have already begun for the development of new in-line metrology systems. Now is the time to

replicate in fab the high quality 2D materials demonstrated in the lab. If we get there, 2D materials are expected to play a pivotal role in shaping the future of semiconductor technology.

* Editorial note: This content is based on HORIBA's investigation at the year of issue unless otherwise stated.

References

[1] *Nature Communications* 13, 1392 (2022)
[2] *Phys. Rev. Lett.* 97, 187401 (2006)
[3] *Nano Lett.* 11, 8, 3190–3196 (2011)
[4] *Nanophotonics* 6, 6, 1219-1237 (2017)
[5] *Nature Nanotechnology* 3, 10–215 (2008)
[6] *Phys. Rev. Lett.* 97, 187401 (2006)
[7] *Photonics* 2(1), 288-307 (2015)
[8] *ACS Nano* 4, 5, 2695–2700 (2010)
[9] *Nanoscale* 14, 6331-6338 (2022)
[10] *npj 2D Mater Appl* 5, 7 (2021)
[11] *Phys. Rev.* B 85, 161403(R) (2012)
[12] *Nano Res.* 7, 561–571 (2014)
[13] *Advanced Optical Materials* 6(1) 1700767 (2018)
[14] *Sci Rep* 3, 1755 (2013)

Marc CHAIGNEAU

Semiconductors Market Manager,
Field leader Metrology,
HORIBA France

Feature Article

Application of HORIBA Instrument in Chemical Mechanical Planarization (CMP) : A Focus on Slurry Analysis and Optimization Strategies

化学機械研磨（CMP）プロセスにおけるHORIBAのアプリケーション：スラリー分析と最適化戦略を中心に

Wan-Hsin HUANG (Ivy)

Kevin SHEN

Optimizing CMP for next-gen devices requires a holistic approach. This involves analyzing physicochemical properties, assessing removal rates, selectivity, planarity, and other relevant factors. In the dynamic landscape of semiconductor technology, analytical tools play a vital role in both assessment and optimization, underscoring their crucial importance in this intricate process. This article provides a summary of measurements conducted on the CMP process in HORIBA's application lab utilizing in-house scientific instruments. It delves into the crucial relationship between CMP slurries and particle size distribution in semiconductor manufacturing. And HORIBA's advanced instruments, such as the CN-300 Partica CENTRIFUGE, provide high-resolution capabilities and possess the ability to measure a diverse range of slurry samples. The document also underscores the role of zeta potential, controlled through sample formulations, and introduces the SZ-100V2 for simultaneous measurement of zeta potential and pH value, aiding in slurry design and quality control. Additionally, spectroscopic ellipsometry are presented as effective tools for determining removal rates and surface change. These contribute to the achievement of precise and robust CMP processes.

次世代デバイス向けのCMPプロセスの最適化には物理化学的特性，研磨レート，選択比，平坦性およびそれらに関連する要素の分析・評価など，広く総合的なアプローチが求められる。半導体技術が急激に進歩するにつれて，複雑なプロセスにおける分析の重要性が高まり，評価や最適化の両面において大きな役割を果たしている。本稿ではHORIBAの分析装置を用いたCMPプロセスに関する分析の概要を示す。まず，CMPスラリーと粒度分布の関係について述べ，多様なスラリーの粒度分布を高分解能で測定できるCN-300 Partica CENTRIFUGEを用いて測定した結果を示す。次に，スラリーの組成によって制御されるゼータ電位測定の重要性およびスラリー設計と品質管理に有用なゼータ電位とpHを同時測定できるSZ-100V2を用いた測定結果を示す。最後に研磨レートや表面状態変化を評価する手法として分光エリプソメトリーについて紹介する。これらの技術は精密でロバストなCMPプロセスの実現に貢献するものと考えている。

Introduction

Chemical Mechanical Planarization (CMP) originated in the 1980s at IBM[1] and has since become a key role in the integrated circuit (IC) manufacturing. CMP is applied in three main areas of IC manufacturing: forming transistors (FEOL), establishing local electrical connections between transistors (MEOL), and creating interconnect structures (BEOL)[1][2]. The FEOL process involves building the device architecture with various CMP steps for layers like SiO_2, Si_3N_4, poly Si stop layers, SiC, SiCN, high-k/metal gate structures, etc. W and Co have attracted attention for local interconnects in the MEOL process. In BEOL, multiple devices are interconnected by sequentially constructing multilevel Cu wires and insulating layers[1][2].

CMP operates through a synergistic interplay of chemical and mechanical interactions to achieve desired removal rates, selectivity, and planarity across different substrate materials in FEOL, MEOL, and BEOL. During the process, the substrate is pressed against a polymeric pad, while a slurry is transported on the pad and undergo three-body (slurry/polishing pad/wafer) interactions (Figure 1). Several factors, including CMP consumables such as slurry, pad, conditioner, and various process conditions like rotating speed and downforce, can influence the polishing performance[2].

To achieve optimized CMP performance tailored for next-generation devices, a comprehensive approach is necessary. This includes understanding the physicochemical properties of CMP slurries, evaluating removal rates, and selectivity, as well as planarity. Given the continuous evolution of semiconductor technology and the heightened demands on CMP performance, analytical tools play a dual role by both assessing and optimizing CMP performance. Therefore, it is evident that having appropriate analytical tools is crucial in this intricate process.

The impact of particle size on CMP performance

CMP slurries are composed of various components, and the formulation is adjusted according to the specific materials being polished. In general, the slurry comprises abrasives, oxidizers, organic compounds such as dispersants and passivation agents, and deionized water. The choice and concentration of these components influence the physicochemical properties of the slurry, impacting the overall CMP performance[2][3].

Particle size is a critical factor in the CMP process, influencing factors like abrasion efficiency and material removal rates. While past literature[3]-[5] extensively delves into the effects of particle size on CMP processes,

comprehending its impact on CMP performance poses challenges, given the diverse influences of particle manufacturing processes, raw materials, and morphology[3].

Numerous research continues to seek a clearer mechanism describing the influence of particle size on CMP. As D. Tamboli et al. mentioned, when removal rates per abrasive particle are plotted against particle size, a clearer trend emerges, indicating an increase in removal efficiency per particle with size[3]. The contact area and size of particles play a crucial role in CMP processes, with larger particles exhibiting higher removal rates when the slurry's particle count is fixed[3][4]. However, spiking coarser particles in the slurry can lead to separation between the wafer and the pad, reducing pressure on smaller abrasive particles and resulting in decreased interaction with the substrate[5]. Observations from literature[5] also indicate that contamination by larger particles not only affect removal rate but also cause surface defect, such as scratching.

Advantaging of utilizing HORIBA Partica CENTRIFUGE CN-300 for CMP slurry analysis

Achieving optimal particle size distribution is crucial for ensuring uniform polishing and maintaining desired planarity in semiconductor manufacturing. Additionally, controlling particle size contributes to the prevention of scratching or damage to the polished surfaces, further emphasizing its pivotal role in the CMP process. Therefore, understanding and managing particle size within CMP slurries become essential for achieving precision and reliability in semiconductor fabrication. HORIBA offers multiple instruments for analyzing the wide range of particle size of slurry (Figure 2), employing various analytical techniques such as laser diffraction (Mie Theory), dynamic light scattering, and nanoparticle tracking analysis (NTA)[6]. And in response to the increasing demand for high-resolution CMP Slurry analysis in semiconductor factories, HORIBA has
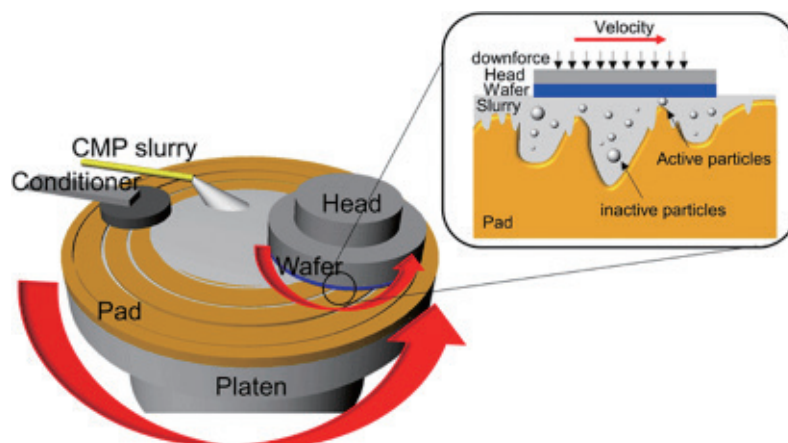

Figure 1   Three-body interactions in CMP process[2].

introduced the innovative Partica CENTRIFUGE CN-300. The CN-300 utilizes centrifugal sedimentation technology, with its primary advantage being high resolution. Furthermore, the CN-300 centrifuge presents several additional advantages, with a key focus on its two distinctive modes, the line-start and homogeneous mode, that significantly broaden the range of sample types and concentrations that can be accurately measured.

The Line-start mode enables the classification of particles based on their size, delivering precise and high-resolution results across a diverse range of samples in a single analysis. To evaluate the resolution of the Line-start mode method, a composite sample containing fourteen different sizes of monodispersed polystyrene latex (PSL), ranging from 100 nm to 30 μm[7], was utilized. As illustrated in **Figure 3**, a Particle Size Distribution (PSD) featuring fourteen distinct peaks, classified by centrifugal force, was observed. Significantly, these peaks closely aligned with the nominal

values of the particle size standards in terms of size positions. The assessment of the mixed PSL sample has confirmed that CN-300 centrifugal sedimentation method demonstrates exceptional resolution and high accuracy capabilities.

The Homogeneous mode significantly broadens the CN-300's capabilities by facilitating the measurement of particle concentrations across a wider range. As shown in **Figure 4**, the Homogeneous mode enables the measurement of particle size across a broad concentration range, spanning from the undiluted sample to a dilution of up to 200 times. This implies that the CN-300 Homogeneous mode is applicable for measuring not even Point-of-Use (POU) slurry but also abrasive raw materials. Additionally, this mode proves highly effective for samples that react with Gradient Solution, highlighting the instrument's versatility in handling a diverse array of challenging samples. Such capabilities confer significant advantages in addressing the
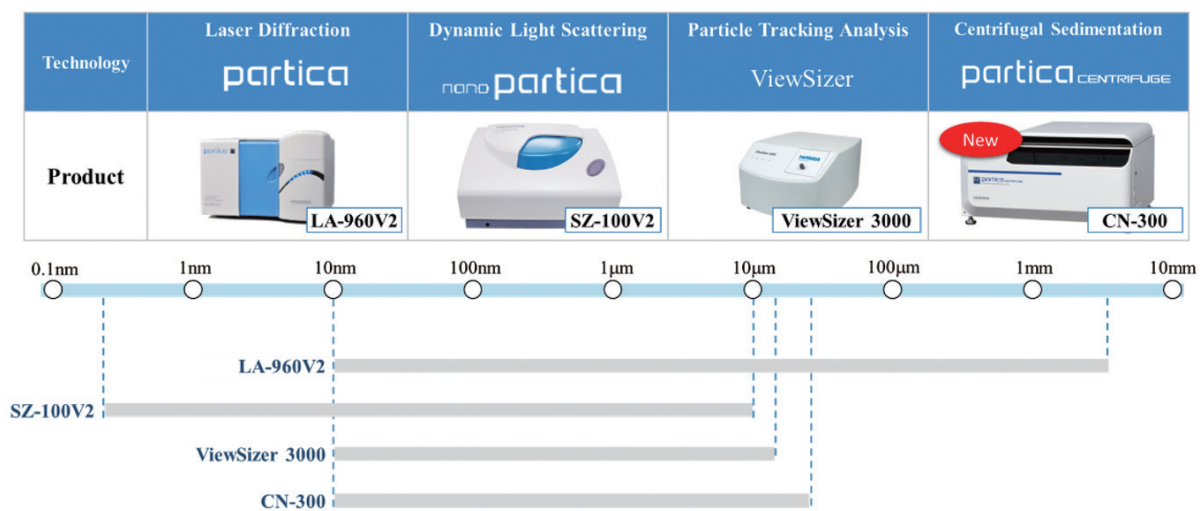

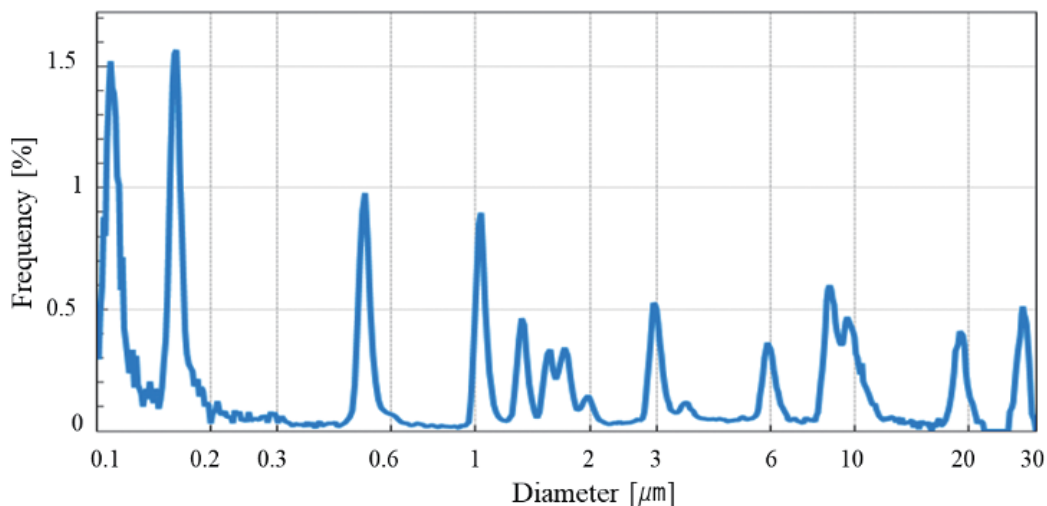Figure 2   HORIBA particle size characterization techniques.

Figure 3   Measurement of mixed samples with different particle sizes with high resolution[7].

progressively complex CMP slurry formulations observed in recent years.

The influence of zeta potential on CMP slurry formulations

The impact of zeta potential on CMP is a crucial area of research, particularly concerning the interactions between particles and the substrate. The zeta Potential of particles can be further controlled through adjustments in sample formulations, allowing for precise regulation of the removal rate.

According to literature, key factors to increase friction energy in CMP processes include the number of active particles, the contact area of each particle, and the friction coefficient related to particle shape, surface morphology, and material type[4]. Increasing the number of active particles can be achieved not only by elevating particle concentration but also by facilitating particle adhesion onto the substrate surface. The constant adsorption and desorption of particles onto the substrate surface in CMP slurries distribution to the platen underscore the importance of inducing attractive forces between particles and the substrate by controlling the zeta potential of each material. The force acting between particles and the substrate in a liquid can be calculated based on the sum of electrostatic force due to electrical double layers and Van der Waals force, as per the DLVO theory. Furthermore, zeta potential adjustment can be achieved through various means, such as pH modification and the introduction of additives[8][9].

The monitoring of zeta potential is critical in both the design of CMP slurry formulations and the quality control of CMP slurry, as it plays a vital role in influencing various aspects of CMP processes. These include the efficiency of the formulation in enhancing removal rates, selectivity, and wafer planarity. HORIBA addresses this need by offering a solution that allows simultaneous measurement

of the zeta potential and pH value of abrasives[10][11]. This instrument SZ-100V2 provides users with the capability to understand the zeta potential of abrasives under different pH conditions or the synergistic effects between abrasives and additives. Such insights are particularly valuable for scientists involved in designing slurry formulations and for quality control purposes, ensuring the robustness of the manufacturing process.

Additionally, SZ-100V2 offers the reliable measurement of ultra-diluted samples, enabling the acquisition of accurate zeta potential data. This capability not only ensures precision in measurements but also supports a Post CMP cleaner design approach by facilitating the exploration of interactions between abrasives and cleaners. For example, simulating the initial stages of the Post CMP process involves immersing ultra-diluted abrasives into cleaners. As shown in **Figure 5**, the zeta potential can be accurately measured even when the sample concentration is as low as 0.05wt%. This capability allows for the measurement of ultra-diluted abrasives in cleaners. Research efforts can then ascertain whether there is a repulsive or attractive force between the slurry abrasive and the wafer. The data obtained provides valuable insights into the formulation design direction, facilitating the pursuit of more challenging targets.

The Role of HORIBA UVISEL Plus Phase Modulated Ellipsometry in Thin Film Characterization

Spectroscopic ellipsometry is a non-destructive, non-contact, and non-invasive optical technique which is based on the change in the polarization state of light as it is reflected obliquely from a thin film sample. Ellipsometry uses a model-based approach to determine thin film, interface, and surface roughness thicknesses, as well as optical properties for thin films ranging in thickness from a few Å to several tens of microns. Therefore, it proves to
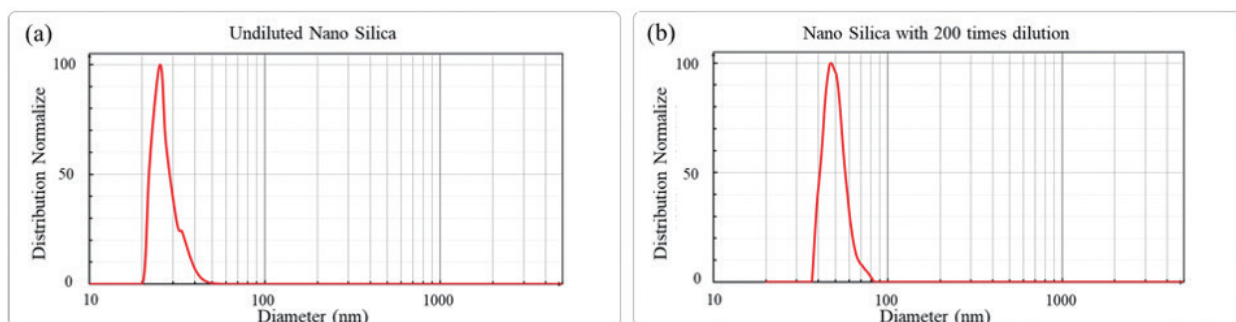

Figure 4   Using CN-300 Homogeneous mode to determine the particle size for both (a) the undiluted sample and (b) the sample diluted 200 times.
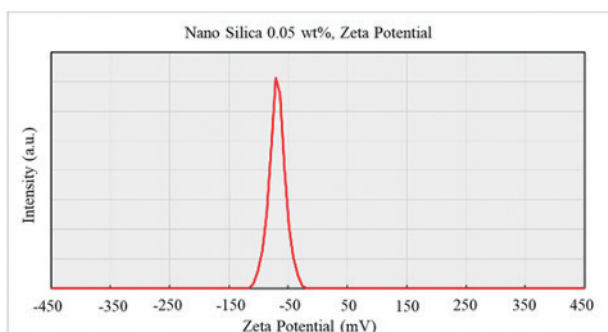
Figure 5　The zeta potential can be measured even when the sample concentration is as low as 0.05wt%.

be a valuable technique in the field of CMP as it facilitates the determination of removal rates for specific wafers. To gauge these removal rates accurately, it becomes imperative to measure the thickness of wafers both before and after CMP processes. Employing multiple thickness measurements enable verification of within-wafer uniformity.

And the HORIBA UVISEL Plus with phase-modulated ellipsometer achieves higher sensitivity and accuracy when compared to conventional ellipsometers using rotating elements. It enables the detection of single-angstrom variations or interfaces not observable by other ellipsometers. By incorporating a thin film model, users gain the capability to discern thickness as well as optical constant changes at specific sites. This functionality enables formulation determination and optimization of process parameters, allowing for the detection of even slight differences in surface conditions. For instance, in cases where certain components in the slurry exhibit strong absorption behaviors on a particular type of wafer, UVISEL Plus ellipsometry reveals spectral differences between the wafer before and after treatment. By developing a fitting model, researchers can delve into the study of absorption behaviors[12]. This capability offers users a comprehensive understanding of the intricacies of the surface by optical constant change, facilitating informed decision-making in the context of CMP processes.

Conclusion

In summary, this document highlights diverse HORIBA analytical tools applicable to the CMP process. The Partica CENTRIFUGE CN-300, with its Line-start and Homogeneous modes, offers high-resolution slurry analysis, addressing the complexity of modern CMP slurry formulations. The importance of maintaining particle size within specified ranges is underscored. The impact of zeta potential on CMP is discussed, and the SZ-100V2 is introduced as a valuable solution for simultaneous measurement of zeta potential and pH in abrasives. This instrument's capability to handle ultra-diluted

samples supports precision measurements and aids in the design of Post-CMP cleaner approaches. Additionally, the document explores the role of spectroscopic ellipsometry in evaluating removal rates, providing a comprehensive understanding of CMP processes. As semiconductor technology progresses, these advanced analytical tools from HORIBA contribute significantly to achieving precision, reliability, and efficiency in CMP applications.

* Editorial note: This content is based on HORIBA's investigation at the year of issue unless otherwise stated.

References

[1]   J. Seo, U. Paik, Preparation and characterization of slurry for chemical mechanical planarization (CMP), *Advances in Chemical Mechanical Planarization (CMP)*, 2016, Pages 273-298, https://doi.org/10.1016/B978-0-08-100165-3.00011-5

[2]   Seo, J., A Review on Chemical and Mechanical Phenomena at the Wafer Interface during Chemical Mechanical Planarization, *Journal of Materials Research*, Vol.36, 235 (2021). DOI: 10.1557/s43578-020-00060-x

[3]   D. Tamboli *et al*, Novel Interpretations of CMP Removal Rate Dependencies on Slurry Particle Size and Concentration, *Electrochem. Solid-State Lett.*, Vol.7, F62 (2004). DOI 10.1149/1.1795033

[4]   Hitoshi Morinaga and Kazusei Tamai, Challenges and Mechanisms of CMP Slurries for 32nm and Beyond, *ECS Trans*. Vol.34, 591 (2011). DOI 10.1149/1.3567643

[5]   G. B. Basim et al, Effect of Particle Size of Chemical Mechanical Polishing Slurries for Enhanced Polishing with Minimal Defects, *J. Electrochem*. Soc., Vol.147, 3523 (2000). DOI 10.1149/1.1393931

[6]   HORIBA AN179, CMP Slurry Measurement using Laser Diffraction.

[7]   HORIBA ADS164, A Mixed Sample of Polystyrene Latex Standards.

[8]   Kazusei Tamai et al, Effect of Particle-Substrate Interaction on the Polishing Rate, ICPT (2009).

[9]   Adam Manzonie et al, CMP Slurry Optimization for Advanced Nodes, Solid state technology (2016).

[10]   HORIBA AN195, Isoelectric Point Determination.

[11]   HORIBA AN206, Using SZ-100Z Autotitrator for Isoelectric Point

[12]   Ebara Technical Papers No. 251, Application of In-situ Observation Technology in CMP Process for Upgrading the Process Integrity. Application of In-situ Observation Technologies in CMP Process for Upgrading the Process Integrity | EBARA CORPORATION

Wan-Hsin HUANG (Ivy)

Sales Engineer,
Sales Engineering Dept.,
HORIBA Taiwan, Inc.

Kevin SHEN

Application Engineer,
Application Engineering Dept.,
HORIBA Taiwan, Inc.

Product Introduction

レティクル／マスク異物検査装置PD Xpadionの紹介
～多種多様な顧客要望に対応可能なプラットフォームを構築～
Introduction of Reticle/Mask Particle Detection Integrated System

出島 悠貴
DEJIMA Yutaka

染谷 翔太
SOMEYA Shota

PDは半導体製造プロセスの露光工程で使用されるレティクル／マスク上の異物を検査する装置である。これまで市場やアプリケーション毎に開発していたPDシリーズを一つのプラットフォームに統合し，2021年に新製品となるPD Xpadionを開発した。高いカスタマイズ性を持ち，多種多様な半導体市場の要求に応えられる製品となっている。本記事ではPDの測定原理をはじめ，新製品PD Xpadionの特徴や新機能を紹介していく。

PD is an instrument to detect particles on Reticle/Mask used in the semiconductor exposure process. A new product PD Xpadion, which is an integrated PD series to one platform, was released in 2011. It is designed for easy customization and to meet a wide variety of requests in the semiconductor market. This article will introduce features and new functions of PD Xpadion.

はじめに

PDは主に半導体工場における露光工程のプロセス品質管理や，マスクショップのマスク製作における中間検査・出荷前検査などの品質管理に使用されている。また近年では，最先端のEUV露光における生産プロセスの品質管理にも採用が始まっており，これまで世界中で370台以上の稼働実績を持っている。

半導体市場における分析装置への要求は工場自動化や各種SEMI規格対応，パターン微細化に伴う高集積化・高機能化実現のための技術進展などを背景に変化し続けている。要求内容は年々多様化・複雑化してきており，従来のPDシリーズのプラットフォームでは対応が困難になってきた。

堀場製作所はこれまで40年近くレティクル／マスク（以下，レティクル）市場に異物検査装置を供給し続けることで，顧客が求める分析装置に対する要求と自動検査装置の開発設計ノウハウを蓄積してきた（**Figure 1**）。

市場要求に迅速に対応するため，それらの成果を整理し，これまでのPDシリーズを一つのプラットフォームに統合したのが新製品PD Xpadionである。

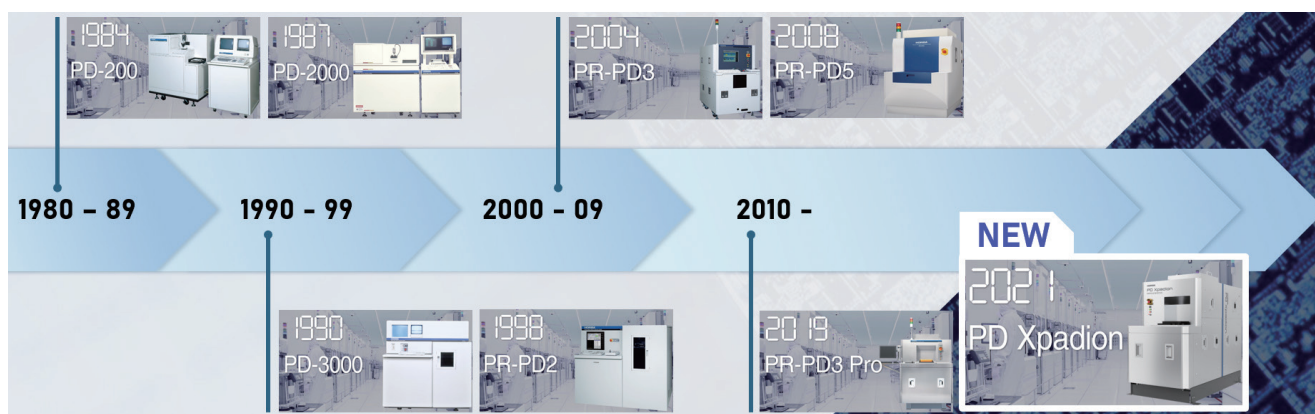### PDの測定原理

PDの異物検出の基本的な原理はレーザ光をレティクル上に照射し，散乱した光を検出する方式となる。

Figure 1   History of PD series.

ガルバノスキャナを用いてレーザ光を走査し，同時にステージを移動させることでレティクル全面を測定することができる。また，検出用の光学系を測定対象の上下に配置することで，パターン面，ペリクル面，ガラス面の3面の高速検査を可能にしている（**Figure 2**）。

異物検出用の光学系に関しては，パターン付きレティクル用途の標準光学系とマルチ検出機光学系，ブランクスマスク用途の高感度検出光学系を準備しており，対応するアプリケーションに応じて選択する（**Table 1**）。

標準光学系

パターン付きレティクルの検査用に設計した検出光学系では最高0.35 µmまでの検出感度に対応している。微細なパターンから発生する回折散乱光を，誤って異物と判定してしまうことを誤検出と呼んでおり，パターン付きレティクル検査では，この誤検出を回避することが重要となる。この光学系では検出器の光学配置と計測光の偏光成分を管理することで，異物依存の散乱光の感度を保ちながら誤検出を低減している。

マルチ検出器光学系

標準光学系では円形パターンのように，特定の向きに強い回折散乱光を発するパターンからの誤検出が課題となっていた。その課題を解決したのがマルチ検出器光学系である。装置内の特定の位置にもう一対の検出器を配置することで，いずれかの検出器が回折散乱光を回避することができる。これまで不得意であったパワー半導体の配線パターンや表面配線用のホールパターンなどのレティクルに対して，大幅に誤検出を低減できるようになった。

高感度検出光学系

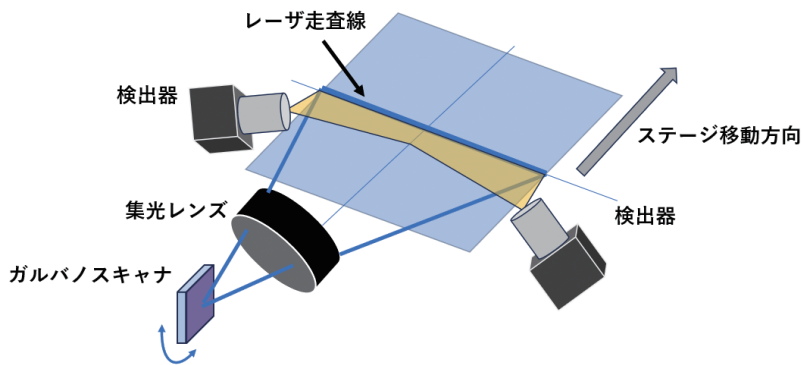ブランクスマスクはその表面にパターンが形成されていないため，パターン付きレティクルからの回折散乱光を回避する必要がない。異物から発生する散乱光を積極的に検出する全光集光型の光学系を採用することで，異物サイズ0.1 µmまでの高感度検査を実現している。

Figure 2　Structure of optical system.

Table 1　Optical system option list.

	標準光学系	マルチ検出器光学系	高感度検出光学系
光学配置			
特　徴	－	誤検出低減	高感度
検査対象	パターン付きレティクル		ブランクスマスク

新製品PD Xpadionの特徴

PD Xpadionは組み合わせによる柔軟なカスタマイズ性と，高いユーザビリティに特徴を持つ製品である。以下にそれぞれの特徴について詳細を述べる。

特徴1：柔軟なカスタマイズ性

PDはレティクルメーカの出荷検査，半導体デバイスメーカのルーティン検査など様々な用途で使用されている。顧客の使用用途に合わせた検出感度やレティクルサイズなど，アプリケーションに応じて装置構成を変更している。従来のPDシリーズでは，製品型式におけるカスタマイズの対応範囲が制約されていたが，PD Xpadionではオプションをユニットとして組み合わせることで対応範囲が広く，迅速なカスタマイズ対応を実現している。

カスタマイズの代表的な例がサンプルを設置するロードポートである。露光工程において半導体回路製造の原板となるレティクルは，通常異物汚染を防ぐため常に専用のケースまたはポッドに入れて管理されており，ＰＤ Xpadionでは国内外の露光装置メーカ毎のケースに対応している。運用に応じて，複数のケースを設置できる多段スロットからの搬送や，OHT（Overhead Hoist Transport：搬送物を吊り下げた状態で保持し，天井に設置された軌道レールを走行する自動搬送装置）との連携など様々な工場運用に対応できるオプションを用意している。

異物検出用の光学系は先に説明した通りパターン付きレティクルやブランクスマスクなど用途やアプリケーションに応じて選択する。

他にもバーコードやRFIDなどのコード読み取り機能や，9インチレティクル対応など多くのオプションを備えており，特定の組み合わせに限定されない，顧客の運用に合わせた幅広いカスタマイズを実現する。

特徴2：高いユーザビリティ

PD Xpadionでは顧客の業務フロー改善に有用な多くの機能を実現している。その中でも改善効果が大きい異物画像のオートサイズ機能と，異物-欠陥のランク分類シミュレーション機能について説明する。

- 異物画像のオートサイズ機能
  本機能はレーザ散乱光で検出した異物を顕微鏡観察し，画像処理にて自動的に異物のサイズを測定する機能である。レーザ散乱による異物検出原理では異物が発光する領域は分かるものの，その範囲は異物形状や材質等に大きく影響し，異物の実サイズとは一致しないことがある。生産工程における異物管理は検出異物の実サイズを用いて合否判定する運用が多く，特に大きな異物に対してオ

ペレータは手動で検出異物を観察し対応を判断する必要があった。本機能を用いて検査から顕微鏡観察，サイズ計測の流れを自動化することにより，オペレータの業務負担を大きく軽減することができる。

- 異物−欠陥のランク分類シミュレーション機能
  PDでは検出異物が発光する領域の大きさに応じてA＜B＜Cの3種類にランク分けし，ランク毎の検出異物個数を用いて合否判定を行うことができる（**Figure 3**）。例えば最も大きいCランクの異物が5個以上含まれていればNGとするなど顧客の運用に応じた判定条件を設定できる。先述の通り，レーザ散乱による検出異物の発光範囲は異物の形状や材質により変動するため，従来機では閾値を変更しながら実測定を繰り返し，パラメータを最適化させる必要があった。複雑な条件の場合は半日以上かかる作業であった。PD Xpadionでは結果データからランク閾値変更後の状態をシミュレートする機能を用いてこの作業を効率化している。一度の測定を行うだけでレシピ作成を完了することができる（**Figure 4**）。
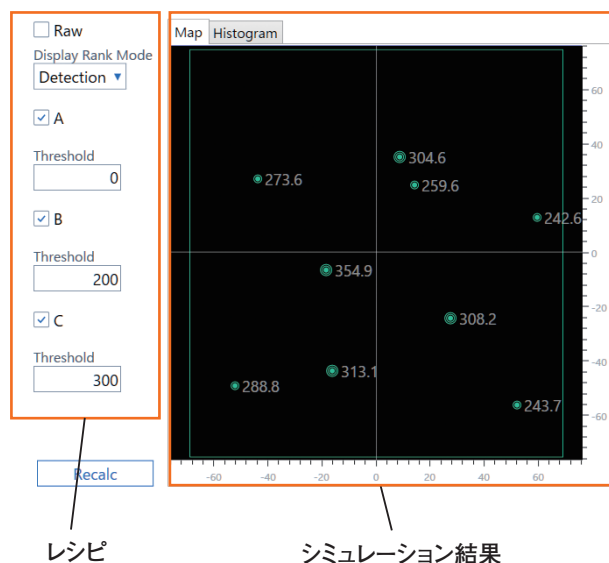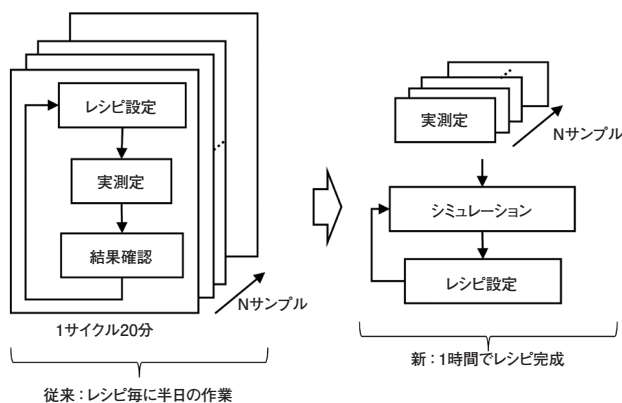

Figure 3   Software operation view.

Figure 4   Comparison of optimization for recipe.

PD Xpadion EXシステムの導入

異物検査に特化したPDとレティクル／マスク搬送ローダーを統合したシステム製品PD Xpadion EXを2024年に新たに開発した。搬送ローダーと接続し，マルチロードポートや別ユニットとの連携を可能とすることでカスタマイズの幅を広げ，工場の運用に応じた最適な仕様を選択することで業務フローの改善に貢献する。

マルチロードポート

PD Xpadion EXでは複数のロードポートを様々な種類の組み合わせで拡張することができる。工場内で複数の異なるケース種を運用している場合，従来のシングルポートの装置では特定のケースに移し替えPDにセットする必要があった。マルチロードポートでは運用されている複数のケース種に対応したロードポートを組合せることで，移し替え作業時のレティクル汚染リスクを低減する。
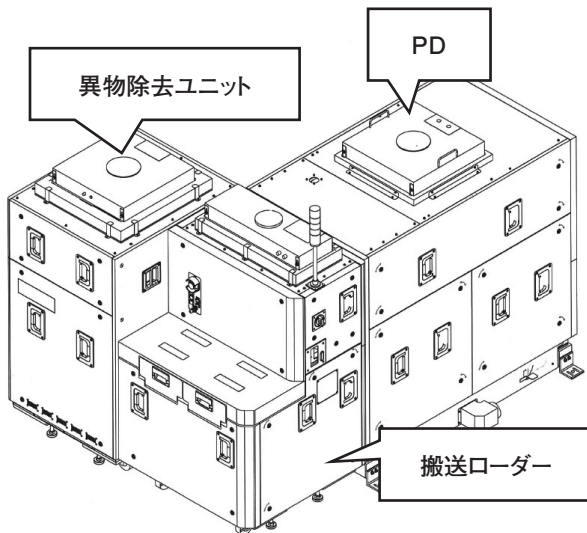

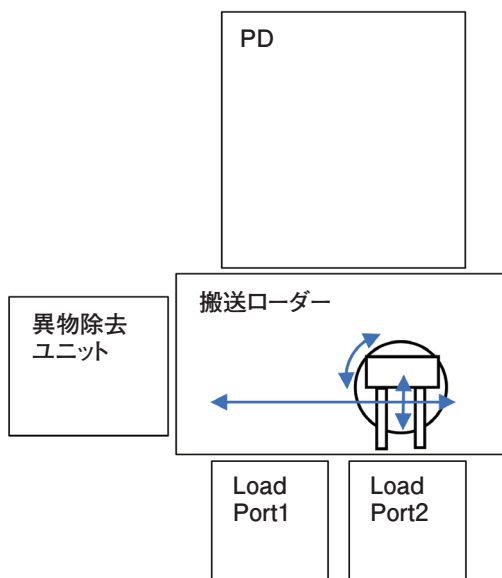Figure 5　External view of the instrument.

Figure 6　Structure of unit connection.

また，PDの異物検出結果がNG（特定の個数以上の異物を検出）となったレティクルのみを特定のポートに分別するなど，結果に応じてアンロードするロードポートを変更することもできる。

ユニット連携

PD以外のユニットを接続することで異物検出に「＋α」となる機能を付与する。その実例の一つが異物除去ユニットである。接続することでPDで検出したレティクルのペリクル面／ガラス面に付着した異物を自動で除去することが可能となる。

上下面からレティクルを挟んだクリーナーヘッドから吹き出すクリーンドライエアーにより異物を対象表面から離脱させ，さらに近傍で吸引することで効果的にレティクルのクリーニングを行う。異物除去作業を自動化することで作業を効率化するだけでなく，従来の人手でのエアブローでおこる人為的ミスでのペリクル破損や，ケースからのレティクル出し入れによる異物再付着といった課題も解決する。

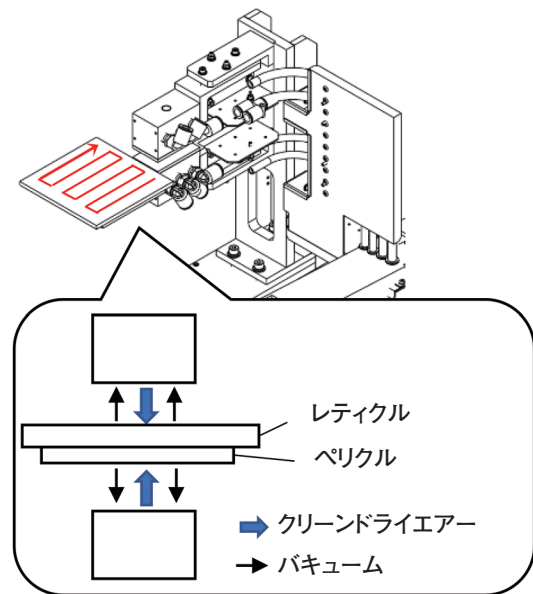ガラス面に5 µm，ペリクル面に20 µmのガラスビーズを付着させた除去性能検査では90%以上の除去性能を確認している。
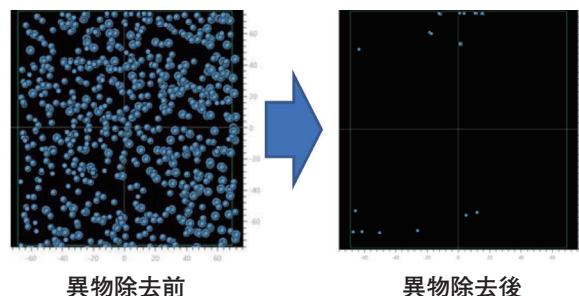

Figure 7　Mechanism to remove particles.

Figure 8　Particle removing result.

おわりに

今回紹介したPD Xpadionは，PDシリーズが長年培ってきたノウハウを一つのプラットフォームに集約させ完成した製品となる。過去に対応してきたカスタマイズを効率的にシステム設計に組み込むことで，多数の有用な機能を搭載した。また，これまでの検出課題であった誤検出も，新たな光学系を採用したことにより大幅に低減することができた。

PD Xpadion EXでは搬送ローダーを中心としたシステムを構築し，顧客に新たな付加価値を提供する。今後はHORIBAグループが所有するラマン分光やエリプソメータ，蛍光X線分析など各種分析装置を接続することで，さらなるアプリケーションの発展を目指していく。

対応できるアプリケーションの幅は広く，"新しいプラットフォーム"と"長年培ってきたノウハウ"を用いてお客様の課題を共に解決していきたい。
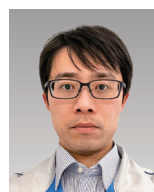
＊編集局注：本内容は特段の記載がない限り，本誌発行年時点での自社調査に基づいて記載しています。

出島 悠貴
DEJIMA Yutaka
株式会社堀場製作所
先端材料・半導体センター　半導体ソリューション部
PD-EX Project チーム
PD-EX Project Team
Semiconductor Solution Dept.
Materials & Semiconductor Center
HORIBA, Ltd.

染谷 翔太
SOMEYA Shota
株式会社堀場製作所
先端材料・半導体センター　半導体ソリューション部
PD Application チーム
PD Application Team
Semiconductor Solution Dept.
Materials & Semiconductor Center
HORIBA, Ltd.

Product Information

新製品紹介

IRLAM技術を用いた半導体エッチングプロセス向け
レーザーガス分析計の開発
Development of a Laser Gas Analyzer for Semiconductor Etching Process using IRLAM Technology

坂口 有平
SAKAGUCHI Yuhei

波田 美耶子
HADA Miyako

半導体製造プロセスでは，ドライエッチング技術を用いてnmオーダーの微細形状の加工が行われている。最先端のエッチングプロセスにおいてプロセス制御を精密に行うため，プロセスの状態をリアルタイムにセンシングする技術は重要である。HORIBAでは量子カスケードレーザー（QCL）を用いた赤外レーザー吸収変調法（IRLAM）を開発しており，高感度で高速に測定できる特徴を生かして半導体エッチングプロセスに適用可能なガス分析計の開発を行った。本稿では分析計の構成や実際のエッチングプロセスで評価した事例について紹介する。

In the semiconductor manufacturing process, dry etching technology is utilized for making nm-order microstructures. Sensing technologies for real-time process monitoring is important for precise process control in advanced etching processes. HORIBA has developed an infrared laser absorption modulation (IRLAM) using a quantum cascade laser (QCL). Taking advantage of IRLAM's high sensitivity and fast response performance, we have developed a gas analyzer which optimized for etching processes. In this paper, we introduce the configuration of the analyzer and evaluation results of actual etching process.

はじめに

近年の半導体デバイスは高集積化し，3 次元的で複雑な微細構造をとるように発展してきており[1]，加工時に制御しなければならない寸法精度も厳しいものとなってきている。最小加工寸法が数nm以下の回路を形成するためには，原子にすると数個や数十個のレベルでの加工の制御が必要とされており，トランジスタのゲート電極やコンタクトホールの形成などにおいては，nmオーダーの微細形状を加工できるドライエッチング技術が用いられている[2]。

エッチングプロセス中の加工状態を管理しリアルタイムに制御を行うため，プラズマエッチングの量産設備では発光分光分析が実用化されている。HORIBAはプラズマ発光分光分析技術を保有しており，その技術を用いた発光分光装置は生産現場だけでなくプロセス開発から生産管理までの様々な段階で幅広く活用されている[3]。一方で，最先端のエッチングプロセスの中には，開口率やアスペクト比などの条件によっては十分な信号が得られないケースや，ケミカルドライエッチングのようにそもそもエッチングにプラズマ源を使用しないため発光分光が適用できないケースもでてきており，そのような先進的なプロセスにも対応できるセンシング技術が求められている。

HORIBAの持つ分析技術の一つである赤外分光法は古くから自動車，科学，環境，半導体などの様々な産業分野に適用されてきた。フーリエ変換赤外分光法（FTIR）は，光源として高温にした発熱体を用い，そこから放射される幅広い波長帯の赤外光を，干渉計を通して干渉波として取り出し，フーリエ変換することで発光波長全域にわたるスペクトルを得る分析法である。また，非分散型赤外分光法(NDIR)と呼ばれる手法は，光源からの一部の波長の光を目的に合わせて光学フィルタで取り出し，その光の変化を測定する手法であり，FTIRよりシンプルな構成で小型の分析計を実現できる[4]。

FTIRやNDIRの技術を用いたガス分析計は半世紀以上の歴史があり，プロセス監視・制御用として確立された技術であるが，半導体プロセスのアプリケーションに適用するには，検出感度や応答速度の点でさらなる技術的な挑戦が必要である。HORIBAで新たに開発したガス分析手法である赤外レーザー吸収変調法（IRLAM）は，量子カスケードレーザー（QCL）から発生する光をガスセルで多重反射させ，検出した信号にHORIBA独自の演算アルゴリズムを組み合わせることで，高い検出感度で高速測定が可能な分析技術である。我々はこのIRLAMの技術を用いて半導体のエッチングプロセスのアプリケーションに最適なガス分析

計の開発を進めてきた。本稿では，IRLAMの原理と半導体プロセス向けに開発した分析計の詳細について述べた後，実際のエッチングプロセスでの評価結果から得られた本分析計の有効性について述べる。

IRLAMの原理と構成

ガス分子はそれぞれ構造に応じた固有のエネルギー準位を持ち，光と相互作用した際に特定の波長の光を吸収する。光が物質によって吸収される際の入射光と透過光の関係はランバート・ベールの法則として知られている。

$$A = -\log \frac{I}{I_0} = \varepsilon C l$$

入射光をI_0，透過光の光の強さをIとすると，一定の厚さlの試料の中を光が通過する際に光の強度は対数的に減少し，吸光度Aは，濃度Cと，そのガスの持つ吸光係数εに比例する。IRLAMを始め，NDIRやFTIRにおいても吸収分光による定量は，この原理に基づいている。

IRLAMでは光源として中赤外領域の光を発振できるQCLを使用している。QCLは半導体薄膜を積層させた構造を持ち，それにより形成される半導体量子井戸のサブバンド間の光学遷移を利用して中赤外波長のレーザー光を発振，放射する。HORIBAでは，このQCLを自社で設計・製造する技術を確立しており，測定対象ガスに応じた最適なQCLを準備することが可能である。

QCLから放射される光は直進性のよいレーザー光であり，この光をガスセルに入射させ，ガスセル内に配置された2枚のミラー間で光を多重反射させることにより光路長を長くとることが可能である。ランバート・ベールの法則で示されるように，試料中を光が通過する距離が長いほど大きな吸光度が得られるため測定感度を向上することができる。HORIBAのIRLAMではガスセルにヘリオットセルと言われる2枚の凹面ミラーを用いる構成を採用しており，光学設計を工夫することでミラー形状を細長形状とし光路長を確保した上でセル内容積の低減を図れるようにしている。この設計によって感度の向上とガス置換時間の低減が可能となり，サイズの点でも小型化が実現できている。

IRLAMでは独自の演算アルゴリズムとして，測定したガスの吸収信号から「特徴量」を抽出する手法を用いている。具体的な内容は別の文献[5]にて説明されているため，ここでは詳細には触れないが，この手法により干渉ガスの影響やQCLの発振波長のドリフトの影響，圧力や共存ガスによるスペクトルブロードニングの影響などを補正することが可能となり，また演算は組込み型のマイクロコンピュータで実行できるため，コンパクトな装置構成にすることができる。

Figure 1   Photograph of the laser gas analyzer, LG-100.

IRLAMを用いた半導体向けレーザーガス分析計

Figure 1に今回開発したレーザーガス分析計LG-100シリーズの外観を示す。本製品はセンサユニットと通信変換ボックスで構成され，センサユニットの外形は440(W)x170(D)x150(H) mm，通信変換ボックスは80(W)x92(D)x87(H) mmである。測定成分としては半導体のエッチングプロセスにおける主要な副生成物であるSiF_4をターゲットとしている。

分析計の構造図と光学系の配置図をFigure 2に示す。センサユニットは半導体製造装置の配管への取付の容易さを考慮し，ガスの入口と出口はNW40のフランジとする設計とした。ガスセルは180℃に温調可能であり，内蔵されているヒーターの配置を最適に設計することでコールドスポットになりがちな光学窓の部分も含めて接ガス部分の温度分布が均一になるようにしている。レーザー光源とガスセル，検出器間の光学系についても，使用するミラーの枚数をなるべく減らしたコンパクトな構造とした。

ガスの測定においては，配管内の圧力の情報も重要なパラメータとなる。半導体製造装置における圧力測定には静電容量型の真空計が広く使われており，HORIBAでも自社で静電容量型の真空計を開発している[6]。HORIBAの真空計(VGシリーズ)は1 Torrから1000 Torrまでのレンジで最高200℃の温度に対応可能な仕様の製品をラインナップしている。エッチングプロセス中のチャンバー圧力は数mTorrであり，排気ラインの圧力も1 Torr以下の真空となっていることが多い。本分析計では，真空計を自社開発している強みを生かし，ガスセル内に組込めるよう設計した真空計が内蔵されている。

通信仕様については，最近の半導体製造装置では通信のリアルタイム性からEtherCAT®の採用が進んでいるため，本分析計もEtherCAT®通信に対応可能な仕様となっている。センサユニットと接続される通信変換ボックスはEtherCAT®通信及びアナログ入出力のインターフェースを持っており，半導体製造装置へ組み込みしやすくなっている。

性能評価

Table 1 に分析計の主な仕様を示す。分析計の出力はSiF_4の分圧値となり，そのフルスケールは10 mTorrである。繰り返し性・直線性・ゼロノイズ(3σ)は±1%F.S.以下の仕様である。
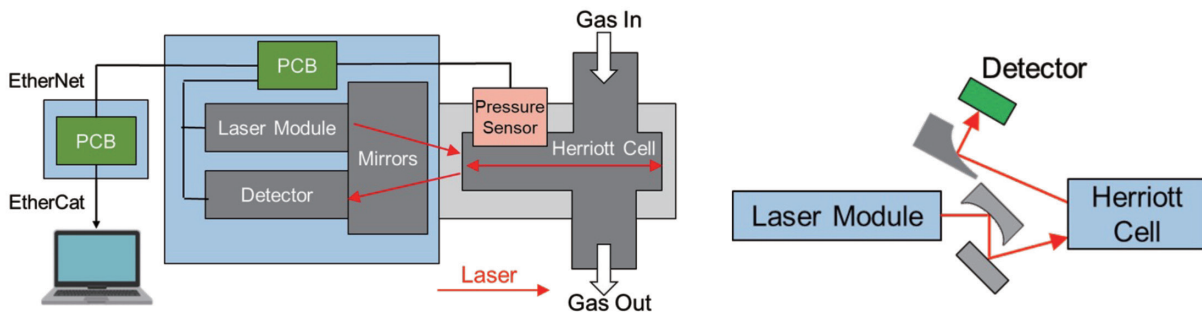
Figure 2　Conceptual diagram of the gas analysis procedure in LG-100.

Table 1　Typical specifications of LG-100.

原理	赤外レーザー吸収変調法
セル温調温度	180℃
測定ガス及びフルスケール	測定ガス：SiF_4　　フルスケール：10 mTorr
繰返し性	±1%F.S.
直線性	±1%F.S.
ゼロノイズ	1%F.S.以下（3σ）
ゼロドリフト	±1%F.S./8 h
周囲温度範囲	20 to 50℃
圧力センサ測定レンジ	1 Torr
圧力センサ精度	±1%F.S
暖機時間	120 min.以上
リークレート	1×10^{-6} Pa・m^3/s(He) 以下
耐圧	200 kPa（A）

Figure 3は既知濃度のSiF$_4$ガスをN$_2$で希釈することで20%F.S.刻みで分圧を変え，また0%F.S.と100%F.S.を繰り返して測定した結果を示す。Figure 4にはゼロ点のノイズ及び8時間の安定性の評価結果を示す。繰り返し性・直線性は±1%F.S.以内であり，ノイズについても約0.2%F.S.と良好なS/N比で安定した測定ができることが確認できた。

エッチングアプリケーションへの適用例

今回開発したガス分析計を実際の半導体エッチング装置に取り付け，プロセスでの評価を実施した。Figure 5に実験構成を示す。誘電結合プラズマ型のエッチング装置の排気側に設置されているターボ分子ポンプとドライポンプの間の配管に分析計を取付けて排ガス測定を行った。サンプルウエハには4インチのSiウエハ上にSiO$_2$を成膜したものを用い，エッチング時に発生するSiF$_4$の変化を測定した。サンプルはFigure 6に示すように開口率とマスクパターンが異なる3つのサンプルを準備した。サンプル(a)はSiO$_2$面上にマスクがされていない開口率100%のサンプルであり，サンプル(b), (c)は開口率5%になるようにマスクがされたサンプルである。(b), (c)は開口率が同じであるが，マスクパターンが異なっており，(b)はウエハ中心に四角形に開口部が配置され，(c)は直径上に長方形に配置されている。今回の試験におけるエッチング条件は，チャンバー圧力 1.0 Pa, C$_4$F$_8$ 30 sccm*, O$_2$ 20 sccm*, ICPパワーは500 W, バイアスは30 Wを基準条件として試験を実施した。

*sccm: standard cubic centimeter per minute

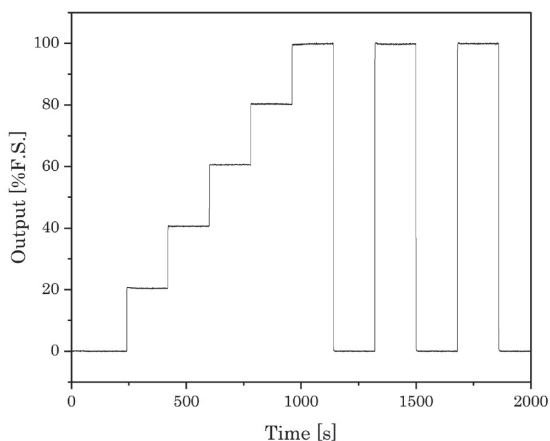エッチング時に印加するバイアスパワーを30 Wから180 Wの間で変化させ，Figure 6(a)のサンプルを1分間エッチン

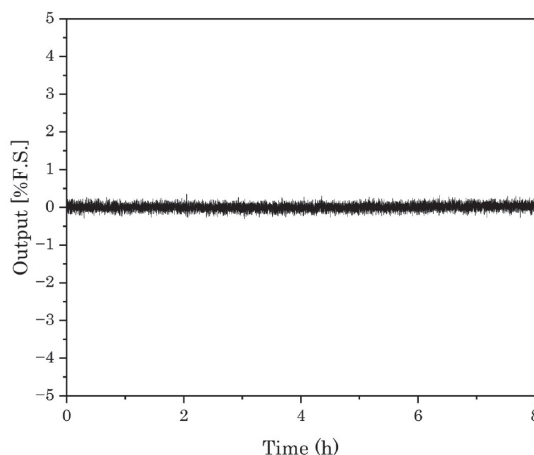Figure 3　Measurement result of SiF$_4$ gas.
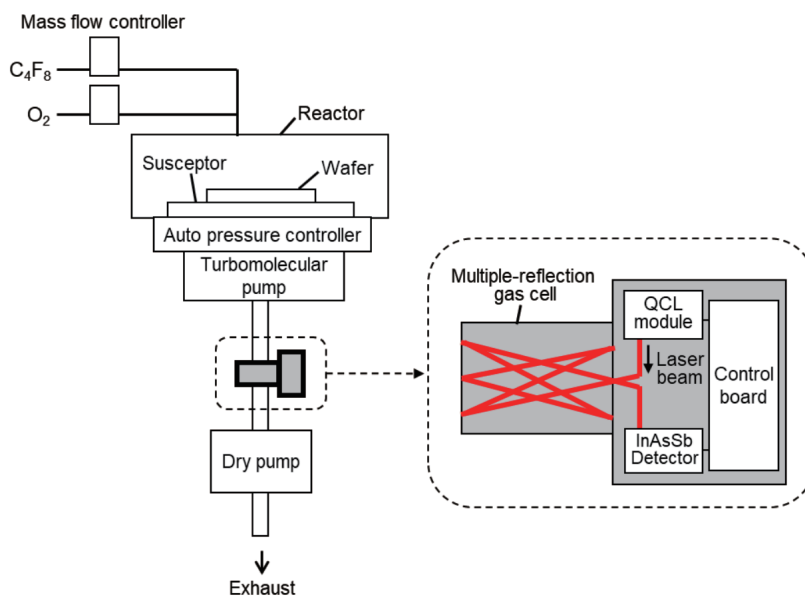

Figure 4　Zero noise and stability.

Figure 5　Schematic diagram of the etching tool with the laser gas analyzer.
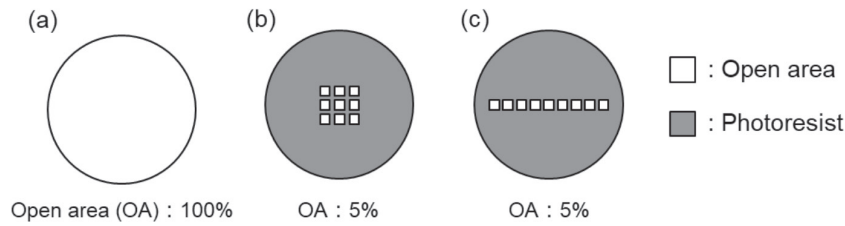
Figure 6　Schematic diagram of SiO₂ samples. Each open area ratio is 100% (a), 5% (b)/(c). There are two types of samples of 5% open area with different open area arguments, square type (b) and rectangular type (c).

グした際のSiF$_4$分圧測定を**Figure 7**に示す。バイアスパワーが増加するにつれて発生するSiF$_4$の分圧が増加する状況が確認された。バイアスパワーが高いほどプラズマイオンの入射エネルギーが高くなりエッチング量も増えることから，妥当な結果と考えられる。プラズマが停止すると同時にSiF$_4$の値も低下しており，測定場所がチャンバーから離れた排気配管であっても遅れはないことが確認された。**Figure 7(b)**に各バイアスパワーにおけるSiO$_2$のエッチレートとSiF$_4$の分圧の関係を示す。両者は0.999以上の高い相関関係にあることが確認され，この結果からSiF$_4$の分圧を測定することでSiO$_2$のエッチレートをリアルタイムに推定できる可能性があることが示唆された。

次に，**Figure 6(b)および(c)**に示すサンプルを基準条件で

あるバイアスパワー30 Wの条件でエッチングした結果を**Figure 8**に示す。エッチングプロセスを開始後，それぞれ222秒と231秒の時点からSiF$_4$の分圧の変化が始まり，242秒および297秒でその変化が収束している。これはSiのほうがSiO$_2$よりもエッチレートが高いことによって生じており，分圧の変化が収束した点は，完全にSiに切り替わりエッチングのエンドポイントであることを示している。

また，マスクパターンの違いによってSiF$_4$の挙動に差が見られている。この差は，チャンバーのコンディションによるばらつきも含まれるが，主要因としてはマスクパターンの形状の差によって発生していると考えられる。

これらの結果より，SiF$_4$の分圧変化を測定することでエッチングエンドポイントを検出できるだけでなく，マスクパターンの違いによるSiF$_4$分圧の挙動の差異を観測できることが分かった。
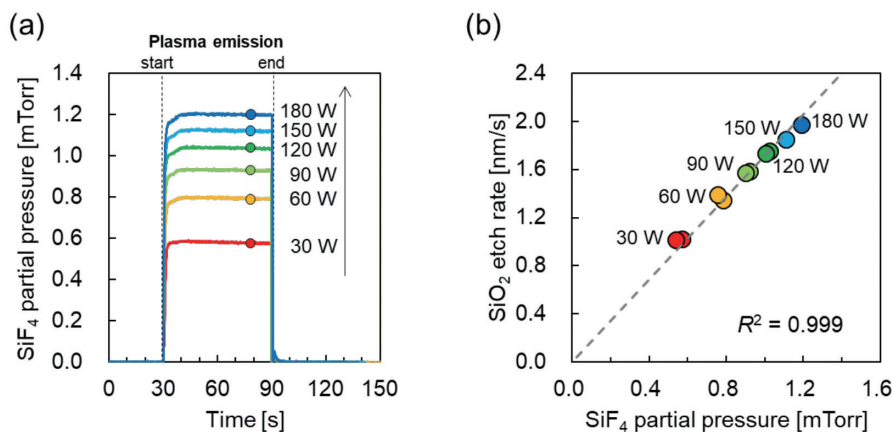
Figure 7　Measurement of SiO₂ etching with bias power in the range of 30–180 W for 1 min using the sample of 100% open area: trend of SiF₄ partial pressure (a). Correlation between SiF₄ partial pressure and SiO₂ etch rate (b).

おわりに

今回開発したIRLAM技術による半導体ガス分析計（LG-100）は，エッチングプロセスの排ガス中の副生物の分圧の変化を高い感度で検知可能であり，その情報からプロセスの状態を把握できることが分かった。近年，AI技術や機械学習が発展し，半導体製造装置においても，それらの技術を活用し装置を自律制御する方向に研究開発が進められている。複雑なプロセスを制御するために多くのパラメータが収集され，多変量解析等によってデータの意味を推測する手法が使われているが，本質的にプロセス状態と直結する質の高いデータが得られるほど，より精密な制御が可能になると考えられる。本分析計を用いて得られる測定データが，プロセスのリアルタイムでの監視や制御に活用できる新たな情報を与え，デバイスの製造工程の効率化，歩留まり改善に貢献していくことを期待している。

＊編集局注：本内容は特段の記載がない限り，本誌発行年時点での自社調査に基づいて記載しています。
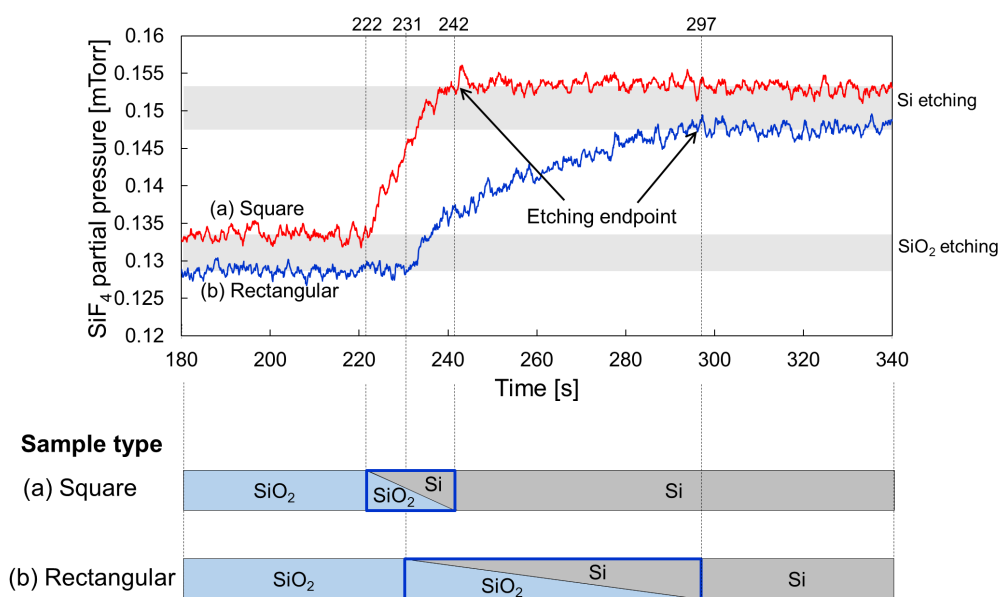
Figure 8　Trend of SiF_4 partial pressure and schematic diagram of etched layer transition during etching with the samples of 5% open area: square type (a) and rectangular type (b).

参考文献

[1] Xiaoyue Wang et al.: Three-dimensional transistors and integration based on low-dimensional materials for the post-Moore's law era, Materials Today, Vol 63, 170 (2023)

[2] 辰巳哲也: 半導体デバイス加工におけるプラズマ制御技術, 応用物理, 第85巻, 第9号, 761(2016)

[3] 飯田裕: 半導体製造プロセスでのプラズマ発光分析終点検知モニタEV140Cの実用例, Readout, Vol.35, 62(2009)

[4] 石田耕三: 赤外線ガス分析計の開発, Readout, Vol.32, 65(2006)

[5] 渋谷享司: 量子カスケードレーザと独自の濃度演算手法を用いたガス分析技術「IRLAM」の開発, Readout, Vol.57, 55(2023)

[6] 岸田創太郎: 高温対応静電容量型隔膜真空計VG-500シリーズの開発, e-Readout-004-2 (2021)
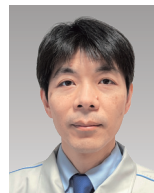
坂口 有平
SAKAGUCHI Yuhei

株式会社堀場エステック
開発本部　開発3部　副部長(ガス分析担当)
Manager
Development Dept.3,
Research & Development Division,
HORIBA STEC,CO., Ltd.

波田 美耶子
HADA Miyako

株式会社堀場エステック
開発本部　開発3部　ガス分析1チーム　サブリーダー
Assistant section leader,
Gas Analysis team1, Development Dept.3,
Research & Development Division,
HORIBA STEC,CO., Ltd.

公益社団法人日本分析化学会による表彰
Awarded by the Japan Society for Analytical Chemistry

第72年会（2023年）公益社団法人日本分析化学会による表彰

表彰の概要

公益社団法人日本分析化学会による表彰制度において，株式会社堀場テクノサービス 分析技術本部 駒谷 慎太郎が「技術功績賞」を株式会社堀場アドバンスドテクノ 基盤技術研究開発部 西尾 友志, 室賀 樹興, 髙味 拓永, 三重大学 橋本 忠範先生, 石原 篤先生のグループが「先端分析技術賞（JAIMA機器開発賞）」を受賞した。

技術功績賞とは：分析技術の向上，あるいは，分析技術による社会的貢献に関し，業績の著しい者のなかから，特に優秀な人物に贈呈される。今年度は2名が受賞。

先端分析技術賞 JAIMA機器開発賞：先端的分析技術開発（機器開発，分析・評価技術開発，分析用新規物質の開発，など）や実用化において，優秀なる業績と展開性を示した個人あるいはグループに贈呈される。今年度は1グループが受賞。

2023年度受賞者

◆技術功績賞
株式会社堀場テクノサービス・分析技術本部長
駒谷 慎太郎

＜研究業績＞
X線分析顕微鏡の開発とその応用

◆先端分析技術賞 JAIMA機器開発賞
株式会社堀場アドバンスドテクノ
基盤技術研究開発部
西尾 友志, 室賀 樹興, 髙味 拓永

＜研究業績＞
工業用無補充式セルフクリーニングpH電極の
製品開発およびその防汚技術

Figure 1 左から橋本 忠範先生, 髙味 拓永, 西尾 友志, 駒谷 慎太郎

Figure 2 室賀 樹興

＊編集局注：本内容は特段の記載がない限り，受賞時点での自社調査に基づいて記載しています。

令和5年度近畿地方発明表彰
Kinki Region Invention Awards 2023

日本弁理士会会長賞

赤外レーザ吸収変調法（特許第6886507号）

表彰の概要

本発明表彰は，近畿地方における発明の奨励・育成を図り，科学技術の向上と地域産業の振興に寄与することを目的としており，近畿地方において優秀な発明，考案，又は意匠（以下「発明等」という）を完成された方々，発明等の実施化に尽力された方々，発明等の指導，奨励，育成に貢献された方々の功績を称え顕彰するものである。この度，HORIBAの特許第6886507号（赤外レーザ吸収変調法）が日本弁理士会会長賞を受賞した。

表彰案件の概要

本発明は，赤外レーザ吸収変調法（IRLAM™: Infrared Laser Absorption Modulation, アーラム）の基本原理に関する発明考案である。本発明は，MEXA-ONE-XL-NX（MEXA-ONE-IRLAM），OBS-ONE-XL（OBS-ONE-IRLAM），PLGA-1000，及びPLGA-7000等に採用されている（例えば，**Figure 1〜3**参照）。

従来発明等の課題

近年，大気汚染などの環境問題，燃焼効率改善，次世代燃料の開発，半導体製造プロセスの改善など，様々な技術課題を解決するため，自動車，船舶，発電所，化学プラント，又は半導体製造プロセス等における排ガス又はプロセスガス（以下サンプルガス）に含まれる測定対象成分の濃度を高速かつ精度良く測定することが求められている。しかし，従来の光吸収を利用したガス分析手法では，サンプルガスの光吸収信号から，測定対象成分の濃度を求める際に，干渉成分[*1]の影響を除去するために，複雑なスペクトル演算処理が必要であり，リアルタイム測定を行うためには，高度な演算処理装置が必要であった。

*1 干渉成分とは，サンプルに複数の成分が含まれている場合，光吸収波長帯が測定対象成分と重なって，測定対象成分の濃度の測定結果に誤差を与える測定対象成分以外の成分である。例えば，COやCO_2の吸収波長帯には水分の吸収波長帯も存在するため，水分は，COやCO_2を測定する際の干渉成分となる。

Figure 1 受賞した技術を用いた製品「MEXA-ONE-IRLAM」

Figure 2 受賞した技術を用いた製品「OBS-ONE-IRLAM」

Figure 3 受賞した技術を用いた製品「PLGA-1000」

本発明等の特徴

本発明は，IRLAMの基本原理に関する発明であり，複雑なスペクトル演算処理をすることなく，簡単な演算で，サンプルガス中の干渉影響を除去するガス分析手法及びそれを適用した分析装置に関する発明である。**Figure 4**を参照して，本発明は，サンプルガスの吸収信号と特徴信号とを用いた演算により，吸収信号の特徴を少ない変数（特徴量）で捉えることができる。これにより，複雑なスペクトル演算処理をすることなく，測定対象成分の濃度を連立方程式を用いた簡単な演算で測定できる。例えば一般的なスペクトルフィッティングで用いるデータ点数は数百点必要だが，本発明ではせいぜい数個から十数個程度の特徴量（相関値）を使えば同等の精度で濃度の算出が可能となる。その結果，演算処理の負荷を小さくすることができ，高度な演算処理装置が不要となり，分析装置のコストを削減すると共に，装置の小型化が可能となる。
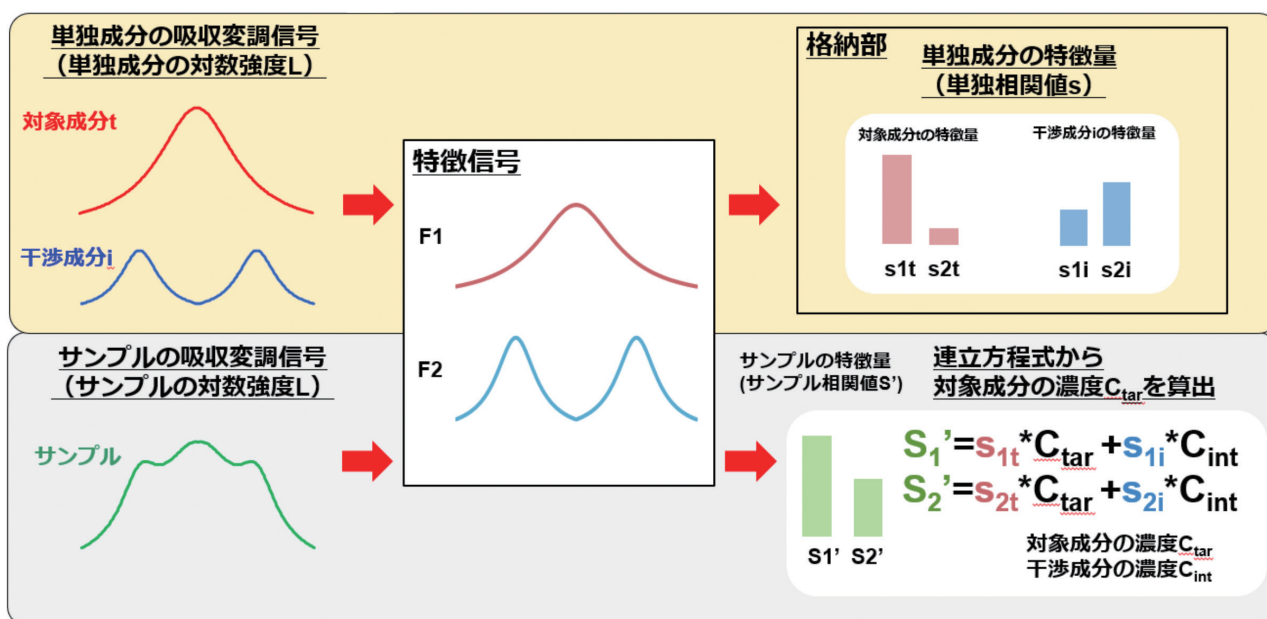
Figure 4　IRLAMの信号処理の概念を説明する図

【登録番号】
特許第6886507号
【発明者】
渋谷 享司

Figure 5　日本弁理士会会長賞　渋谷 享司(右)

Figure 6　実績功労賞　コーポレートオフィサー CTO 中村 博司（右）
　　　　　（代表取締役社長 足立正之代理）

その他受賞案件

受賞名	特許番号	発明の名称	発明者氏名
発明奨励賞	特許第5144829号	イオン電極	小林 一星
発明奨励賞	特許第6857174号	放射線検出装置及び放射線検出用信号処理装置	大橋 聡史
発明奨励賞	特許第6910181号	弁要素, 流体制御弁及び半導体製造装置	赤土 和也, 林 繁之

Figure 7　令和5年度近畿地方発明表彰式 (左から, 渋谷 享司, 中村 博司, 小林 一星)

＊編集局注：本内容は特段の記載がない限り，受賞時点での自社調査に基づいて記載しています。

Topics

トピックス

第13回 HORIBA Group IP World Cup
Gold Award受賞IPの紹介

Award Winners of 2023 HORIBA Group IP World Cup

IP World Cup

Figure 1　HORIBA Group IP World Cup.

ＨＯＲＩＢＡグループで生まれた数々の独創的な技術や知的財産(以下, Intellectual Propertyの略語として「IP」ともいう)が事業の推進力となってきた。技術開発とその成果たる知的財産がHORIBAブランドの本質的な要素であり, HORIBA Group IP World Cup(**Figure 1**)は,HORIBA Group is One Companyの精神のもと,事業を牽引する技術・知的財産をグループ全体で賞賛し, 次なる成長の起爆剤となる技術・知的財産の創出をさらに奨励していくことを趣旨として創設された。

第13回HORIBA Group IP World Cup[*1]では, 海外を含むHORIBAグループの開発拠点で選考された13件の応募があり, 株式会社堀場製作所およびHORIBA MIRA Limitedの「HORIBA Intelligent Lab – Digitalisation of Propulsion System Development for Emissions Compliance」に関する論文がGold Awardを受賞した。

この知的財産は,シミュレーションモデルと実車両による試験とを組み合わせたデジタルツイン技術[*2]を用いることで,車両の路上走行試験を効率的に実現するものである。複雑化する車両開発において, 実機を用いた試験にかかる時間を減らすことで, 作業効率を高め開発工数削減に貢献するものであり,今後のHORIBAグループのエネルギー環境分野の事業をけん引する技術として以下に紹介する。

[*1] 第13回では, 2022年6月1日から2023年5月31日の間に創作, 出願, 論文発表, 特許登録, または外部表彰を受賞したなどの知的財産を対象としている。

[*2] 物理的な対象やプロセスを正確に反映するように設計された仮想モデル。このモデルに基づいて, 分析, 予測, 最適化を行う技術。

HORIBA Intelligent Lab – Digitalisation of Propulsion System Development for Emissions Compliance

IP：（論文）HORIBA Intelligent Lab – Digitalisation of Propulsion System Development for Emissions Compliance (THEISEL 2022 Conference on Thermo and Fluid Dynamics of Clean Propulsion Powerplants 13-16 Sept 2022)

受賞者：Dr. Philip Roberts, Dr. Luke Bates, Aaron Headley, Steven Whelan (HORIBA MIRA／イギリス), 田畑邦夫(株式会社堀場製作所／日本)

Figure 2　左からSteven Whelan, 堀場 厚, Dr. Luke Bates, 田畑 邦夫

Gold Award受賞IPの概要

HORIBA MIRA Limited and HORIBA, Ltd. have won the IP World Cup Gold Award

The 'HORIBA Intelligent Lab' automotive sector team are developing solutions that HORIBA can use to bring benefits to customer's product development processes. HORIBA Intelligent Lab (**Figure 3**) enable the customer to develop smarter. This Solution will enhance the competitiveness of HORIBA equipment and services. One of these solutions is called Empirical Digital Twin. The IP behind this solution has won the gold prize for outstanding innovation in the use of highly accurate virtual simulation within increasingly complex vehicle development projects.

The 'Empirical Digital Twin' EDT

For customers, use of EDT means less physical testing and fewer prototypes. This saves time and significantly reduces costs and risk in the vehicle development process and product.

Digital twins are common already within automotive R&D, but the HORIBA EDT innovative solution improves that method of development much further.

The Empirical Digital Twin is a precise simulation built by AI, created from highly accurate measurement of a physical object under test. **Figure 4** shows the key stages of the EDT solution. It runs fast and can be used in co-simulation with vehicle models to predict efficiency & emissions from thousands of complex scenarios in several hours, instead of physical vehicle tests that would take months of work. Digital twins can be made of engines, batteries, thermal systems, electric machines and more. If it can be measured, it can be modelled. **Figure 5** shows how the EDT is created for any system.

Figure 3   HORIBA Intelligent Lab Overview.

Empirical Digital Twin: Key Stages

Test Designer — Transient excitation signal design specific to the unit under test

Modeller — Rapid generation of transient empirical models using recurrent neural networks

Predictor — Prediction of attributes using transient empirical models at faster than real-time

Optimiser — Multi-objective optimiser and 'hot-spot' identification toolset for improved performance

Figure 4   Outline of planned Empirical Digital Twin Solution key stages.

Figure 5   Empirical Digital Twin creation process flowchart.

The use of digital twins moves the development process into the "digital" world, where optimisation can be carried out much faster and over more scenarios.

Figure 6 shows a comparison of the time taken to validate a powertrain calibration in a vehicle on the road, compared to using EDT in the lab. The EDT solutions shows more than a 70% reduction in time required. This will also result in a >70% reduction in testing cost because expensive vehicle prototypes and transportation to cold and hot climates will not be required.

Once the powertrain digital twin is created and verified it can be shared and used across multiple vehicle platforms and variants, power applications, and also used in other technical areas such as vehicle dynamics and autonomous vehicle system. This enhances efficiency through the entire new product introduction process."

Confidence in results

With new real-world emissions regulation, complex electrified vehicles and new autonomous vehicle function, automotive development requires new ways of working to cope with the huge increases in development effort required in these new areas.

Vehicle development and sign-off requires confidence in the results whether they're virtual or real. HORIBA Intelligent Lab enables our customers to trust that their simulation data is as accurate as the real thing, and check the validity by running scenarios 'in-the-loop' back on the test rig with real hardware.

HORIBA Intelligent Lab solutions build on the legacy and foundation of HORIBA's automotive products with accuracy, reliability and repeatability.
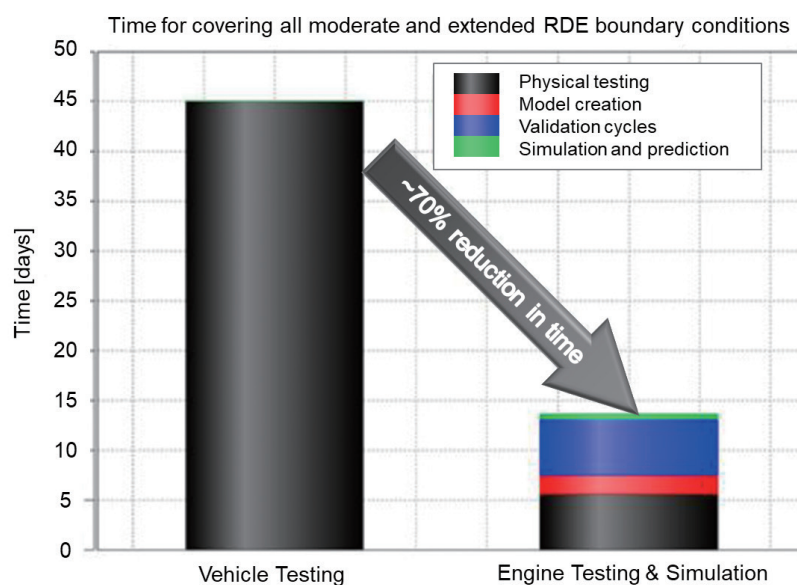

Figure 6   Showing potential time reduction of over 70% for RDE engine calibration validation from EDT process compared to physical on-road vehicle testing.

その他受賞IP

【Silver Award】

Vacuum Gauge

IP：（特許）特許第7418248号 (発明の名称：真空計)

受賞者：岸田創太郎 (株式堀場エステック／日本)

概　要：隔膜真空計の回路基板を冷却するための技術。センサ部を高温に温調する真空計では回路基板を耐熱温度以下に保つ必要があり，従来はファンで外気を取り込み冷却していた。本IPでは，センサや回路基板などを収容するケーシングを2重にし，ケーシングの隙間を調整することで，センサ部と回路基板との温度差により隙間に上昇気流を生じさせ，外気を引き込み回路基板に向かって流す。これにより，ファンがなくても回路基板を冷却することが可能となり，コスト低減・設計の自由度向上にも寄与している。

【Bronze Award】

Disruptive sustainable solid reagent for hematology analyzers

IP：（特許出願）FR2311799 (発明の名称：Composition for hematology analysis)

受賞者：Dr. Dario Donnarumma, Dr. Jocelyne Adjemian (HORIBA ABX SAS／フランス)

概　要：血球計数装置に用いられる希釈液に関する技術である。血球計数装置では測定に大量の希釈液を用いており，希釈液容器の頻繁な交換によって時間がかかると共に，重い容器の持ち運びによって作業者に負担がかかっていた。一方，このような負担を軽減するために希釈液を固形化することは簡単ではなかった。本IPでは，塩や界面活性剤と等の原材料を選定すると共に，塩を粉砕，個々の塩に界面活性剤をコーティングすることで異なる粒径の塩を均一化している。これにより，塩の凝集を抑えつつ溶解性を向上させることができる。結果として，従来よりも飛躍的な効果を持つ固形の希釈試薬の実現に成功した。本IPが適用された固形の希釈試薬は「DilTabs」と呼ばれる。そして，DilTabsは以下のような素晴らしい効果をもたらすことが期待される。
・当社従来比で95%のプラスチック使用量削減，水の消費量削減，輸送による二酸化炭素排出削減等，環境負荷低減につながること
・輸送コストや労働負荷に対し経済的効率を改善できること

【Honorable Mention】

Trolley for EHT/SOEC stacks

IP：（特許）EP22204322.6（発明の名称：A transport and testing trolley for moving and conditioning and/or testing stacked assemblies of electrolyser and/or fuel cell components, An associated station)

受賞者：Jérôme Tardieu（HORIBA FRANCE SAS／フランス），Mathias Rachau, Stefan Hübner （HORIBA FuelCon GmbH／ドイツ)

概　要：本IPは，燃料電池や水素生成のセルスタックの組立/調整・評価工程の改善に関する。従来，セルスタックの組立工程を行った後，それらセルスタック一つ一つを調整・評価していたため，多くの工数を要していた。本IPでは，移動筐体マニホールドを有する「トロリー」上でセルスタックの組立工程が行えるようにしつつ，流体や電気系統がテストステーションとトロリー間で自動的に接続され，炉によって高温のテスト環境を作ることがポイントである。本IPにより，組立ラインからテストステーションへの移動について，①個別の積層セル操作の排除　②準備のためのダウンタイム低減　③製造物の故障リスク低下　④操作者の作業環境の改善　⑤種々の製造エリアのモジュール化 を実現できる。これらの特徴によって従来よりも高度な自動化を可能にし，製造プロセスにおける生産性を向上させることができる。

Figure 7　表彰式

＊編集局注：本内容は特段の記載がない限り，受賞時点での自社調査に基づいて
　記載しています。

Scientific Research Papers from HORIBA Group

From April 1, 2023 to February 29, 2024 on ScienceDirect

Size distributions of cellulose nanocrystals in dispersions using the centrifugal sedimentation method

a: Yusui Sato, Hiroshi Tateno, ab: Yuichi Kato, Takushi Sugino, c: Yoko Iizumi, ac: Takahiro Morimoto, Kazufumi Kobashi

a: HORIBA Institute for Particle Analysis in AIST TSUKUBA (HIPAA)
b: Nanomaterials Research Institute, AIST
c: Nano Carbon Device Research Center, AIST

Free exciton and bound excitons on Pb and I vacancies and O and I substituting defects in PbI_2: Photoluminescence and DFT calculations

a: Sergii Golovynskyi, Iuliia Golovynska, Baikui Li, Honglei Wu, b: Oleksandr I. Datsenko, c: Muhammad Usman, de: Ana I. Pérez-Jiménez, f: Marc Chaigneau, g: Matteo Bosi, Luca Seravalli, h: Tarek Hidouri

a: College of Physics and Optoelectronic Engineering, Shenzhen University
b: Physics Faculty, Taras Shevchenko National University of Kyiv
c: Xuzhou Medical University
d: Technology Innovation Institute, Masdar City, Abu Dhabi
e: Horiba Scientific, Shanghai
f: Horiba Scientific, Palaiseau
g: Institute of Materials for Electronics and Magnetism
h: Physical and Computer Sciences, University of Parma

On the preparation and characterization of AlSi12-graphene powder for powder bed fusion additive manufacturing applications

a: Ali Ghasemi, Eskandar Fereiduni, Mohamed Elbestawi, Saeid Habibi, b: Jasmin Kathrin Saewe, Niklas Hartke, c: Fran Adar, d: Kayvon Savadkouei, e: Yoshinori Fukushima

a: Department of Mechanical Engineering, McMaster University
b: Fraunhofer Institute for Laser Technology ILT
c: HORIBA Scientific, Piscataway
d: HORIBA Scientific, Irvine
e: HORIBA Ltd.

Constructing the oxygen diffusion paths for promoting the stability of acidic water oxidation catalysts

a: Rui Huang, Yunzhou Wen, Wenjuan Shi, Wenzhe Niu, Kai Sun, Bo Zhang, b: Peng Miao, c: Youyong Li, Yujin Ji

a: Department of Macromolecular Science, Fudan University
b: HORIBA (China) Trading Co., Ltd.
c: Soochow University

Tensile strain creates trion: Excitonic photoluminescence distribution over bilayer MoS$_2$ grown by CVD

a: Oleksandr I. Datsenko, Victoriya Shevchenko, b: Sergii Golovynskyi, Iuliia Golovynska,
c: Ana I. Pérez-Jiménez, d: Marc Chaigneau, e: Andrii Golovynskyi, f: Matteo Bosi, Luca Seravalli

a: Taras Shevchenko National University of Kyiv
b: College of Physics and Optoelectronic Engineering, Shenzhen University
c: Technology Innovation Institute, Abu Dhabi
d: Horiba Scientific, Palaiseau
e: V.M. Glushkov Institute of Cybernetics, National Academy of Sciences
f: Institute of Materials for Electronics and Magnetism

Beyond vanilla: Improved autoencoder-based ensemble in-vehicle intrusion detection system

a: Sampath Rajapaksha, Harsha Kalutarage, Andrei Petrovski, b: M. Omar Al-Kadri, c: Garikayi Madzudzo

a: Robert Gordon University
b: University of Doha for Science and Technology
c: Horiba Mira Ltd

In Situ X-ray imaging of HT-PEMFC hot-pressing using contrast enhancement

ab: Adam Zucconi, a: Jennifer Hack, Theo A.M. Suter, Paul R. Shearing, Dan J.L. Brett, Alexander J.E. Rettie,
b: Michele Braglia

a: Department of Chemical Engineering, UCL, London
b: HORIBA MIRA

Micro-mechanisms of deformation and strengthening during high pressure torsion of CoCuFeMnNi high entropy alloy

ab: Reshma Sonkusare, a: N.P. Gurao, Krishanu Biswas, Somnath Bhowmick, c: Joysurya Basu, d: S. Sen,
de: K.G. Pradeep, fg: Manimunda Praveena, f: Sanjit Bhowmick, h: A. Kilmametov, hi: M. Palit

a: Department of Materials Science and Engineering, Indian Institute of Technology
b: Institute of Material and Process Design, Helmholtz-Zentrum Hereon
c: Department of Metallurgical Engineering, Indian Institute of Technology (BHU)
d: Materials Chemistry, RWTH Aachen University
e: Department of Metallurgical and Materials Engineering, Indian Institute of Technology
f: Bruker Nano Surfaces, United States
g: Horiba Scientific, Piscataway
h: Institute of Nanotechnology (INT), Karlsruhe Institute of Technology (KIT)
i: Advanced Magnetics Group, Defence Metallurgical Research Lab

Improvements proposed to noisy-OR derivatives for multi-causal analysis: A case study of simultaneous electromagnetic disturbances

a: Alastair R. Ruddle, b: Alistair P. Duffy, ab: Lokesh Devaraj, c: Qazi Mashaal Khan,
de: Richard Perdriau, Mohsen Koohestani

a: HORIBA MIRA Limited

b: De Montfort University

c: Chalmers University of Technology, Microwave Electronics Laboratory, Department of Microtechnology and Nanoscience

d: ESEO School of Engineering, Department of Electrical and Electronic Engineering

e: Institute of Electronics and Telecommunications of Rennes, University of Rennes

Pervasive aqueous alteration in the early Solar System revealed by potassium isotopic variations in Ryugu samples and carbonaceous chondrites

a: Yan Hu, Frédéric Moynier, Wei Dai, Marine Paquet, Marc Chaussidon, b: Tetsuya Yokoyama, Ikshu Gautam, Makiko K. Haba, Akira Ishikawa, Yuki Masuda, c: Yoshinari Abe, d: Jérôme Aléon, e: Conel M. O'D. Alexander, Richard W. Carlson, fg: Sachiko Amari, h: Yuri Amelin, i: Ken-ichi Bajo, Noriyuki Kawasaki, Sohei Wada, Hisayoshi Yurimoto, aj: Martin Bizzarro, k: Audrey Bouvier, l: Byeon-Gak Choi, m: Nicolas Dauphas, Andrew M. Davis, n: Tommaso Di Rocco, Andreas Pack, o: Wataru Fujiya, p: Ryota Fukai, Tomohiro Usui, Kanako Sakamoto, Masanao Abe, Akiko Miyazaki, Aiko Nakato, Masahiro Nishimura, Tatsuaki Okada, Toru Yada, Kasumi Yogata, Satoru Nakazawa, Takanao Saiki, Satoshi Tanaka, Yuichi Tsuda, Makoto Yoshikawa, pq: Yuki Hibiya, r: Hiroshi Hidaka, Sei-ichiro Watanabe, s: Hisashi Homma, t: Peter Hoppe, u: Gary R. Huss, Alexander N. Krot, Kazuhide Nagashima, v: Kiyohiro Ichida, Shintaro Komatani, Mayu Morita, Morihiko Onose, w: Tsuyoshi Iizuka, x: Trevor R. Ireland, y: Shoichi Itoh, Takaaki Noguchi, z: Noriko T. Kita, Koki Kitajima, aa: Thorsten Kleine, ab: Ming-Chang Liu, Lauren Tafla, Haolan Tang, Edward D. Young, ac: Kazuko Motomura, ad: Izumi Nakai, ae: David Nesvorný, af: Ann Nguyen, ag: Larry Nittler, Meenakshi Wadhwa, ah: Changkun Park, ai: Laurette Piani, aj: Liping Qin, ak: Sara S. Russell, ak: Naoya Sakamoto, am: Maria Schönbächler, an: Kentaro Terada, ao: Yasuko Terada, ap: Richard J. Walker, aq: Katsuyuki Yamashita, ar: Qing-Zhu Yin, as: Shigekazu Yoneda, at: Hiroharu Yui, au: Ai-Cheng Zhang, av: Tomoki Nakamura, aw: Hiroshi Naraoka, Ryuji Okazaki, ax: Hikaru Yabuta, ay: Fuyuto Terui, az: Shogo Tachibana

a: Université Paris Cité, Institut de Physique du Globe de Paris

b: Department of Earth and Planetary Sciences, Tokyo Institute of Technology

c: Graduate School of Engineering, Tokyo Denki University

d: Institut de Minéralogie, de Physique des Matériaux et de Cosmochimie, Sorbonne Université

e: Earth and Planets Laboratory, Carnegie Institution for Science

f: McDonnell Center for the Space Sciences and Physics Department, Washington University

g: Geochemical Research Center, The University of Tokyo

h: Korea Basic Science Institute

i: Department of Natural History Sciences, Hokkaido University

j: Centre for Star and Planet Formation, GLOBE Institute, University of Copenhagen

k: Bayerisches Geoinstitut, Universität Bayreuth

l: Department of Earth Science Education, Seoul National University

m: Department of the Geophysical Sciences and Enrico Fermi Institute, The University of Chicago

n: Faculty of Geosciences and Geography, University of Göttingen

o: Faculty of Science, Ibaraki University

p: ISAS/JSEC, JAXA

q: Research Center for Advanced Science and Technology, The University of Tokyo

r: Department of Earth and Planetary Sciences, Nagoya University

s: Osaka Application Laboratory, SBUWDX, Rigaku Corporation

t: Max Planck Institute for Chemistry

u: Hawai'i Institute of Geophysics and Planetology, University of Hawai'i at Mānoa

v: Horiba Techno Service Co., Ltd.

w: Department of Earth and Planetary Science, The University of Tokyo

x: School of Earth and Environmental Sciences, The University of Queensland

y: Division of Earth and Planetary Sciences, Kyoto University

z: Department of Geoscience, University of Wisconsin-Madison

aa: Max Planck Institute for Solar System Research

ab: Department of Earth, Planetary, and Space Sciences, UCLA

ac: Thermal Analysis, Rigaku Corporation

ad: Department of Applied Chemistry, Tokyo University of Science

ae: Department of Space Studies, Southwest Research Institute

af: Astromaterials Research and Exploration Science, NASA Johnson Space Center

ag: School of Earth and Space Exploration, Arizona State University

ah: Earth-System Sciences, Korea Polar Research Institute

ai: Centre de Recherches Pétrographiques et Géochimiques, CNRS - Université de Lorraine

aj: CAS Key Laboratory of Crust-Mantle Materials and Environments, University of Science and Technology of China

ak: Department of Earth Sciences, Natural History Museum

al: Isotope Imaging Laboratory, Creative Research Institution, Hokkaido University

am: Institute for Geochemistry and Petrology, Department of Earth Sciences, ETH Zurich

an: Department of Earth and Space Science, Osaka University

ao: Spectroscopy and Imaging, Japan Synchrotron Radiation Research Institute

ap: Department of Geology, University of Maryland

aq: Graduate School of Natural Science and Technology, Okayama University

ar: Department of Earth and Planetary Sciences, University of California

as: Department of Science and Engineering, National Museum of Nature and Science

at: Department of Chemistry, Tokyo University of Science

au: School of Earth Sciences and Engineering, Nanjing University

av: Department of Earth Science, Tohoku University

aw: Department of Earth and Planetary Sciences, Kyushu University

ax: Earth and Planetary Systems Science Program, Hiroshima University

ay: Kanagawa Institute of Technology

az: UTokyo Organization for Planetary and Space Science, The University of Tokyo

HORIBA World-Wide Network

JAPAN

HORIBA, Ltd.
2 Miyanohigashi-cho, Kisshoin, Minami-ku, Kyoto, 601-8510, Japan
Phone : +(81)75-313-8121 Fax : +(81)75-321-8312
Biwako Factory
1-15-1, Noka, Otsu, Shiga, 520-0102, Japan
Phone : +(81)-77-548-6130 Fax : +(81)-77-548-6193
Tokyo Branch
Kanda Awaji-cho Nichome Building, 2-6 Kanda Awaji-cho, Chiyoda-ku, Tokyo, 101-0063, Japan
Phone : +81-3-6206-4711 Fax : +81-3-6206-4720
Tokyo Sales Office
Kanda Awaji-cho Nichome Building, 2-6 Kanda Awaji-cho, Chiyoda-ku, Tokyo, 101-0063, Japan
Phone : +81-3-6206-4721 Fax : +81-3-6206-4730
Hokkaido Sales Office
6F Park East Sapporo, 1-3 Minami Ichijo Higashi, Chuo-ku, Sapporo, Hokkaido, 060-0051, Japan
Phone : +81-11-207-1800 Fax : +81-11-207-1802
Tohoku Sales Office
4-21-8 Izumichuo, Izumi-ku, Sendai, Miyagi, 981-3133, Japan
Phone : +81-22-776-8251 Fax : +81-22-772-6727
Tochigi Sales Office
1F Flora Building, 1-9-15 Higashishukugo, Utsunomiya, Tochigi, 321-0953, Japan
Phone : +81-28-634-7051 Fax : +81-28-634-6099
Yokohama Sales Office
1F Prime ShinYokohama Building, 2-3-19 Shinyokohama, Kohoku-ku, Yokohama, Kanagawa, 222-0033, Japan
Phone : +81-45-478-7017 Fax : +81-45-478-7029
Nagoya Sales Office
4F BIZrium Nagoya, 3-1-17 Noritakeshinmachi, Nishi-ku, Nagoya, Aichi, 451-0051, Japan
Phone : +81-52-433-3450 Fax : +81-52-433-3460
Toyota Sales Office
2-23 Tsukasa-cho, Toyota, Aichi, 471-0831, Japan
Phone : +81-565-37-8510 Fax : +81-565-37-8511
Hamamatsu Sales Office
221-1 Sanjino-cho, Minami-ku, Hamamatsu, Shizuoka, 430-0816, Japan
Phone : +81-53-468-7780 Fax : +81-53-468-7781
Osaka Sales Office
4F ShinOsaka UenoToyo Building, 7-4-17 Nishinakajima, Yodogawa-ku, Osaka, 532-0011, Japan
Phone : +81-6-6390-8011 Fax : +81-6-6390-8012
Shikoku Sales Office
9-9 Imazato-cho, Takamatsu, Kagawa, 760-0078, Japan
Phone : +81-87-867-4800 Fax : +81-87-867-4801
Hiroshima Sales Office
1F Furuta Building, 2-5-27 Miyanomachi, Fuchu-cho, Aki-gun, Hiroshima, 735-0005, Japan
Phone : +81-82-288-4433 Fax : +81-82-286-0761
Kyusyu Sales Office
1F Hakata Fukoku Seimei Building, 8-30 Tenyamachi, Hakata-ku, Fukuoka, 812-0025, Japan
Phone : +81-92-292-3593 Fax : +81-92-292-3594
HORIBA Advanced Technology Center
11-5 Hokotate-cho, Kamitoba, Minami-ku, Kyoto, 601-8116, Japan
Phone : +81-75-693-2300 Fax : +81-75-693-2350
Kutsuki Training Center
335-10 Tochu, Kutsuki, Takashima, Shiga, 520-1425, Japan
Phone : +81-740-38-3127 Fax : +81-740-38-3126

HORIBA STEC, Co., Ltd.
11-5 Hokotate-cho, Kamitoba, Minami-ku, Kyoto, 601-8116, Japan
Phone : +(81)-75-693-2300 Fax : +(81)-75-693-2350
Aso Factory
Torikokogyodanchi, 358-11, Koumaibata, Toriko, Nishiharamura, Aso-gun, Kumamoto, 861-240, Japan
Phone : +(81)-96-279-2921 Fax : +(81)-96-279-3364
Fukuchiyama Technology Center
11-1 Miwa-cho Miwa, Fukuchiyama, Kyoto, 620-1445 Japan
Phone : +(81)-773-59-2070 Fax : +(81)-773-59-2074
Tokyo Sales Office
5F Kanda Awaji-cho Nichome Building, 2-6 Kanda Awaji-cho, Chiyoda-ku, Tokyo, 101-0063, Japan
Phone : +81-3-6206-4731 Fax : +81-3-6206-4740

Tohoku Sales Office
4-21-8 Izumichuo, Izumi-ku, Sendai, Miyagi, 981-3133, Japan
Phone : +81-22-772-6717 Fax : +81-22-772-6727
Yamanashi Sales Office
3F Daita Building, 2-14-13, Marunouchi, Kofu, Yamanashi, 400-0031, Japan
Phone : +81 55-231-1351 Fax : +81- 55-231-1352
Nagoya Sales Office
4F BIZrium Nagoya, 3-1-17 Noritakeshinmachi, Nishi-ku, Nagoya, Aichi, 451-0051, Japan
Phone : +81-52-433-3451 Fax : +81-52-433-3461
Kyushu Chuo Sales Office
Torikokogyodanchi, 358-11 Koumaibata, Toriko, Nishiharamura, Aso-gun, Kumamoto, 861-2401, Japan
Phone : +81-96-279-2922 Fax : +81-96-279-3364

HORIBA Advanced Techno, Co.,Ltd.
2 Miyanohigashi-cho, Kisshoin, Minami-ku, Kyoto, 601-8551, Japan
Phone : +(81)-75-321-7184 Fax : +(81)-75-321-7291
Factory
2 Miyanohigashi-cho, Kisshoin, Minami-ku, Kyoto, 601-8551, Japan
Phone : +81-75-321-1215 Fax : +81-75-321-1079
Tokyo Sales Office
Kanda Awaji-cho Nichome Building, 2-6 Kanda Awaji-cho, Chiyoda-ku, Tokyo, 101-0063, Japan
Phone : +81-3-6206-4751 Fax : +81-3-6206-4760
Tohoku Sales Office
4-21-8 Izumichuo, Izumi-ku, Sendai, Miyagi, 981-3133, Japan
Phone : +81-22-776-8253 Fax : +81-22-772-6727
Nagoya Sales Office
4F BIZrium Nagoya, 3-1-17 Noritakeshinmachi, Nishi-ku, Nagoya, Aichi, 451-0051, Japan
Phone : +81-52-433-3452 Fax : +81-52-433-3462
Osaka Sales Office
4F ShinOsaka UenoToyo Building, 7-4-17 Nishinakajima, Yodogawa-ku, Osaka, 532-0011, Japan
Phone : +81-6-6390-8211 Fax : +81-6-6390-8222
Shikoku Satellite Office
9-9 Imazato-cho, Takamatsu, Kagawa, 760-0078, Japan
Phone : +81-87-867-4841 Fax : +81-87-867-4842
Kyushu Sales Office
1F Hakata Fukoku Seimei Building, 8-30 Tenyamachi, Hakata-ku, Fukuoka, 812-0025, Japan
Phone : +81-92-292-3595 Fax : +81-92-292-3596
Kyushu Chuo Sales Office
Torikokogyodanchi, 358-11, Koumaibata, Toriko, Nishiharamura, Aso-gun, Kumamoto, 861-240, Japan
Phone : +81-96-234-8035 Fax : +81-75-321-7291

HORIBA TECHNO SERVICE Co., Ltd.
2 Miyanohigashi-cho, Kisshoin, Minami-ku, Kyoto, 601-8305, Japan
Phone : +81-75-313-8125 Fax : +(81)-75-321-5647
Tokyo Service Station
4F Kanda Awaji-cho Nichome Building, 2-6 Awaji-cho, Kanda, Chiyoda-ku,Tokyo, 101-0063, Japan
Phone : +81-570-200-809 Fax : +81-3-6206-4742
Hokkaido Sevice Station
6F Park East Sapporo, 1-3 Minami Ichijo Higashi, Chuo-ku, Sapporo, Hokkaido, 060-0051, Japan
Phone : +81-570-200-809 Fax : +81-11-207-1802
Tohoku Service Station
4-21-8 Izumichuo, Izumi-ku, Sendai, Miyagi, 981-3133, Japan
Phone : +81-570-200-809 Fax : +81-22-772-6727
Fukushima Service Station
101 Office Tatsumi, 5-13-17 Saikon, Koriyama, Fukushima, 963-8862, Japan
Phone : +81-570-200-809 Fax : +81-24-925-9312
Tochigi Service Station
1F Flora Building, 1-9-15 Higashishukugo, Utsunomiya, Tochigi, 321-0953, Japan
Phone : +81-570-200-809 Fax : +81-28-634-6099
Chiba Service Station
1-8-12 Goichuo-higashi, Ichihara, Chiba, 290-0054,Japan
Phone : +81-570-200-809 Fax : +81-436-24-0642
Kashima Service Station
1-4-35 Kamisu, Kamisu, Ibaraki, 314-0143, Japan
Phone : +81-570-200-809 Fax : +81-299-92-9561

Tsukuba Service Station
203 Tsukuba Cityia Moi Building, 5-20-2 Kenkyugakuen, Tsukuba, Ibaraki, 305-0817, Japan
Phone : +81-570-200-809 Fax : +81-29-859-5221
Saitama Service Station
1F Higashikawaguchi Garden Plaza, 1-6-1 Totsukahigashi, Kawaguchi, Saitama, 333-0802, Japan
Phone : +81-570-200-809 Fax : +81-48-298-6880
Nishitokyo Service Station
1F The-Macrocosm, 3-37-34 Izumi, Kokubunji, Tokyo, 185-0024, Japan
Phone : +81-570-200-809 Fax : +81-42-322-3210
Yokohama Service Station
1F Prime ShinYokohama Building, 2-3-19 Shinyokohama, Kohoku-ku, Yokohama, Kanagawa, 222-0033, Japan
Phone : +81-570-200-809 Fax : +81-45-478-7029
Fuji Service Station
1F Suzuki Building, 4-7 Suzukawahigashi-cho, Fuji, Shizuoka, 417-0012, Japan
Phone : +81-570-200-809 Fax : +81-545-33-3159
Hamamatsu Service Station
221-1 Sanjino-cho, Minami-ku, Hamamatsu, Shizuoka, 430-0816, Japan
Phone : +81-570-200-809 Fax : +81-53-464-6528
Tokai Service Station
2-23 Tsukasa-cho, Toyota, Aichi, 471-0831, Japan
Phone : +81-570-200-809 Fax : +81-565-37-3520
Nagoya Service Station
Wakahara Building, 5-207 Kamiyashiro, Meito-ku, Nagoya, Aichi, 465-0025, Japan
Phone : +81-570-200-809 Fax : +81-52-705-0710
Hokuriku Service Station
1F Ichigo Toyama Station West Building, 1-1-19, Jinzuhonmachi, Toyama, 930-0008, Japan
Phone : +81-570-200-809 Fax : +81-76-471-5493
Mie Service Station
1F Taiyo-Seimei Yokkaichi Building, 1-1-18 Unomori, Yokkaichi, Mie, 510-0074, Japan
Phone : +81-570-200-809 Fax : +81-59-340-6063
Kyoto Service Station
2 Miyanohigashi, Kisshoin, Minami-ku, Kyoto, 601-8305, Japan
Phone : +81-570-200-809 Fax : +81-75-321-5647
Osaka Service Station
1-6-40, Hagoromo, Takaishi-shi, Osaka, 592-0002, Japan
Phone : +81-570-200-809 Fax : +81-72-267-6655
Hyogo Service Station
1F Harima Building, 1215-1, Tsuchiyama, Hiraoka-cho, Kakogawa-shi, Hyogo, 675-0104, Japan
Phone : +81-570-200-809 Fax : +81-78-941-0123
Shikoku Service Station
9-9 Imazato-cho, Takamatsu, Kagawa, 760-0078, Japan
Phone : +81-570-200-809 Fax : +81-87-867-4822
Okayama Service Station
1-12-35 Tsurajima, Kurashiki, Okayama, 712-8012, Japan
Phone : +81-570-200-809 Fax : +81-86-446-5637
Hiroshima Service Station
1F Furuta Building, 2-5-27 Miyanomachi, Fuchucho, Aki-gun, Hiroshima, 735-0005, Japan
Phone : +81-570-200-809 Fax : +81-82-286-0761
Yamaguchi Service Station
1F 3rd Hanada Building, 1-72 Hashimoto, Shunan, Yamaguchi, 745-0022, Japan
Phone : +81-570-200-809 Fax : +81-834-34-8685
Kyusyu Service Station
1F Hakata Fukoku Seimei Building, 8-30 Tenyamachi, Hakata-ku, Fukuoka, 812-0025, Japan
Phone : +81-570-200-809 Fax : +81-92-292-3598
Oita Service Station
1F Tsuruwa Building, 2-2-37 Hagiwara, Oita, 870-0921, Japan
Phone : +81-570-200-809 Fax : +81-97-551-3889
Kumamoto Service Station
Toriko-kogyodanchi, 358-11, Koumaibata, Toriko, Nishiharamura, Aso-gun, Kumamoto, 861-2401, Japan
Phone : +81-570-200-809 Fax : +81-96-279-2986

HORIBA World-Wide Network

BRAZIL

HORIBA Instruments Brasil, Ltda.
Rua Presbitero Plinio Alves de Souza, 645,
Loteamento Multivias, Jardim Ermida II - Jundiai
Sao Paulo - CEP 13.212-181 Brazil
Phone : +(55)-11-2923-5400 Fax : +(55)-11-2923-5490

TCA/HORIBA Sistemas de Testes Automotivos Ltda.
Avenida Luigi Papaiz, 239 - Campanário, Diadema,
São Paulo, Brazil CEP: 09931-610
Phone : +(55)-11-4224-0200 Fax : +(55)-11-4227-3133

CANADA

HORIBA Canada, Inc.
Unit102, 5555 North Service Road Burlington,
Ontario, Canada, L7L 5H7
Phone : +(1)-905-335-0234 Fax : +(1)-905-331-2362
London Office
347 Consortium Court, London, Ontario, Canada,
N6E 2S8
Phone : 1-519-668-6920   Fax : 1-519-668-8437

U.S.A.

HORIBA Americas Holding Incorporated
9755 Research Drive, Irvine, CA 92618, U.S.A.
Phone : +(1)-949-250-4811

HORIBA Instruments Incorporated
9755 Research Drive, Irvine, CA 92618, U.S.A.
Phone : +(1)-949-250-4811 Fax : +(1)-949-250-0924
Ann Arbor Office
5900 Hines Drive, Ann Arbor, MI 48108, U.S.A.
Phone : +(1)-734-213-6555 Fax : +(1)-734-213-6525
Austin Office
9701 Dessau Road, Suite 605, Austin, TX 78754,
U.S.A.
Phone : +(1)-512-836-9560 Fax : +(1)-512-836-8054
Canton Office
5449 Research Drive Canton, MI 48188, U.S.A.
Phone : +(1)-800-445-9853 Fax : +(1)-734-483-1592
Fletcher Office
270 Rutledge Road, Unit D Fletcher, NC 28732,
U.S.A.
Phone : +(1)-828-676-2801 Fax : +(1)-828-676-2805
Houston Office
5390 Bay Oaks Drive, Pasadena, TX 77505
Phone : +1-281-482-4334   Fax : +1-281-674-6058
Novato Field Office
359 Bel Marin Keys Blvd, #18, Novato, CA 94949
HORIBA New Jersey Optical Spectroscopy Center
20 Knightsbridge Rd, Piscataway, NJ 08854, U.S.A.
Phone : +(1)-732-494-8660 Fax : +(1)-732-549-5125
Portland Office
7007 S.W. Cardinal Lane, Suite 185, Portland, OR
97224, U.S.A.
Phone : +(1)-503-624-9767 Fax : +(1)-503-968-3236
HORIBA Reno Technology Center
3740 Barron way Reno, Nevada 89511, U.S.A.
Phone : +(1)-775-358-2332 Fax : +(1)-775-358-0434
Sunnyvale Office
430 Indio Way, Sunnyvale CA 94085, U.S.A.
Phone : +(1)-408-730-4772 Fax : +(1)-408-730-8975
Tempe Office
1515 West University Drive, Suite 101 Tempe, AZ
85281, U.S.A.
Phone : +(1)-480-791-2203
Troy Office
2890 John R Road, Troy, MI 48083, U.S.A.
Phone : +(1)-248-689-9000 Fax : +(1)-248-689-8578
Salt Lake City Office
630 Komas Drive, Suite 310, Salt Lake City, UT
84108 , U.S.A

AUSTRIA

HORIBA (Austria) GmbH
Kaplanstrasse 5, A-3430 Tulln, Austria
Phone : +(43)-2272-65225 Fax : +(43)-2272-65225-45

CZECH

HORIBA Czech, Olomouc Factory
Zeleznicni 512/7, 779 00 Olomouc, Czech Republic
Phone : +(420) 588 118 365 + (420) 588 118 393
HORIBA Czech, Prague Office
Prumyslova 1306/7, CZ-10200, Praha 10, Czech
Republic
Phone : +(420) 246 039 265

FRANCE

HORIBA Europe Holding SASU
14 Boulevard Thomas Gobert - CS 45002 - 91120
Palaiseau

HORIBA Europe Research Center
14 Boulevard Thomas Gobert - Passage Jobin
Yvon CS 45002 - 91120 Palaiseau - France
Phone : +(33)-1-69-74-72-00 Fax : +(33)-1-69-31-32-20
HORIBA FRANCE SAS, Lille Office
455 avenue Eugène Avinée - 59120 LOOS -
France
Phone : +(33)-1-69-74-72-00 Fax : +(33)-3-20-59-18-08
HORIBA FRANCE SAS, Vénissieux Office

HORIBA Advanced Techno France SAS
100 B Allée Saint Exupéry 38330 Montbonnot-
Saint-Martin
Phone : +33 (0)4 76 41 86 39 Fax : +33 (0)4 76 41 92 27

HORIBA ABX SAS
Parc Euromédecine, rue du Caducée, BP7290,
34184 Montpellier Cedex 4, France
Phone : +33 (0)4 67 14 15 16 Fax : +33 4-67-14-15-17

GERMANY

HORIBA Europe GmbH / Oberursel Office
Hans-Mess-Str.6, D-61440 Oberursel, Germany
Phone : +(49)-6172-1396-0 Fax : +(49)-6172-1373-85
Darmstadt Office
Landwehrstrasse 55, D-64293, Darmstadt,
Germany
Phone : +(49)-6151-5000-0 Fax : +(49)-6151-5000-3865
Dresden Office
Hugo-Junckers-Ring 1, 01109 Dresden, Germany
Phone : +(49)-351-8896807 Fax : +(49)-351-8896808
Flörsheim Office
Mariechen-Graulich-Straße 10-12a, 65439
Flörsheim, Germany
Phone : +49 6145 37699-12
Hanover Office
Frankenring 14, D-30855 Langenhagen, Germany
Phone : +49 511-65523987 Fax : +49 511-54571751
Korschenbroich Office
Friedrich-Ebert-Str. 9-11, D-41352 Korschenbroich,
Germany
Phone : +(49)-2161-47537-0
Leichlingen Office
Julius-Kronenberg-Str. 9, D-42799 Leichlingen,
Germany
Phone : +(49)-2175-8978-0 Fax : +(49)-2175-897850
Munich Office
Waldmeisterstr. 72-74/Robinienstr. 66, D-80935
Munich, Germany
Phone : +(49)-89-2444779-0 Fax : +(49)-89-2444779-10
Potsdam Office
Dennis-Gabor-Str. 2, D-14469 Potsdam, Germany
Phone : +(49)-3316-4900-70 Fax : +(49)-3316-4900-74
Stuttgart Office (Neuhausen)
Zabergaeustr. 3, D-73765 Neuhausen, Germany
Phone : +(49)-7158-933-800 Fax : +(49)-7158-933-899
Wolfsburg Office
Klauskamp, Heinenkap II 38444 Wolfsburg ,
Germany
Phone : +(49)-5361-38653-16 Fax : +(49)-5361-38653-24

HORIBA Jobin Yvon GmbH
Hans-Mess-Str. 6, 61440 Oberursel, Germany
Phone : 49(0)61-72-13-96500

HORIBA FuelCon GmbH
Otto-von-Guericke-Allee 20, 39179 Barleben,
Germany
Phone : +49 39203 514 400 Fax : +49 39203 514 409

BeXema GmbH
Otto-von-Guericke-Allee 20, 39179 Barleben,
Germany
Phone : +49 39203 964 200

HORIBA Tocadero GmbH
Johann-Hittorf-Str. 8 12489 Berlin Germany
Phone : +49 (0)30 6392 3150 Fax : +49 (0)30 6392 3151

ITALY

HORIBA ITALIA Srl
Via Luca Gaurico 209 - 00143 Roma Italy
Phone : +(39)-6-51-59-22-1 Fax : +(39)-6-51-96-43-34
Torino Office
Via Feroggio, 30, 10151 Torino, Italy
Phone : +(39)-1-19-04-06-01 Fax : +(39)-1-19-00-04-48

HORIBA ABX SAS, Italy Branch
Viale Luca Gaurico 209/211, 00143 Roma, Italy
Phone : +(39)-6-51-59-22-1 Fax : +(39)-6-51-96-43-34

NETHERLANDS

HORIBA Europe GmbH, Netherlands Branch
Science Park Eindhoven 5080 (Industrial park
"Ekkersrijt") 5692 EA, 1 Son, Netherlands
Phone : +(31)-40-2900240 Fax : +(31)-40-2900624

POLAND

HORIBA ABX Sp. z o.o.
Aleja Niepodleglosci 18
02-653 Warszawa (Warsaw), Poland.
Phone : +(48)-22-673-2022 Fax : +(48)-22-673-2026

PORTUGAL

HORIBA ABX SAS, Portugal Branch
Alfrapark - Estrada de Alfragide n° 67, Edificio F -
Piso 0 Sul, 2610-008 Amadora, Portugal
Phone : +(351)-2-14-72-17-70 Fax : +(351)-2-14-72-17-89

ROMANIA

HORIBA (Austria) GmbH, Romania Branch
B-dul.Republicii, nr. 164, Etaj Parter, Birourile nr. 3
si 4, Pitesti, 110177, Judetul Arges, ROMANIA
Phone : +(40)-348-807117 Fax : +(40)-348-807118

RUSSIA

HORIBA OOO
Altufievskoe shosse, 13, building 5, 127106,
Moscow, Russia
Phone : +(7)-495-221-87-71 Fax : +(7)-495-221-87-68
Zelenograd Office
Office 106, 2nd West st., 1, build 1, 124460,
Zelenograd city, Moscow, Russia
Phone : +(7)-499-995-09-54

SPAIN

HORIBA ABX SAS, Spain Branch
Calle Apolonio Morales. Num. 6 (Bajos), 28036
Madrid, Spain
Phone : +(34)-91-353-30-10 Fax : +(34)-91-353-30-11

HORIBA MIRA SPAIN, S.L.
Calle Oficios, nave 22, 04620 Vera (Almería)
Phone : +(34)-950-39-11-53

SWEDEN

HORIBA Europe GmbH, Sweden Branch (Gothenburg)
Grimboasen 10 A, S-417 05 Gothenburg, Sweden
Phone : +(46)-10-161 1500 Fax : +(46)-10-161 1503
HORIBA Europe GmbH, Sweden Branch (Sodertalje)
Sydhamnsvagen 55-57, SE- 15138, Sodertalje,
Sweden
Phone : +(46)-8-550-80701 Fax : +(46)-8-550-80567

TURKEY

HORIBA Europe GmbH, Istanbul Office
Veysel Karani Mahallesi, Colakoglu Sokak No: 10,
Rings Rezidans D:23, PK: 34885, Sancaktepe /
Istanbul
Phone : +90 216 572 1166 Fax : +90 216 572 1167

HORIBA World-Wide Network

UNITED KINGDOM

HORIBA UK Limited
Kyoto Close Moulton Park Northampton NN3 6FL
UK
Phone : +44 (0)1604 542500 Fax : +44 (0)1604 542699

HORIBA UK Finance Limited
Kyoto Close Moulton Park Northampton NN3 6FL
UK
Phone : +(44) 1604 542500

HORIBA Jobin Yvon IBH Ltd.
133 Finnieston St. Glasgow G3 8HB, UK
Phone : +(44)-141-229-67-89 Fax : +(44)-141-229-67-90

HORIBA Test Automation Limited
Brook Court Whittington Hall Worcester WR5 2RX,
UK
Phone : +(44)-1905-359359 Fax : +(44)-1905 359332

HORIBA MIRA Limited
Watling Street, Nuneaton, Warwickshire, CV10
0TU, United Kingdom
Phone : +(44)-24-7635-5000
Quatro Park
Unit 1, Quatro Park, Paycocke Road, Basildon,
Essex, SS14 3GH, United Kingdom
Phone : +(44)-1268-290100

HORIBA MIRA Certification Limited
Watling Street, Nuneaton, Warwickshire, CV10
0TU, United Kingdom
Phone : +(44)-24-7635-5000

MIRA Service Limited
Watling Street, Nuneaton, Warwickshire, CV10
0TU, United Kingdom
Phone : +(44)-24-7635-5000

MIRA Technology Park Limited
Watling Street, Nuneaton, Warwickshire, CV10
0TU, United Kingdom
Phone : +(44)-24-7635-5000

MIRA Technology Park Services Limited
Watling Street, Nuneaton, Warwickshire, England,
CV10 0TU
Phone : +(44)-24-7635-5000

IDV Robotics Ltd.
Suite 1.03, Technology Centre Nw05 Mira
Technology Park, Watling Street, Nuneaton,
Warwickshire, United Kingdom, CV10 0TU

CHINA

HORIBA INSTRUMENTS (SHANGHAI) CO., LTD
No.99, Chunxiu Rd, Anting Town, Jiading District,
Shanghai, China 201804
Phone : +(86)-21-6952-2835 Fax : +(86)-21-6952-2823

HORIBA Technology (Suzhou) Co.,LTD.
No.1 building, Industry park, No.101 Chenmenjing
Rd, Taicang, Jiangsu, China (215400)
Phone : +(86)-0512-3306-6388

HORIBA (China) Co., Ltd.
No.99, Chunxiu Rd, Anting Town, Jiading District,
Shanghai, China 201804
Phone : +(86)-21-6289-6060 Fax : +(86)-21-6289-5553

HORIBA (China) Trading Co., Ltd.
Unit D, 1F, Building A, Synnex International Park,
1068 West Tianshan Road, 200335, Shanghai
Phone : +(86)-21-6289-6060 Fax : +(86)-21-6289-5553
Beijing Branch
12F, Metropolis Tower, No.2, Haidian Dong 3
Street, Beijing, 100080, China
Phone : +(86)-10-8567-9966 Fax : +(86)-10-8567-9066
Guangzhou Branch
Room 1611/1612, Goldlion Digital Network Center,
138 Tiyu Road East, Guangzhou 510620, China
Phone : +(86)-20-3878-1883 Fax : +(86)-20-3878-1810

HORIBA Precision Instruments (Beijing) Co., Ltd.
Building1, No.3 yuan, Xixing Road, Houshayu
Town, Shunyi District, Beijing, 101318 China
Phone : +86-10 8492 9402 Fax : +86-10 8492 7216

MIRA China Ltd.
Unit E, B1F, Building A, Synnex International Park,
No. 1068 Tianshan West Road, Shanghai 200335
Phone : +(86)-21-6220-6377 Fax : +(86)-21-6220-6379
Xiangyang Branch
A27-1, Jiahai industrial park, High-tech District,
Xiangyang, Hubei, 441004, China
Phone : +(86)-710-2578-268

INDIA

HORIBA India Private Limited
246, OKHLA INDUSTRIAL ESTATE, PHASE 3
NEW DELHI - 110020, India
Phone : +91-11-4646-5000 Fax : +91-11-4646-5020
Bangalore Office
3rd, No.504, 22nd Cross HSR Club Road Sector-3,
Bengaluru, Karnataka, 560102, INDIA
Phone : +(91)-80-4127-3637
Chennai Office
No.9, 01 & 02 Floor,Ganapathy Colony,Thiru-Vi-Ka
Industrial Estate,Guindy, Chennai ,600032 India
Phone : +(91)-44-42077899
Haridwar Factory
Plot No. 26, Sector-7, IIE, SIDCUL, Haridwar,
Uttarakhand - 249403, India
Phone : +(91)-1334-239139
Kolkata Office
EK Tower/6th Floor/Office -4A, Action Area-II D,
Newtown, Pin Code 700161,India
Phone : +(91)-90073-63356
Nagpur Factory
Plot No B-3, C-32, MIDC Industrial Area, Butibori,
Phase 2, Nagpur, Maharashtra, 441122, India
Phone : +(91) 71-0328-0200
Technical Center
D-225,Chakan MIDC Phase-II, Bhamboli Village,
Pune-410501.
Phone : +(91) 21-3567-6000

INDONESIA

PT HORIBA Indonesia
Jl. Jalur Sutera Blok 20A, No. 16-17, Kel. Kunciran,
Kec. Pinang Tangerang - 15144, Indonesia
Phone : +62-21-3044 8525 Fax : +62-21-3044 8521

KOREA

HORIBA KOREA Ltd.
25, 94-Gil, Iljik-Ro, Manan-Gu, Anyang-Si,
Gyeonggi-Do, 13901, Korea
Phone : +(82)-31-296-7911 Fax : +(82)-31-296-7913
Ulsan Office
(44633)5F, 10, Bukbusunhwan-doro, Nam-gu,
Ulsan, Korea
Phone : +(82)-52-275-0122 Fax : +(82)-52-276-0136
Dongtan Office
513-Ho, Digital Station, 160, Samsung 1-Ro,
Hwaseong-Si, Gyeonggi-Do, 18450, Korea
Phone : +(82)70-4689-0647

HORIBA STEC KOREA, Ltd.
98, Digital valley-ro Suji-gu, Yongin-si Gyeonggi-do
16878 Korea
Phone : +(82)-31-8025-6500 Fax : +(82)-31-8025-6599

MALAYSIA

HORIBA Malaysia Sdn Bhd
73-3-1, Ideal@The One, Jalan Mahsuri, Bayan
Lepas, 11950 Penang, Malaysia

PHILIPPINES

HORIBA INSTRUMENTS (SINGAPORE) PTE LTD., MANILA OFFICE
27/F Tower 2, The Enterprise Center, 6766 Ayala
Avenue corner Paseo de Roxas, Brgy. San
Lorenzo, Makati City, Philippines, 1226
Phone : +63 2 8885 8468

SINGAPORE

HORIBA Instruments (Singapore) Pte Ltd
3 Changi Business Park Vista #01-01, Singapore
486051
Phone : +(65)-6-745-8300 Fax : +(65)-6-745-8155
West Office
83 Science Park Drive, #02-02A, The Curie,
Singapore 118258
Phone : +(65)-6-908-9660

TAIWAN

HORIBA Taiwan, Inc.
8F.-8, No.38, Taiyuan St. Zhubei City, Hsinchu
County 30265, Taiwan (R.O.C.)
Phone : +(886)-3-5600606 Fax : +(886)-3-5600550
Tainan Office
1F., No.90 Ziyou Rd., Shanhua Dist., Tainan City,
74158, Taiwan (R.O.C.)
Phone : +(886)6-581-1108 Fax : +(886)6-581-1160

THAILAND

HORIBA Holding (Thailand) Limited
46/8 Rungrojthanakul Bld., 1st , 2 nd Floor,
Ratchadapisek Road., Huai Khwang Bangkok
10310
Phone : +(66)-2-861-59-95 Fax : +(66)-2-861-52-00

HORIBA (Thailand) Limited
46/8 Rungrojthanakul Bld., 1st , 2 nd Floor,
Ratchadapisek Road., Huai Khwang Bangkok
10310
Phone : +66 (0) 2 861 5995 ext.123 Fax : +66 (0) 2 861 5200

VIETNAM

HORIBA Vietnam Company Limited
Lot 3 and 4, 16 Floor, Detech Tower II, No. 107
Nguyen Phong Sac Street, Dich Vong Hau Ward,
Cau Giay District, Hanoi, Vietnam
Phone : +(84)-24-3795-8552 Fax : +(84)-24-3795-8553
Branch in Ho Chi Minh city
7th Floor, No 09 Dinh Tien Hoang Street, Da Kao
Ward, District 1, Hochiminh City
Phone : +84 2871095386

HORIBA

Explore the future